

Accepted for publication in the *Astrophysical Journal Supplements*

The Intrinsically X-ray Weak Quasar PHL 1811. II. Optical and UV Spectra and Analysis^{1,2}

Karen M. Leighly

Homer L. Dodge Department of Physics and Astronomy, The University of Oklahoma, 440 W. Brooks St., Norman, OK 73019

`leighly@nhn.ou.edu`

Jules P. Halpern

Department of Astronomy, Columbia University, 550 W. 120th St., New York, NY 10027-6601

Edward B. Jenkins

Princeton University Observatory, Princeton, NJ 08544-1001

Darrin Casebeer

Homer L. Dodge Department of Physics and Astronomy, The University of Oklahoma, 440 W. Brooks St., Norman, OK 73019

ABSTRACT

This is the second of two papers reporting observations and analysis of the unusually bright ($m_b = 14.4$), luminous ($M_B = -25.5$), nearby ($z = 0.192$) narrow-line quasar PHL 1811. The first paper reported that PHL 1811 is intrinsically X-ray weak, and presented a spectral energy distribution (SED). Here we present *HST* STIS optical and UV spectra, and ground-based optical spectra. The optical and UV line emission is very unusual. There is no evidence for forbidden or semiforbidden lines. The near-UV spectrum is dominated by very strong Fe II and Fe III, and unusual low-ionization lines such as Na I D and Ca II H&K

¹Visiting Professor, The Ohio State University, Department of Astronomy, 4055 McPherson Laboratory, 140 West 18th Avenue, Columbus, OH 43210-1173

are observed. High-ionization lines are very weak; C IV has an equivalent width of 6.6\AA , a factor of ~ 5 smaller than measured from quasar composite spectra. An unusual feature near 1200\AA can be deblended in terms of Ly α , N V, Si II and C III* using the blueshifted C IV profile as a template. Photoionization modeling shows that the unusual line emission can be explained qualitatively by the unusually soft SED. Principally, a low gas temperature results in inefficient emission of collisionally-excited lines, including the semiforbidden lines generally used as density diagnostics. The emission resembles that of high-density gas; in both cases this is a consequence of inefficient cooling. PHL 1811 is very unusual, but we note that quasar surveys are generally biased against finding similar objects.

Subject headings: quasars: emission lines—quasars: individual (PHL 1811)

1. Introduction

Strong, broad emission lines are an identifying feature of Active Galactic Nuclei (AGN) optical and UV spectra. The gas emitting these lines is illuminated and photoionized by the continuum spectrum emitted by the accretion disk and corona in the central engine. The emission line spectrum in AGN is broadly similar from object to object over many decades of luminosity. This makes sense because photoionization and thermal equilibrium tends to produce strong recombination lines, as well as strong resonance lines from easily excited abundant ions.

Different elements and ions in the line-emitting gas have a range of ionization potentials, so naively one would think that the variations in the spectral energy distribution should influence the emission-line equivalent widths and emission-line ratios. The influence is muted by the fact that many of the metal ions are excited predominately by collisions, so that the ionization state of the gas depends on the ionization parameter $U = \Phi/nc$, where Φ is the photon flux, n is the gas density, and c is the speed of light. This means that the dependence on spectral energy distribution should be a secondary effect (e.g., Krolik & Kallman

¹Based on observations made with the NASA/ESA Hubble Space Telescope, obtained at the Space Telescope Science Institute, which is operated by the Association of Universities for Research in Astronomy, Inc., under NASA contract NAS 5-26555. These observations are associated with proposal #9181.

²Based on observations obtained at Kitt Peak National Observatory, a division of the National Optical Astronomy Observatories, which is operated by the Association of Universities for Research in Astronomy, Inc. under cooperative agreement with the National Science Foundation.

1988; Casebeer, Leighly & Baron 2006). Second, the line emitting region is most probably extended and comprises gas with a range of densities (Baldwin et al. 1995). Another complication is that the broad-line region may not see the continuum that we see because some components of the central engine may radiate more isotropically than others (e.g., Netzer 1987).

Despite these complications, evidence that differences in the spectral energy distribution have an effect on the broad-line region emission and kinematics has been found recently. It is now accepted that the Baldwin effect (the empirical anticorrelation between the BLR emission-line equivalent widths and the continuum luminosity; Baldwin 1977) is a result of the softening of the spectral energy distribution in more luminous objects as a result of a larger black hole mass (see, e.g., Casebeer, Leighly & Baron 2006, for a review); the observed anticorrelation between the Baldwin effect slope and the ionization potential for each line is the most compelling evidence (Dietrich et al. 2002). The accretion rate, which also may affect the spectral energy distribution, may also influence the emission-line equivalent widths (Baskin & Laor 2004), and the fact that two properties may influence the equivalent width perhaps contributes to the large scatter in the Baldwin effect correlation. In addition, the spectral energy distribution can affect the line fluxes and equivalent widths in indirect ways. Leighly (2004) discussed the fact that an X-ray deficient spectral energy distribution better explained the broad, blueshifted high-ionization line ratios in two extreme Narrow-line Seyfert 1 Galaxies (NLS1s). Then, she showed that the narrow, intermediate-ionization lines were better explained if the continuum incident upon them had been first transmitted through the gas emitting the high-ionization lines. In addition, they found that the strong high-ionization line emission, in particular, the strong O VI line, in the low-luminosity NLS1 RE 1034+39 is a consequence of its hard spectral energy distribution (Casebeer, Leighly & Baron 2006).

This is the second of two papers that report optical, UV and X-ray observations and analysis of the nearby ($z = 0.192$), luminous ($M_B = -25.5$) narrow-line quasar PHL 1811 (Leighly et al. 2007). PHL 1811 was first cataloged as a blue object in the Palomar-Haro-Luyten plate survey (Haro & Luyten 1962). It then rediscovered in the optical followup of the VLA Faint Images of the Radio Sky at Twenty Centimeters (FIRST) survey (White et al. 1997; Becker, White, & Helfand 1995). It is extremely bright ($B=14.4$, $R=14.1$); it is the second brightest quasar at $z > 0.1$ after 3C 273. Being so bright, it is a very good background source for studies of the intergalactic and interstellar medium; furthermore, a *FUSE* observation found it to have a rare Lyman limit system which has been studied by Jenkins et al. (2003, 2005). It was odd, however, that such a bright quasar was not detected in the ROSAT All Sky Survey (RASS). In comparison with other quasars of its luminosity, the expected RASS count rate is about 0.5 s^{-1} ; we placed an upper limit of

1.3×10^{-2} counts s $^{-1}$ (Leighly et al. 2001). A pointed *BeppoSAX* observation detected the object, but it was still anomalously weak. Too few photons were obtained in the *BeppoSAX* observation to unambiguously determine the cause of the X-ray weakness; Leighly et al. (2001) speculated that either it is intrinsically X-ray weak, or it is a nearby broad-absorption line quasar and the X-ray emission is absorbed, or it is highly variable, and we observed it both times in a low state.

In the companion paper (Leighly et al. 2007, hereafter Paper I), we reported the results of five X-ray observations of PHL 1811 using *Chandra*, *XMM-Newton*, and *Swift*. We also reported the simultaneous UV photometry using the OM on *XMM-Newton* and the UVOT on *Swift*, as well as optical photometry obtained at the MDM observatory. These observations confirmed that PHL 1811 is an anomalously X-ray weak quasar. The X-ray spectrum is steep, with photon index between 2 and 2.6, and there is no evidence for absorption in excess of the Galactic H I column. The X-ray flux varied by a factor of ~ 5 among the 5 observations, but the UV photometry, when compared with the *HST* spectrum presented and analyzed in this paper, showed no detectable variability. The inferred α_{ox} , defined as the point-to-point slope between 2500Å and 2 keV, is measured to be -2.3 ± 0.1 . Typical quasars with PHL 1811’s optical luminosity have α_{ox} of -1.6 (Steffen et al. 2006). Accounting for scatter, this means that PHL 1811 is between 13 and 450 times fainter in X-rays than other quasars with the same UV luminosity. Along with the *ROSAT* All Sky Survey upper limit and the *BeppoSAX* observation, we have now observed PHL 1811 in X-rays seven times and it is always found to be X-ray weak. While we can never disprove the hypothesis that we coincidentally always observe it in a transient low state, the odds of that being true are decreasing. We concluded in Paper I that PHL 1811 is the best example of an intrinsically X-ray weak quasar. We present an updated spectral energy distribution of PHL 1811 in Paper I and discuss possible reasons for its X-ray weakness.

In this paper, we present *HST* STIS UV and optical spectra, and ground-based optical spectra obtained at the KPNO 2.1 meter telescope (§2). As shown in §3, the emission-line properties of PHL 1811 are very unusual. There are no forbidden or semi-forbidden lines, and the high-ionization lines are weak. The spectra are dominated by low-ionization lines, and Fe II and Fe III are strong. In §4 we investigate, using *Cloudy* models, the physics of gas illuminated by an X-ray weak spectral energy distribution (SED). It turns out that gas illuminated by a soft SED has much different properties than gas illuminated by a normal SED, and furthermore, many of the peculiar features of the optical and UV spectra of PHL 1811, including the lack of semiforbidden lines, can be explained by this single factor. We summarize the principal results of the paper in §5. We also include a brief Appendix in which we explore additional properties of the soft SED that are not directly related to the observations. Some of the results have been published in Leighly, Halpern & Jenkins

(2004). We assume a flat Universe with $H_0 = 70 \text{ km s}^{-1} \text{ Mpc}^{-1}$ and $\Omega_{vac} = 0.73$, unless otherwise specified.

2. Optical and UV Observations and Analysis

The *HST* observations were reduced using the standard pipeline. To reduce the effects of any possible fixed-pattern noise, four exposures with each of the chosen MAMA gratings were made with the target stepped along the slit. The separate exposures for each detector were each cross correlated with a preliminary average spectrum to search for any systematic offsets; none were found. The average spectrum was then computed using the *IRAF* task `scombine` and resampled to a linear binning. The *HST* STIS CCD observation was split into two separate exposures in order to aid in the rejection of cosmic rays.

We presented an optical spectrum taken at the MMT telescope in 1997 in Leighly et al. (2001). We obtained several other spectra at KPNO that have better resolution and signal-to-noise ratios that we present here (Table 1). Two of the KPNO spectra were taken within 1.5 months of the *HST* and *Chandra* observations.

To check the wavelength calibration of the UV spectra, we fit Galactic absorption lines (FUV: Si II $\lambda 1260, \lambda 1527$; C II $\lambda 1335$; C IV $\lambda 1548, 1551$; NUV: Mg II $\lambda 2796, 2804$; Fe II $\lambda 2344, 2374, 2383, 2567, 2600$). We find that the FUV spectrum is consistent with no systematic shift. However, all five lines in the NUV were offset from their rest wavelengths by 1.0–1.7 Å. To rectify this, the wavelength scale in the NUV was adjusted blueward by 1.35 Å (the mean of the shifts of the seven NUV lines).

There were no convenient absorption lines available to check the wavelength calibration in the *HST* STIS CCD and ground-based optical spectra. Assuming no systematic shifts does not lead to any anomalous or unexplainable results (see below) so we assume that the wavelength calibration in these spectra is satisfactory.

The *HST* spectra are all given in the vacuum wavelengths; we convert the optical spectra to vacuum wavelengths uniformly for consistency.

We next estimate the redshift of the object. There is no prominent emission feature in the FUV spectrum that could confidently be considered to be emitted at the rest wavelength. There is, however, a weak absorption line that Jenkins et al. (2003) speculated originates in Ly α in the rest frame of the object. This absorption line gives an estimate of the redshift of $z = 0.1903$. Interestingly, however, in the medium resolution *HST* spectra, there can be seen two lines near the Ly α restframe; one is consistent with a redshift of 0.1901, and another,

smaller one that does not appear in the low resolution data is consistent with a redshift of 0.1920. Alternatively, these may originate in galaxies other than the quasar host that are in the same group.

In the NUV spectrum, there is a narrow emission line clearly originating in Fe II UV191. The three multiplet components are closely spaced, lying within 3Å of one another; the gf_{ij} weighted average wavelength is 1786.2Å. Fitting this feature in the NUV spectrum gives an estimated redshift of $z = 0.1900$. In the *HST* CCD spectrum, we may consider Mg II to be emitted at the rest wavelength; it gives an estimate of the redshift of 0.1920. The Balmer lines in the optical spectra also give estimates near this value (0.1919 estimated from H α in the July spectrum; 0.1924 estimate from H β in the October blue spectrum; 0.1923 from H β in the October red spectrum; 0.1921 from H α in the October red spectrum). Note there is no observed [O III] or any other narrow-line region emission line. Thus, we see a difference in the estimated redshift between the UV and optical spectra by 0.002. This corresponds to wavelength shifts of 2.9Å at observed frame Ly α , 4.3Å at Fe II UV191, and 6.7Å at Mg II. The estimated wavelength calibration uncertainty, obtained from the STIS data handbook (Kim Quijano et al. 2003), is 0.5–1.0 pixel in the MAMA and 0.2–0.5 pixel in the CCD. This corresponds to 0.3–0.6Å in the FUV spectrum, 0.8–1.6Å in the NUV spectrum, and 0.5–1.4Å in the CCD spectrum – much smaller than the shift required to explain the $\Delta z = 0.002$ between the redshift estimates. Therefore, we assume that the Balmer and Mg II lines are most likely to reflect rest wavelength of the object, we take the redshift to be $z=0.192$, and assume that the Fe II UV191 is blueshifted.

We next construct a merged spectrum using the *HST* and ground-based spectra. For the *HST* spectra, we start at the far UV end and successively adjust the normalization and construct average, resampled spectra in the overlap regions. The absolute photometry is estimated to be 4% and 5% for the MAMA and CCD spectroscopy, according to the STIS data handbook. We found good agreement in the overlap regions throughout the FUV, NUV and optical HST spectra.

Turning to the ground-based spectra, we found that the October red and blue KPNO spectra were consistent in slope and normalization. However, the July red spectrum had better SNR than the October red spectrum, and we wanted to use it. It had a slight difference in slope compared with the July spectrum. We resample the overlap region, which was most of both spectra, onto the same wavelength binning, divided the two, fit a quadratic function to the result and correct the slope difference in the July spectrum. We then merge the October blue spectrum with the corrected July red spectrum.

Next, we merge the *HST* and KPNO spectra. The *HST* spectrum is brighter by about 30%, most likely because of slit losses in the KPNO spectra, and there was also a small

difference in slope. We resampled the overlapping regions onto the same wavelength scale, fitted the ratio to a 9-node spline and corrected the KPNO spectrum to match the slope of the *HST* spectrum.

Finally, we deredden the merged spectrum using $E(B - V) = 0.046$, estimated from the infrared cirrus (Schlegel, Finkbeiner, & Davis 1998) and the Cardelli, Clayton & Mathis (1989) reddening law, and apply the redshift correction ($z = 0.192$), and

The merged spectrum is shown in Fig. 1. Except for the small absorption line near rest-frame Ly α , the other prominent absorption lines are all from our Galaxy or from intervening galaxies; they are all identified in Jenkins et al. (2003), and the reader is referred to that paper for the identifications. Emission lines expected from active galaxies are marked. We also mark emission lines from a particular type of ion - those in which the lowest excited level has $\Delta S \neq 0$ compared with the ground state, but rather that transition to the ground state is semiforbidden. These ions include Si $^{+1}$, Si $^{+2}$, C $^{+2}$, and Al $^{+1}$. The emission lines that we mark are those that have the first excited level as the lower level. This type of line is analogous to auroral lines, except that the metastable transitions to ground are semiforbidden rather than forbidden. The motivation for looking at these lines is discussed in §3.3.2.

3. Emission-line Properties

In this section, we discuss the optical and UV emission-line properties of PHL 1811. We organize the discussion by moving shortward in the spectrum: we first discuss the optical emission lines, then the near UV, and finally the far UV lines.

To model the spectra, we use a combination of the IRAF task `Specfit`, and programs that we developed ourselves written in IDL. `Specfit` requires 1-sigma error bars on the spectra, which are not available for the optical spectra. The signal-to-noise ratio in the continuum of the optical spectra is greater than 30, so fit results are not dominated by statistics. We estimate uniform 1-sigma errors as the standard deviation in line-free segments of the data, and interpolate between these estimates.

3.1. Optical Emission-line Properties

We use the merged spectrum to analyze the emission-line properties. Fig. 2 displays the region of the spectrum near H β and H α . The strong emission lines from Fe II that are common in NLS1s are clearly seen. In order to determine which lines besides Fe II are present in the spectrum, and to measure the properties of the Balmer lines, we perform

an Fe II template subtraction, as is commonly done (e.g., Boroson & Green 1992; Leighly 1999b) using a template obtained from the prototypical NLS1 I Zw 1. We use two different templates. The first one is the Boroson & Green (1992) template with a few additional iron lines added in the blue by Dirk Grupe. The second one was recently developed by Véron-Cetty, Joly, & Véron (2004). Each template is broadened by convolution with a Gaussian with $\text{FWHM} = 400 \text{ km s}^{-1}$, scaled appropriately, and subtracted from the spectra. Neither template matches the Fe II emission in the region of $\text{H}\beta$ very well (Fig. 2). We note that this might be expected for the Véron-Cetty, Joly & Véron template, since those authors remove forbidden Fe II emission, leaving only permitted Fe II in their template.

The Boroson & Green (1992) template produces a better fit in the vicinity of $\text{H}\beta$, so we use that spectrum for further analysis in that region. Véron-Cetty, Joly, & Véron (2004) identified Fe II usually hidden in the base of $\text{H}\alpha$, and therefore their template yields an $\text{H}\alpha$ line with a narrower, more symmetric base. The $\text{H}\alpha$ and $\text{H}\beta$ line profiles have extended wings and clearly can not be modeled using a Gaussian. We use a Lorentzian profile plus a local linear continuum to fit them. The results are given in Table 2.

We clearly observe $\text{H}\gamma$, and report the results of the Lorentzian fit to this line in Table 2. However, because the Fe II subtraction is really not very good in the region of this line, we do not consider these results to be very reliable.

The optical spectra contain very few other lines besides hydrogen Balmer lines and Fe II. He II $\lambda 4686$ is not apparent, although it could be present if it is weak and masked by the imperfect Fe II subtraction. There is no trace of the generally strong narrow-line region line, [O III] $\lambda 5007$, or any other narrow-line region line. There is an excess near 6350 \AA that can be seen after subtraction with the Véron-Cetty, Joly, & Véron template (Fig. 2). Based on the line identifications for I Zw 1 made in Véron-Cetty, Joly, & Véron (2004), this could be Si II $\lambda\lambda 6347.10, 6371.40$.

The most interesting lines that are seen in the optical part of the spectrum are the very low ionization lines Na I D and Ca II H& K. The Na I D $\lambda\lambda 5889.89, 5895.89$ doublet is frequently blended with the He I $\lambda 5875.70$ (e.g., Thompson 1991), but in this case, as seen in Fig. 3, we are fairly confident that the entire feature is Na I D and no He I is present. We modeled the feature in two ways, using the Veron-template-subtracted spectrum. First, we modelled the doublet with two Lorentzians of equal flux, width and fixed separation. The results of this model comprises the entry for Na ID in Table 2. Notably, we find that the mean wavelength of the doublet, which would be the weighted mean of the feature if the gas were very optically thick to the line, is equal to the lab value. The second model includes an additional Lorentzian to model He I also. The separations of the lines were fixed, and the widths and fluxes of the Na ID lines were constrained to be equal (as before). Since we

do not see He I, we constrain the fit by assuming that the width is the same as that of H α , although we note that it is observed to be somewhat broader in Seyfert galaxies (Crenshaw 1986). The improvement in the fit was not significant ($\Delta\chi^2 = 1.2$ for 201 fitted points), and the uncertainty on the flux of the He I component is almost as large as the flux (i.e, relative uncertainty is 90%). In addition, the mean wavelength for the Na ID line is now redward of the lab wavelength, although it is still consistent with that value. We conclude that He I is not detected, and evaluate the upper limit by varying the normalization until the χ^2 is larger by 6.63 (99% confidence for one parameter of interest). In addition, we search for He I $\lambda 7067$. We find no evidence for it, and we estimate the upper limit in the same way. The results are given in Table 2.

The weakness of He I $\lambda 5876$ is physically interesting. Crenshaw (1986) tabulate the fluxes of He I and H α for 9 Seyfert galaxies; the mean He I/H α ratio is 0.061. Thompson (1991) tabulate He I/H α ratio for 6 quasars, and the mean ratio is 0.025. We measure an upper limit on the ratio of 0.0062 in PHL 1811. Such a low ratio is difficult to explain using photoionization models; we address this issue in §4.4.

The strength of Na ID is also interesting. Thompson (1991) discussed the presence of this line in quasars. The ionization potential of Na $^+$ is only 5.14 eV, so rather special conditions are necessary to produce this line. Using *Cloudy* models, he found that a very high column density was necessary to shield the neutral sodium from photoionization in order to produce sufficiently large Na ID/H α .

Turning to the Ca II H& K doublet, we initially modelled these lines as Lorentzians, as the other lines are. The line widths are then found to be only $770 \pm 83 \text{ km s}^{-1}$, about half the width of the other lines. Gaussian profiles fit these lines somewhat better ($\Delta\chi^2 = 15.4$ for 152 points), and the widths are still somewhat narrow ($980 \pm 80 \text{ km s}^{-1}$). Indeed, if we overlay their profiles on that of H β (Fig. 4), they appear to be narrower than that line. The Na I D lines are also somewhat narrower than H α ($1365 \pm 180 \text{ km s}^{-1}$), although we model those with a Lorentzian profile.

Observations of the Ca II infrared triplet in AGN were reported by Persson (1988). He found that these lines were detected in at least nine of the forty objects surveyed, and that the line strengths were roughly correlated with the optical Fe II. Interestingly, reports of observations of Ca II H&K are rather rare (Ferland & Persson 1989), although we note the recent detection of these lines in IRAS 07598+6508 by Véron-Cetty et al. (2006). Ferland & Persson (1989) and Joly (1989) present models that show that very large column densities are required to produce the observed infrared triplet emission. There are two hypotheses for the weakness of the Ca II H&K lines in most AGNs. First, the structure of the Ca $^+$ ion is similar to the Fe $^+$ ion. In each case, there are resonance transitions to a

high level, which decay back to the ground state, or to an intermediate metastable state. Some of the UV Fe II lines and the Ca II H&K lines correspond to the resonance transitions to the high level, while the optical Fe II lines and the Ca II IR triplet correspond to the decay to the intermediate metastable state. Thus, just as scattering of the UV Fe II lines reprocess the iron emission into optical Fe II lines (Kwan & Krolik 1981), scattering in a high-column-density gas converts the Ca II H&K lines into the infrared triplet. Alternatively or in addition, absorption in the host galaxy may make Ca II H&K in emission difficult to detect. Regardless, the similarities between Ca⁺ and Fe⁺ suggest that the study of Ca II may be a profitable way to understand the physical conditions of the low-ionization line-emitting region in AGN, as Ca⁺ is a much simpler atom than Fe⁺.

The Ca II lines are well resolved, so in principle we can try to constrain the optical depth of the line-emitting region. We fit the lines with equal width and a fixed separation, but allow their fluxes to be independent. We find that the K component flux is then larger than the H component flux, and the ratio between the two is measured to be 1.28. The gf values are 1.36 and 0.66 for K and H, respectively, thus predicting a ratio equal to 2 for optically thin gas. We note that there is some uncertainty in the measurement of the line fluxes because the continuum is not smooth and is difficult to identify; however, the line ratio can be seen by eye to closer to one than to two. Laor et al. (1997b) measure the ratio between the similar Mg II doublet components in I Zw 1 to be 1.2. Mg II is isoelectronic with Ca II and these lines are both transitions from the lowest-level excited state to the ground state, so the interpretation of the low ratio should be similar. In both cases it means that the gas is sufficiently optically thick that enough scatterings occur to redistribute the lines; the ratio would be 1 to 1 if completely optically thick.

The ratio of Fe II to H β is a parameter frequently used to describe the strength of the Fe II emission. As was done in Boroson & Green (1992) and Leighly (1999b), we integrate the subtracted Fe II model between 4344 and 4684 Å. Dividing the flux measured from the model by the integrated and modeled H β fluxes yields an estimated ratio in the range of 1.22–1.35. Comparing with the sample of NLS1s reported in Leighly (1999b), we find that the estimated ratio for PHL 1811 is in the middle of the range reported there, but somewhat larger than the median and mean (1.0 and 1.1, respectively). Thus, PHL 1811 is a moderately strong Fe II emitter.

In summary, we find that the optical spectrum from PHL 1811 contains prominent Balmer and Fe II lines, similar to many other NLS1s. The spectrum is somewhat unusual in that there are no forbidden lines; in particular the generally strong [O III] λ 5007 line is absent. NLS1s are identified by their weak forbidden lines, and a few other objects appear to have no [O III] also (e.g., RX J0134.2–4258, Grupe et al. 2000). There are

no high-ionization coronal lines which sometimes appear in optical spectra of NLS1s (e.g., Dietrich, Crenshaw, & Kraemer 2005). PHL 1811 is unusual in that it shows prominent very low-ionization lines from Na ID and Ca II H&K, but no He I.

3.2. The Near-UV Spectrum

The near UV portion of the spectrum of AGN, between around 1600 Å and 3500 Å, generally exhibits strong and prominent emission lines from C III] λ 1909 and Mg II λ 2800. A pseudocontinuum of Fe II may also be present over the entire region, and is most prominent between 2200 and 3050Å. Fe III and Fe I may also contribute. Good signal-to-noise spectra often reveal contributions from numerous weak semiforbidden lines of oxygen, nitrogen, silicon, and carbon. The near UV spectrum from PHL 1811 is different from many AGN in that no semiforbidden or forbidden lines are observed. The spectrum is strongly dominated by Fe II and Fe III.

3.2.1. *Mg II, Fe II and Fe III in PHL 1811*

The properties of UV Fe II and Mg II in Active Galactic Nuclei (AGN) are important diagnostics for several reasons. Luminous quasars are probes of the early Universe. As discussed by Hamann & Ferland (1993) and others, the production of iron is thought to lag that of the α elements including magnesium due to different formation mechanisms: magnesium and about half of the iron (Nomoto, Nakamura, Kobayashi 1992) are produced in supernovae of massive, rapidly-evolving stars, while the remainder of the iron is produced largely in Type 1a supernova which are triggered by accretion onto a white dwarf, and are delayed with respect to core-collapse supernova. Observation of an evolution of the [Fe/Mg] ratio with redshift could constrain the time of the first burst of star formation in the Universe. The UV Fe II and Mg II are found conveniently near one another in the rest-UV bandpass, and they should both be produced in gas with similar properties, so it was thought that the Fe II/Mg II ratio could be an abundance diagnostic. No clear evidence for Fe II/Mg II ratio evolution has been observed yet (e.g., Dietrich et al. 2003).

As in the optical bandpass, the flux and equivalent width of Fe II are frequently measured using a template (e.g., Corbin & Boroson 1996; Forster et al. 2001; Dietrich et al. 2002; Leighly & Moore 2006). We developed a UV Fe II template from the *HST* spectrum of the prototypical Narrow-line Quasar I Zw 1, following Vestergaard & Wilkes (2001): we subtracted a power law identified at the relatively line-free regions near 2200Å and 3050Å;

absorption lines and prominent emission lines not attributable to Fe II were then subtracted.

Using this template, we recently measured the Fe II/Mg II ratio in the spectra from 903 intermediate-redshift narrow-line quasars from the Sloan Digital Sky Survey (Leighly & Moore 2006). In most of those spectra, the template modelled the iron quite well in the 2200–3090 Å bandpass. However, when we try to apply the template to PHL 1811, we cannot obtain a good fit. While the region of the spectrum around Mg II matches the template well, there is significant excess emission at shorter wavelengths. To illustrate this problem, we adopt a strategy frequently used by X-ray astronomers: we fit the spectrum with a linear model, the iron template, and two Gaussians to model the Mg II doublet in the ~ 2650 –3090 Å bandpass. Then, we extrapolate the model to shorter wavelengths. The result is shown in Fig. 5a for PHL 1811. It is interesting that the template and continuum match the dip around 2250Å fairly well, but there is significant excess emission between 2300Å and 2500Å and shortward of 2250Å.

For comparison, we perform the same analysis on the spectra of several other quasars and a composite spectrum. In Fig. 5b we show I Zw 1. Naturally, the template fits the spectrum perfectly. Next, we show the largest Fe II/Mg II composite from Leighly & Moore (2006, shown in their Fig. 6). In this case and for the next case, we ignore the wavelengths containing the prominent emission from Fe II UV 62 and UV 63, low-lying transitions that sometimes produce strong emission near 2760 Å, and trim the fitted bandpass. Finally, we show the spectrum of SDSS J105023.68-010555.5. The template matches the data rather well for both of these spectra. In Fig. 5a, however, we compare PHL 1811 with the *HST* FOS spectrum of the luminous NLS1 RX J0134.2–4258 (e.g., Grupe et al. 2000), and the spectrum of SDSS J094257.80-004705.2. In both of these objects, like PHL 1811, extrapolation of the template leaves prominent excess emission at short wavelengths.

What is the origin of the short wavelength excess in PHL 1811 and the other objects? In Fig. 6, we show the spectrum of PHL 1811 along with the upper level energies of transitions of Fe II and Fe III between 1000 and 3500 Å; the atomic data was obtained from Kurucz Atomic Line Database³. Around 2000Å, there are many Fe III transitions with large Einstein A_{ij} coefficients. These include the multiplets from low-lying levels such as Fe III UV 34 near 1900Å and Fe III UV 48 near 2060Å, which are seen as excesses in the spectrum. But there are also many more transitions with upper level energies between 15 and 19 eV. Thus, it may be that strong Fe III contributes to the excess shortward of 2250Å.

Between 2300–2500Å, there are no high A_{ij} transitions of Fe III. Fe II is more prominent in this region. The principal low-lying transitions with high A_{ij} values between 2300 and 2500

³<http://cfa-www.harvard.edu/amdata/ampdata/kurucz23/sekur.html>

Å are UV 2 near 2400 Å, UV 3 near 2340 Å, and UV 35 and UV 36 near 2380 Å. With upper level energy of only 5–6 eV, these are candidates for the short wavelength excess emission. However, UV 1 near 2610 Å, UV 62 and 63 near 2750 Å, and UV 64 near 2570 Å also have upper level energies near 5–6 eV, and so one might expect these to be enhanced also. These transitions, and especially UV 62 and UV 63 are sometimes quite strong in some narrow-line quasars (e.g., SDSS J105023.68-010555.5 in Fig. 5b; also Hall et al. 2004), but they do not appear to be excessively strong in PHL 1811 or in the objects in Fig. 5a. However, Fig. 6 shows that there exists many higher-excitation Fe II transitions with high A_{ij} values that produce emission in this region. Especially near 14 eV, there is a large concentration that is centered between 2300–2500 Å, and we propose that it is this high-excitation Fe II emission that contributes to the Fe II pseudocontinuum so strongly in PHL 1811 and similar objects.

Combined with the strong Fe III emission, the strong Fe II emission from high energy levels suggests that the iron in PHL 1811 and similar objects is characterized by a relatively higher ionization/excitation than in other objects. At first sight, this is a puzzling result, because the soft spectrum implies that the energy per ionizing photon is relatively low; using the PHL 1811 continuum developed for *Cloudy* simulations, we obtain an average energy per photon of only 19 eV. Also, the lack of hard X-rays implies that the partially ionized zone, where Fe II emission is thought generally to be emitted, will be quite shallow. But as we show in §4.3, it turns out that strong Fe II and Fe III are consequence of the soft spectral energy distribution through several mechanisms: the gas in the H II region is dominated by intermediate-ionization species, including Fe^{+2} , there is strong continuum pumping of the Fe^+ ion, and there is strong Ly α pumping associated with strong continuum emission in the partially-ionized zone.

The Mg II is rather weak in PHL 1811, although in some sense it appears strong because it is prominent in comparison with the other lines. We find that the equivalent width is just 12.9 Å. In comparison, the equivalent widths from composite spectra are 50 Å (Francis et al. 1991), 64 Å (Zheng et al. 1997), and 34 Å (Brotherton et al. 2001). In §4.1.3 we show that the low equivalent width for this collisionally excited line is plausibly a consequence of the low temperature in the line-emitting gas.

Finally, we measure the UV Fe II/Mg II flux ratio, which, as noted before, is used as an abundance diagnostic in quasars. As shown above, the I Zw 1 template does not fit the UV Fe II spectrum in PHL 1811 well. Therefore, to measure the flux of this component, we define the continuum, subtract a powerlaw model, integrate over the remainder from 2000 to 3000 Å (the Fe II UV band defined by Verner et al. 2004), and subtract the flux of the Mg II line. Defining the continuum is difficult. As noted by Verner et al. (2004), there is a gap in the Fe II emission at around 3050 Å, but then a pseudocontinuum of varying amplitude

continues to at least $\sim 1000\text{\AA}$. That pseudocontinuum is relatively low at 1800 or 2000 \AA , so to obtain a lower limit on the Fe II emission, we define two continua: from 1800–3050 \AA and from 2000–3050 \AA . The Fe II UV/Mg II flux ratios obtained this way are 14.9 and 13.7 for the 1800–3050 and 2000–3050 \AA continua, respectively. These estimates are uncertain because some Fe III emission may be contained in the Fe II flux estimate, which would tend to decrease the ratio. In addition, there is some uncertainty in the Mg II emission-line flux, since Fe II template that was used assumes no Fe II emission under the Mg II; if there were Fe II under Mg II, the Fe II/Mg II flux ratio would be larger (see Leighly & Moore 2006, for a discussion of this point). For comparison, we found a maximum likelihood mean and 1σ dispersion of the Fe II/Mg II ratio of 3.93 ± 0.95 in the 903 SDSS quasar spectra analyzed in Leighly & Moore (2006). Note that in that paper the Fe II flux was integrated between 2200 and 3050 \AA . Thus, PHL 1811 shows an enhanced Fe II/Mg II flux ratio, and enhanced UV Fe II emission compared with other quasars.

3.2.2. No Semi-forbidden Lines in PHL 1811

Fig. 7 shows a portion of the near-UV spectrum from PHL 1811. The *HST* spectrum of the prototypical NLS1 I Zw 1 is also shown. The positions of permitted, semiforbidden, and forbidden emission lines commonly seen in AGN are marked. Prominent Fe II and Fe III lines are marked, although as discussed above, blends of lines from the same ions produce a strong pseudocontinuum. Absorption lines that are present all originate in our Galaxy.

The most prominent difference between these two spectra is the relative weakness of all emission features in the spectrum of PHL 1811. In most AGN, C III] $\lambda 1909$ is one of the strongest emission lines; the equivalent width of the 1900 \AA feature in quasar composite spectra is around 20 \AA (Francis et al. 1991; Brotherton et al. 2001). In I Zw 1, C III] is weak relative to Si III], perhaps because of a higher density in the broad-line region (e.g., Laor et al. 1997b). In the spectrum of PHL 1811, there is a bump near the expected position of C III]. However, as the inset figure shows, the central wavelength of that feature is somewhat longward ($\sim 1915\text{\AA}$) of the expected wavelength for C III]. Its wavelength matches that of the Fe III $\lambda 1914.1$ emission line, part of the Fe III UV34 triplet (1894.8 \AA , 1914.1 \AA , 1926.3 \AA) more closely. As discussed in Leighly & Moore (2004), the optically thin ratios of the lines in this triplet should be 1:1.4:1.8. However, in some objects in the sample considered by Leighly & Moore (2004), the 1914 \AA component was strongly enhanced. The upper level energy of this transition corresponds to 1214.6 \AA , which is just 1.1 \AA from Ly α . Therefore, it is quite plausible that if microturbulence is present in the line-emitting gas, this line may be strongly pumped by Ly α (also Johansson et al. 2000). We suspect that

this phenomenon is occurring in PHL 1811, so that the feature near 1914Å is Fe III, and C III] is not present.

It is not straightforward to obtain an upper limit on C III] because of the complicated iron emission in the region. We assign the conservative upper limit recorded in Table 2 as follows: we assume that our identification of the 1915Å feature is mistaken, and it is really C III]. We identify as pseudocontinuum on each side of that feature and integrate over it to obtain the flux.

The lack of semiforbidden lines in PHL 1811 naturally suggests that the emitting gas has a high density. Of the six semiforbidden lines (O III] λ 1664, N III] λ 1750, Si III] λ 1892, C III] λ 1909, N II] λ 2142, and C II] λ 2326) in the region of the spectrum shown in Fig. 7, Si III λ 1892 has the highest critical density ($3 \times 10^{11} \text{ cm}^{-3}$; Hamann et al. 2002). However, as we show in §4, density indicators break down for gas illuminated by a soft spectral energy distribution (SED). In fact, the lack of semiforbidden lines can be completely attributed to the soft SED. Semiforbidden lines are collisionally excited, and collisionally-excited lines are weak in gas illuminated by a soft SED as a consequence of a low gas temperature.

3.2.3. Other Near-UV Line Emission

We clearly see the Fe II UV 191 feature in the spectrum. This triplet (1785.277, 1786.758, 1788.004Å) originates in a high-excitation state; the upper level energy is 9.8 eV. This line is prominent in stellar spectra; the excitation mechanism is not known. Dielectronic recombination has been suggested as a possible mechanism (Johansson & Hansen 1988). That mechanism might be consistent with our hypothesis, presented in §3.2.1, that the near-UV line emission is dominated by Fe^{+3} and high-excitation Fe II. We model this line with three Gaussian components fixed at their expected optically thin relative fluxes of 2.0:1.5:1.0 (Johansson et al. 1995). The best fitting gf weighted wavelength of the feature is 1783.2Å. Because this feature is so narrow, it can be seen to be clearly blueshifted (by 570 km s^{-1}) from the expected gf weighted wavelength of 1786.4Å. A blueshift in a narrow, low-excitation line is not expected. Perhaps this is telling us something about the emission mechanism?

We also identify Al III $\lambda\lambda$ 1854.7, 1862.8. We model this feature with two Gaussians with equal widths, fluxes and a fixed distance between. We measure a relatively large width (Table 2; 3050 km s^{-1}), and large redshift (1340 km s^{-1}). While the large widths and shifts may be real, it is also quite possible that the line is blended with other emission lines. An attractive possibility are the “unexpected UV” lines at 1870Å and 1873Å resulting from Ly α pumping of Fe II (e.g., Rudy et al. 2000). We note that there seems to be a small blue

shift from the marked rest-wavelength position in I Zw 1 for both Fe II UV 191 and Al III (Laor et al. 1997b).

We also notice an excess in the spectrum at 1750Å that could be the resonance transition of Ni II. In most AGN, that line would be hidden under the N III] multiplet; however, in this object, since other semiforbidden lines are conspicuously weak, there is no reason to suspect that N III] is present.

As will be discussed in §3.3.2, we infer prominent Si II emission from multiplets near 1263Å and 1194Å. As discussed in Baldwin et al. (1996), if these emission lines are produced by collisional excitation, we expect to see emission from lower-lying resonance transitions near 1815Å and 1531 Å, neither of which are observed. The 1531 Å line is difficult to identify, because it is hidden under C IV. We obtain an upper limit to the 1815Å line by fitting with the C IV template, described in §3.3.1, fixed at the expected wavelength. We then vary the flux of the template until we obtain χ^2 larger by 6.63, which corresponds to 99% confidence for one parameter of interest. We note that our upper limit is conservative; because the spectrum is complicated in this region, we are forced to constrain the fit over only a narrow bandpass and therefore cannot constrain the continuum very well.

3.3. The Far-UV Spectrum

The far UV continuum and emission lines are both unusual in PHL 1811. Typical quasars show a break to a flatter spectrum at $\sim 1000\text{\AA}$, as is seen in a composite spectrum constructed from *HST* spectra of quasars (Zheng et al. 1997; Telfer et al. 2002). A break in this vicinity is also observed in the spectral energy distributions of individual low-redshift objects (Shang et al. 2005), which means that the break cannot be a consequence of Ly α forest absorption. Fig. 8 shows the broadband continuum spectrum of PHL 1811 in comparison with the Francis composite spectrum (Francis et al. 1991). We see no evidence for a break down to 970Å, the extent of the *HST* spectrum. The continuum is possibly a power law over the entire optical-UV bandpass, with a large contribution from Fe II and Fe III between 2000 and 3200Å. Alternatively, a rollover might be present at $\sim 2500\text{\AA}$, a longer wavelength than usual.

Ly α is generally a strong and prominent line in AGN spectra. Since it is a recombination line of hydrogen, it is expected to be strong in photoionized gas. The equivalent width of Ly α plus N V in composite spectra is found to be ~ 50 to ~ 90 Å (Francis et al. 1991; Zheng et al. 1997; Brotherton et al. 2001). In addition, C IV is generally observed to be very strong as well. C IV is expected to be strong because C $^{+3}$ is easily excited by

collisions. Composite spectra reveal a C IV equivalent width of 33–59Å (Francis et al. 1991; Zheng et al. 1997; Brotherton et al. 2001). In PHL 1811, C IV and a feature near Ly α are observed, but their equivalent widths are small (Table 2; see below).

Although PHL 1811 has an unusual far-UV spectrum, it is not a unique object. Fig. 9 shows the spectra from two other high-luminosity narrow-line quasars: RX J0134.2–4258 (Goodrich 2000) and PHL 1092 (Leighly et al. in prep.). All three objects show low equivalent-width emission lines and blue far-UV spectra. For comparison, the *HST* composite spectrum (Zheng et al. 1997), the spectrum from the NLS1 1H 0707–495 (Leighly & Moore 2004; Leighly 2004), and a spectrum from the well-studied broad-line Seyfert 1 galaxy, NGC 5548 (Korista et al. 1995) are shown.

3.3.1. The C IV Line, He II λ 1640, and 1400 Å Feature

Fig. 10 shows the region of the spectrum that includes the C IV line. This line was somewhat difficult to analyze, because the continuum was difficult to identify. However, there is a relatively flat region longward of the C IV line that stretches to 1800Å that we could plausibly identify as the continuum.

As discussed in Leighly et al. (2001), and in Paper I, PHL 1811 is X-ray weak. Brandt, Laor, & Wills (2000) investigated soft X-ray weak objects among the Boroson & Green (1992) sample of PG quasars. They found that soft X-ray weak objects frequently show significant C IV absorption lines; in fact, they showed that there is a trend for the most X-ray weak objects to have the largest equivalent-width absorption lines. They postulated that soft X-ray weakness is caused by photoelectric absorption of the X-rays by the same gas that is responsible for the C IV absorption lines. Indeed, in many cases, deep X-ray observations find that the signature of absorption is present in the X-ray spectra of soft X-ray weak objects (Gallagher et al. 2002). Since PHL 1811 is X-ray weak, we might expect to observe C IV absorption lines, and based on Brandt, Laor, & Wills (2000), we might expect an absorption line equivalent width of up to 20Å. But as seen in Fig. 10, although the spectrum is noisy, no evidence for a C IV absorption line is seen. There are negative fluctuations at the positions of resonance lines from gas in our Galaxy, namely Si II λ 1808 (seen at 1516.8Å) and possibly from Al III $\lambda\lambda$ 1854.7, 1862.8 (seen at 1556 and 1562.8 Å). There is another negative fluctuation at 1529.3 Å that we identify as C IV absorption from the $z(abs) = 0.17651$ intervening system (Jenkins et al. 2003). Thus PHL 1811 is not a typical soft X-ray weak object, and therefore we do not conclude that the soft X-ray weakness is a consequence of absorption.

Fig. 10 shows the C IV emission line is blueshifted and asymmetric. Following the pro-

cedure discussed in Leighly & Moore (2004), we create a template from the C IV line. The template fit, and the separate components, are shown overlaid on the C IV line. The shape of the PHL 1811 template is quite similar to the shape of the templates obtained IRAS 13224–3809 and 1H 0707–495; given the lower equivalent width of the C IV line, and noiser spectra, they are essentially identical. To illustrate this, we overlay the IRAS 13224–3809 profile on Fig. 10.

The equivalent width of the C IV line is exceptionally low; we measure it to be just 6.6Å. As discussed in Leighly & Moore (2004), C IV equivalent widths are much larger in composite spectra; Francis et al. (1991), Zheng et al. (1997), and Brotherton et al. (2001) measured C IV equivalent widths of 37, 59, and 33Å respectively. Fig. 8 compares the PHL 1811 C IV line with that from the Francis composite (Francis et al. 1991); it is a factor of > 5 smaller. The two NLS1s, IRAS 13224–3809 and 1H 0707–495, analyzed in Leighly & Moore (2004) had low equivalent width of 13–15Å; the C IV equivalent width in PHL 1811 is about half that. Leighly (2004) found that the weak C IV lines in those two NLS1s, along with other unusual emission-line ratios, could be explained by a combination of high metallicity and an X-ray weak continuum. In §4 we show that the soft SED is responsible for the weak C IV in PHL 1811.

PG 1407+265 is a quasar that has low-equivalent width high-ionization lines (McDowell et al. 1995). Blundell, Beasley, & Bicknell (2003) report the observation of a weak relativistically-beamed radio jet, and infer that the object is viewed face on. They then speculate that the low-equivalent width emission lines are a consequence of the face-on viewing angle, because they are diluted by the strong accretion disk emission. This reasoning has been recently applied to another weak-line quasar, HE 0141–3932 (Reimers et al. 2005).

While PHL 1811 may well be observed face-on, that cannot be the reason why the line equivalent widths are so low. First of all, one may not be able to achieve a very large boost in continuum emission by viewing an object face on. Laor & Netzer (1989) show that the ionizing flux from an accretion disk has nearly $\cos(\theta)$ dependence. Thus, assuming that the typical viewing angle to the accretion disk is $\sim 30^\circ$, then one gains only a factor of 1.15 by moving to a normal viewing angle. This is far from sufficient to explain the factor of ~ 5 difference between the equivalent widths of C IV in PHL 1811 and the quasar composite spectrum. Of course, this analysis assumes that the continuum is not relativistically beamed; there is no reason to expect that it is, because although it is a radio source, it is a very weak one, and it is not radio-loud.

Another argument against continuum boosting being responsible for the low high-ionization line equivalent widths is illustrated in Fig. 8. This figure shows that PHL 1811 has a continuum slope quite similar to that of an average quasar; simultaneously the H β line

has a normal equivalent width and the C IV has a very low equivalent width. The reasoning goes as follows. First, if the continuum were uniformly boosted, one would expect both lines to have low equivalent widths; yet we see that H β has a normal equivalent width, while the C IV equivalent width is low. Second, if the continuum were boosted preferentially in the blue (e.g., a super-Eddington disk may allow radiation to escape more easily along optically thin pores or channels (e.g., Begelman 2002) in the hotter regions of the disk), then one would expect a bluer continuum than the average quasar. Instead, we see that PHL 1811 has the continuum of a normal quasar, at least between C IV and H β .

We do not see any evidence for He II λ 1640. To estimate the upper limit of this line, we fit a C IV template shifted to the appropriate wavelength for He II. The best fit does not detect this line, so we estimate the upper limit by increasing the normalization until the χ^2 has increased by 6.63 compared with the best fit (99% confidence for one parameter of interest).

The 1400Å feature is difficult to analyze. First, the continuum slope appears to change at \sim 1470Å, although the continuum blueward of the 1400Å feature appears to be flat and to extrapolate to the continuum shortward of the Ly α feature. Second, the signal-to-noise ratio in that part of the spectrum is not very good. Finally, absorption lines from Galactic Al II λ 1670.79 and from C IV in the $z=0.08093$ damped Ly α system (Jenkins et al. 2003) cut through the middle of the feature. This feature is difficult to model, regardless, because it is usually a blend of the two multiplet lines of Si IV and the five multiplet lines of O IV]. Here, based on the lack of semforbidden lines in the rest of the spectrum, it might be safe to assume that the entire feature is Si IV. However, in Leighly (2004) it was inferred that O IV] participated in the wind in IRAS 13224–3809 and 1H 0707–495, and therefore was emitted in a different component than the intermediate-ionization lines such as C III] that are so clearly absent in PHL 1811. To emphasize the uncertainty in the identification of this feature, we refer to it as “unidentified” in Table 2. To estimate the flux and equivalent width, we fit the entire feature with a Gaussian. The centroid is measured to be 1395 Å, which possibly suggests an origin in Si IV, which has a gf weighted average wavelength of 1396.75 Å.

3.3.2. The Ly α /N V Region

The far-UV spectrum of PHL 1811 is cluttered with absorption lines that originate in intervening absorption systems (Jenkins et al. 2003). In order to better see the shape of the far UV spectrum, we model out the absorption lines first. Using Jenkins et al. (2003) as a guide, we fit local continua around each absorption line, and then model each absorption line

as a Gaussian. A comparison of the portion of the spectrum around Ly α with and without the absorption lines removed is seen in the top panel of Fig. 11.

The Ly α /N V feature in PHL 1811 appears as a lump stretching from ~ 1140 to $\sim 1270\text{\AA}$ superimposed on a rising continuum that appears to be linear or a power law in the range 1090 – 1140\AA and 1320 – 1360\AA . The equivalent width of the whole feature is only 24\AA , which is small compared with the 50 – 90\AA measurements of Ly α +N V from composite spectra mentioned above.

It is not obvious at first glance what the various bumps in the Ly α /N V feature are. There are peaks that could correspond to Si II multiplets near 1193 , 1260 and 1304\AA , and peaks that may be N V and Ly α . We apply the approach previously used by Leighly & Moore (2004), and fit these features using the C IV template profile described in §3.3.1. A difference in the analysis presented here is that we now use the IRAF `Specfit` program which can fit an input profile, and properly minimizes χ^2 to obtain the normalizations and spectral shifts.

We first determine the continuum by fitting the line-free bands 1086 – 1103 , 1116 – 1137 and 1314 – 1350\AA with a linear model. Initially, we assumed that the feature is composed of the five lines described above, and each one has the C IV template profile. We construct profiles for each multiplet, assuming first that the gas is optically thin and the multiplet ratios are proportional to the gf values, which were obtained from the NIST database⁴. Initially, we fix the wavelengths of the profiles at the rest wavelengths, this implicitly assuming that gas emitting all the lines has uniform kinematics. The resulting fit is shown in the middle panel of Fig. 11. Many of the bumps are modelled, but not well. Specifically, the N V emission appears to be insufficiently blueshifted, and there is extra emission blueward of Si II $\lambda 1193$. Emission in this region has been previously identified as C III* $\lambda 1175$ (e.g., Laor et al. 1997b), so we assume that as the tentative identification of this excess.

We also try profiles with all of the lines in the multiplets having equal strength, as would be appropriate if the gas were very optically thick. This model yielded a slightly larger χ^2 but was not clearly distinguishable from the optically-thin case. We therefore proceeded to use the optically-thin profiles.

We next apply the same model but add another template component around 1175\AA to model the suspected C III* emission, and allow the central wavelengths of the profile components for each line to be free in the fitting. We obtain a much better fit, as seen in the lower panel of Fig. 11. The wavelengths, fluxes and equivalent widths of this model are given

⁴http://physics.nist.gov/cgi-bin/AtData/main_asd

in Table 2. We find an excellent correspondence between the laboratory wavelength and the observed wavelength of the template fits of Si II $\lambda 1193$, Ly α and C III*; the remaining lines are somewhat blueshifted. The blueshift on Si II $\lambda 1308$ is conceivably partially due to an incomplete or faulty subtraction of a prominent absorption line. The blueshift on N V is plausibly real, as it might be expected that higher ionization lines may be emitted by gas with a higher velocity; this may be evidence that our template model is too simple.

The presence of C III* $\lambda 1175$ is interesting. This line is emitted as a transition to a metastable state that is the upper level for the C III] $\lambda 1909$ line. Laor et al. (1997b) discuss possible reasons for a strong C III* line in the prototype Narrow-line Seyfert 1 galaxy I Zw 1; we also tentatively identified this line in two other NLS1s (Leighly & Moore 2004). The presence of C III* suggests that there might be a similar transition from the metastable upper level of Si III] $\lambda 1892$ line, since Si $^{+2}$ and C $^{+2}$ are isoelectronic. That transition should appear in the region 1108.4–1113.2 \AA (the *gf*-weighted average wavelength is 1111.59 \AA). Indeed, there is a bump clearly present at these wavelengths that we confidently identify as Si III* $\lambda 1112$. Interestingly, it is not well fit by the template profile; we model it using first a single Gaussian, and then by the six components of the multiplet assuming optically thin ratios. For the second model, the width is $690 \pm 130 \text{ km s}^{-1}$ (Table 2), and it is marginally-significantly blueshifted by 290 km s^{-1} .

The successful deconvolution of the Ly α /N V lump into these six components using the C IV profile as a template may be fortuitous, and we caution that it is certainly not unique and may not be complete. The presence of the metastable transitions of C $^{+2}$ and Si $^{+2}$ led us to search for other similar metastable lines. On Fig. 1, we mark the positions of lines that have lower levels that are metastable, so that the transitions to ground state are semiforbidden, as described in §2. In the region of the Ly α /N V lump, there are a couple of Si II* transitions that could be strong. We also mark Si III $\lambda 1206.5$, a resonance line that may also contribute; this line is analogous to C III $\lambda 977$.

Strong high-excitation Si II has been previously reported by Baldwin et al. (1995). In §3.2.3, we obtained an upper limit on Si II $\lambda 1814$, and using the results of the deconvolution presented in this section, we measure a lower limit on the Si II $\lambda 1263$ /Si II $\lambda 1814$ of 8.5, even larger than the value of 6 that was obtained by Baldwin et al. (1995) from Q0207–398. Baldwin et al. (1995) showed that such high ratios are hard to explain, if the gas is collisionally excited, as one expects that the lower excitation line to be stronger. They suggested that the high-excitation transitions are selectively excited. The key seems to be that far UV lines are predominately excited by continuum pumping, generally speaking. Bottorff et al. (2000) explored the effect of microturbulence on line ratios in AGN, and showed that since pumped lines are enhanced by turbulence, large Si II $\lambda 1263$ /Si II $\lambda 1814$ ratios can be produced if

the turbulent velocity is high. Finally, Casebeer, Leighly & Baron (2006) investigated Si II emission as a function of the shape of the ionizing continuum in their Appendix. They note that high-excitation Si II emission is stronger for softer continua, and that the *Cloudy* output information indicates that for soft continua, continuum pumping is important.

In §3.3.1, we reported an upper limit on He II $\lambda 1640$, and comparing with N V measured from the deconvolution presented here, we obtain a lower limit on the N V/He II ratio of 11.6. Ferland et al. (1996) reported N V/He II > 10 for “Component B” (the outflowing component) in Q0207–398. N V and He II are both high-ionization lines from ions that require similar ionization potentials (He $^{+2}$: 54.4 eV; N $^{+4}$: 77.5 eV); therefore, they should be emitted by gas with similar properties. A thorough analysis carried out by Ferland et al. (1996) showed that the only way that the high N V/He II ratio can be produced is if the metallicity is enhanced by a factor of 5. A large N V/He II ratio in PHL 1811 may likewise imply a high metallicity also, although we again note the uncertainty in the deconvolution.

3.3.3. Other FUV lines

There are a few relatively narrow, weak lines in the FUV that we try to identify. We were able to identify N II $\lambda 1085$, which is a resonance line of N II. We model it with a single Gaussian, and also with the six Gaussians that comprise the multiplet. The latter fit yields a rather narrow line width, only 370 km s^{-1} . We also see another narrow line near 1034\AA , although this line is uncertain because considerable reconstruction had to be performed in the vicinity of this line. We were unable to confidently identify this line. It seems to be too centered and too narrow to be associated with O VI $\lambda 1032, 1038$.

C II $\lambda 1335$ is commonly seen in AGN, but we see no hint of it although it occurs in a relatively line-free region of the spectrum. To obtain an upper limit on the flux of this line, we add a C IV template component for this line to the FUV model, and fit over the entire region from $1086\text{--}1365\text{\AA}$; we also include a short strip of continuum between 1425 and 1462\AA . No significant emission is detected, so we estimate the upper limit on the flux of C II by increasing the normalization until the χ^2 is larger than the best fitting value by 6.63 (99% confidence for one parameter of interest).

4. Discussion

The spectra and analysis presented in §3 reveal the unusual emission-line properties of the narrow-line quasar PHL 1811. We briefly summarize the principal results here. PHL 1811

has no forbidden or semiforbidden lines, and unusual very low-ionization lines are present (e.g., Ca II and Na ID). He I $\lambda 5876$ is very weak, and a very low He I/H α ratio is inferred. The Fe II and Fe III pseudocontinuum dominates the near-UV part of the spectrum. However, while the Fe II in the majority of AGN is fit well by the template developed from the high signal-to-noise *HST* observation of I Zw 1, the pseudocontinuum in PHL 1811 has a demonstratively different shape that we show is likely to be a consequence of the presence of high-excitation Fe II and strong Fe III. Some of the other low-ionization lines are strong, including the high-excitation Si II lines near 1194Å and 1263Å, but other low-ionization permitted line emission (e.g., Mg II) is weak or absent (e.g., C II $\lambda 1335$). While the hydrogen Balmer lines appear to have rather typical equivalent widths, the equivalent widths of the high-ionization lines are small, and in addition, the high-ionization lines have a blue-shifted profile. Deconvolution of a feature near Ly α in terms of a template developed from the blueshifted C IV line reveals strong N V and high-excitation Si II, as well as C III* $\lambda 1176$.

The goal of this section is to interpret these results. But first, we summarize previous work that has addressed some of the results. We note that previous work has been mentioned throughout §3, but we summarize the major points here also. The production of Na ID has been discussed by Thompson (1991), who inferred that since the ionization potential of Na $^+$ is only 5.14 eV, this line must be produced very deep in the partially-ionized region where neutral sodium can survive. The production of Ca II has been discussed by Persson (1988); Ferland & Persson (1989) and Joly (1989). Observationally, the infrared triplet is correlated with the optical Fe II (Ferland & Persson 1989), but the Ca II H&K, the lines that we report here, are rarely seen (Ferland & Persson 1989). Both Ferland & Persson (1989) and Joly (1989) found that a high column density is necessary to produce the infrared triplet. Strong high-excitation Si II was first discussed by Baldwin et al. (1996), who pointed out the difficulty of producing large fluxes of the high-excitation lines such as Si II $\lambda 1263$, but at the same time producing very low fluxes of the resonance line Si II $\lambda 1814$. Bottorff et al. (2000) showed that this problem may be solved if the emitting gas is turbulent, as the high excitation Si II lines are predominately pumped by the continuum and will be selectively excited by turbulence. Blueshifted high-ionization lines have been observed in other NLS1s such as IRAS 13224–3809 and 1H 0707–495 (e.g., Leighly & Moore 2004). The C IV lines in these two objects also have relatively low equivalent widths, especially compared with the N V and the 1400Å feature. Leighly (2004) showed that the gas emitting these lines is optically thin to the continuum, and that the line ratios can be explained by a somewhat X-ray weak spectral energy distribution and elevated gas metallicity. We do not detect He II $\lambda 1640$ and thus infer a large N V/He II ratio. Ferland et al. (1996) discussed the large N V/He II ratio in Q0207–398, and found that the only way that this ratio can be explained is if the metallicity were enhanced compared with solar by $Z \sim 5Z_\odot$.

What is the origin of the unusual emission-line properties in PHL 1811? PHL 1811 has one property that is much different than an ordinary quasar: it is intrinsically X-ray weak (Paper I), and therefore has an unusually soft spectral energy distribution. In the next several subsections, we examine the physics of gas illuminated by a very soft spectral energy distribution. We find that gas illuminated by a very soft SED has much different physical properties than gas illuminated by a typical AGN SED, and that most of the unusual observational features of PHL 1811 can be explained qualitatively by the soft SED *alone*. The low He II/H α ratio cannot be explained by the soft SED, but we find that it can be explained by a “filtered” continuum; we discuss this idea in §4.4. Finally, in §4.5 we discuss whether there may be other objects like PHL 1811, and how we might identify them.

4.1. Physical Conditions in Gas Illuminated by a Soft SED

In this section, we investigate the physical conditions and line emission from gas illuminated by an X-ray weak spectral energy distribution. Our goal is physical insight rather than a detailed match to the line emission, so we begin by exploring the physics of gas illuminated by a range of spectral energy distributions for a representative value of the ionization parameter ($\log U = -1.5$) and density ($\log n = 11$). These correspond to a photoionizing flux of $\log \Phi = 20$. We use a hydrogen column density of $\log(N_H) = 24.5$, which corresponds to a thickness more than 100 times the depth of the hydrogen ionization front. We now define some terms. We refer to the region between the illuminated surface of the gas and the hydrogen ionization front as the H II region, and the region at greater depths than the hydrogen ionization front as the partially-ionized zone. In addition, we discuss the ionization potential to create emitting ions, and we refer to this as “ionization potential”, whereas more correctly, it is the ionization potential of the next lower charge state.

4.1.1. The Continua

We use a range of continua to explore the influence of the spectral energy distribution. We start with the ones previously presented in Casebeer, Leighly & Baron (2006) (hereafter referred to as the CLB continua). They are described in detail in the Appendix of that paper; briefly, they constructed a number of spectral energy distributions parameterized by the energy in eV of the UV bump high-energy cutoff. They assumed that the temperature of the cutoff T_{cut} , which corresponds roughly to the inner edge of the accretion disk, is related to the luminosity by $L \propto T_{cut}^{-4}$. Then, to determine the X-ray power law normalization, they assumed that the UV monochromatic luminosity at 2500Å is related to

the X-ray monochromatic luminosity at 2 keV by α_{ox} , with α_{ox} dependence on UV luminosity given by the regression developed by Wilkes et al. (1994). Finally, the proportionality constants were determined using the measured T_{cut} from coordinated *IUE* and *ROSAT* observations of the quasar 3C 273 (Walter et al. 1994). For more details, see the Appendix of Casebeer, Leighly & Baron (2006).

We also use the PHL 1811 SED developed from the *HST* and the brighter of the two *Chandra* observations, supplemented by a *FUSE* point from a non-simultaneous observation, and using the *Cloudy* AGN continuum at higher and lower energies where we have less information (Fig. 12). We do not know the shape of the extreme UV, so we simply join the *FUSE* point and the *Chandra* spectrum using a power law. We also use the *Cloudy* AGN continuum with parameters as used by Korista et al. (1997); hereafter referred to as “K97”, and also shown in Fig. 12, this is taken to be a typical AGN continuum.

Fig. 13 gives some information about the properties of these continua. The CLB continua are coded on the x-axis by their cutoff temperature, and the other two files are named “PHL1811”, and “K97” for the PHL 1811 and Korista et al. continua, respectively. The top panel shows the α_{ox} for the continua. As noted in Paper I, PHL 1811 is anomalously X-ray weak and has a very steep $\alpha_{ox} = -2.3 \pm 0.1$. In comparison, the α_{ox} for the K97 spectrum is -1.4 .

In the next panel, we plot the continuum flux at 2500Å assuming typical values of the input ionization parameter ($\log U = -1.5$) and density ($\log n = 11$). These values correspond of course to the same value of the ionizing photon flux, but the continuum flux in the optical or UV is much different. Specifically, an X-ray weak continuum must be brighter in the optical and UV in order to produce the same ionizing flux, since the ionizing flux is integrated from 13.6 eV toward shorter wavelengths. This will influence the equivalent widths of the lines produced; specifically, for objects that have soft continua like PHL 1811, the lines will appear to have lower equivalent width for the same global covering factor compared with an ordinary AGN continuum. The PHL 1811 continuum is 3.5 times brighter than the K97 continuum at 2500Å. This is certainly one factor contributing to the low equivalent widths of the line emission observed in PHL 1811.

In the bottom panel of Fig. 13, we show the Compton temperature, which is a measure of the mean photon energy of the continuum. The gas would reach the Compton temperature if it were in equilibrium with the radiation field. The Compton temperature is very low for the PHL 1811 continuum, around 5×10^4 K; this temperature is similar to the typical temperature of a photoionized gas.

4.1.2. Temperature and Hydrogen Ionization

We first examine the temperature structure of the ionized gas (Fig. 14). The drop in temperature at around $1-2 \times 10^{11}$ cm occurs at the hydrogen ionization front; the kink at shallower depths occurs at the helium (He^{+2} to He^+) ionization front. As might be expected, the very soft continuum from PHL 1811, and accompanying low Compton temperature, produce a rather cool temperature in the photoionized gas. The temperature in the partially-ionized zone for the PHL 1811 is exceptionally low; we will return to this point later. In contrast, the harder continua produce significantly higher temperatures, especially in the H II region.

Next, we examine the fraction of ionized hydrogen as a function of depth (Fig. 15). The hydrogen ionization front is slightly deeper for the harder SEDs, perhaps marking additional ionization associated with the presence of soft X-rays, higher Compton temperature and greater heating. The fraction of ionized hydrogen in the partially ionized zone follows the temperature for the harder SEDs; that is, at a particular depth, the ionization fraction is higher for harder SEDs. That breaks down at the softest SEDs, where the ionization fraction rises again. For the PHL 1811 continuum, the ionization fraction is higher than for many of the harder SEDs.

To understand the origin of the high ionization fraction in the partially-ionized zone of the gas illuminated by the PHL 1811 continua, we review the physical mechanisms that produce ionized hydrogen in the partially-ionized zone. There are two principal mechanisms (e.g., Collin-Souffrin & Dumont 1989; Ferland 1999). The first mechanism involves X-ray photons that photoionize heavy elements through inner shell interactions creating secondary nonthermal electrons that ionize hydrogen. These electrons also heat the gas. The second mechanism involves photoionization of hydrogen in excited states (e.g., $n = 2$) by the direct continuum and the diffuse continuum. The hydrogen is in an excited state due to a circular process. Recombining hydrogen produces $\text{Ly}\alpha$; the optical depth to $\text{Ly}\alpha$ in the partially-ionized zone is very high, so the $\text{Ly}\alpha$ photons scatter many times before escaping the gas. That scattering may leave some hydrogen atoms in $n = 2$ long enough that they can be photoionized by the Balmer continuum of the incident quasar continuum.

To investigate the importance of the latter process as a function of spectral energy distribution, we examine the rate of photoionization from $n = 2$ per hydrogen atom in $n = 2$ by solving the radiation transport equation at any depth in the gas. We compute the photoionization rate from the incident continuum, attenuated by $e^{-\tau_\nu}$, where τ_ν can be obtained using the extinction coefficient which can be output from *Cloudy*. We also compute the photoionization rate from the diffuse continuum, where the diffuse continuum I_ν is obtained by integrating the source function; this can also be output from *Cloudy*. The

resulting rates are shown in Fig. 16. For comparison, we show the collisional ionization rate.

Fig. 16 shows first that collisional ionization is practically negligible in the partially ionized zone. This is not surprising, since the temperature of the gas is a fraction of an eV. Of the photoionization rates, the contribution from the direct continuum is more important than that from the diffuse continuum, but the diffuse continuum contributes most to the harder continua, from, e.g., $\sim 15\%$ for the K97 continuum to $\sim 40\text{--}60\%$ in the very hardest continua. Considering the contribution from the direct continua alone, we see that the photoionization rate from $n = 2$ is highest for the softest continua. This is simply a consequence of the fact that for a particular ionizing flux, the flux density in the optical and UV will be higher for the soft continua (Fig. 13; §4.1.1). By itself, this predicts that the softest continua would produce the highest ionization fractions in the partially ionized zone. This is not what we see, so the difference must lie in the number of hydrogen in $n = 2$.

The density of hydrogen in $n = 2$ can be output from *Cloudy* also, and we show it in left panel of Fig. 17. We see indeed that in the partially-ionized zone, this density is higher in objects with the hardest SEDs. However, this difference is insufficient to explain the dependence of the hydrogen ionization on the SED. For example, at a depth of 5×10^{11} cm, the hydrogen fraction in gas illuminated by the PHL 1811 continuum is almost the same as in gas illuminated by the $kT = 320$ eV SED. At that depth, the total photoionization rate is a factor of five larger for PHL 1811, but the density of hydrogen in $n = 2$ is only a factor of 1.5 larger for the $kT = 320$ eV SED. Thus, the balance of hydrogen ionizations in gas illuminated by the hardest continua come from the first process mentioned above, the initial inner-shell X-ray photoionization and resulting photoelectrons.

Next, we investigate the origin of the hydrogen in $n = 2$. We plot the ratio of the excitation temperature based on the populations in $n = 1$ and $n = 2$ to the electron temperature (Fig. 17). The ratio exceeds 1 in the partially-ionized zone, except for the gas illuminated by the hardest continua, which means that the temperature is not sufficiently high to explain the population in $n = 2$. Therefore, the radiation field must be responsible, and indeed, scattering of trapped Ly α mentioned above is likely to be the origin of hydrogen in $n = 2$ in gas illuminated by the PHL 1811 continuum.

The surprising aspect of Fig. 17 is that the gas illuminated by the PHL 1811 continuum exhibits a very large ratio, indicating an exceptionally high ratio of hydrogen in $n = 2$ compared with that expected from a thermal gas. This trend continues to even higher n ; in Fig. 18 we show the ratio of the density of hydrogen in $n = 5$ from the *Cloudy* output to the ratio expected based on the density in $n = 1$ and the electron temperature; this parameter is proportional to the departure coefficient for $n = 5$. This shows that departure coefficient is higher in gas illuminated by the PHL 1811 continuum by nearly three orders of magnitude

compared with gas illuminated by the hardest continua.

The origin of the excited-state hydrogen in PHL 1811 is the strong diffuse continuum. In Fig. 19 we show the integrated diffuse continuum (i.e., energy in the diffuse continuum) multiplied by the depth, as a function of depth. The energy in the diffuse continuum is much larger for gas illuminated by the PHL 1811 continuum. Note that this does not necessarily mean that we expect to see a strong continuum emission from this object, as the diffuse continuum used in this calculation is the emission at that depth, and the radiative transfer to the surface has not been folded in. This fact also explains the low electron temperature in the partially-ionized zone; the energy is locked up in the radiation field and excited states of hydrogen rather than electron kinetic energy. Thus, in PHL 1811, this strong continuum scatters in the partially-ionized zone, causing the hydrogen to be in high-excitation states. We will see why the continuum is so strong in the next section.

To summarize this section, we find that the hydrogen in the partially-ionized zone in gas illuminated by the PHL 1811 continuum is rather highly ionized. This is a consequence of the bright Balmer continuum for a given photoionizing flux for soft SEDs, and the relatively large density of hydrogen in $n = 2$, which is a consequence of strong diffuse continuum. As will be shown in the next section, the low temperature means that the gas cannot cool by emission of collisionally-excited lines, so the energy is deposited in strong continuum and excited states of hydrogen, resulting in the relatively low gas temperature.

4.1.3. Metal Ions: General Considerations

The conditions in the line emitting gas can be understood further by examining the behavior of the metal ions. In Fig. 20 we show the ratios of the column densities of the ions of interest for the PHL 1811 continuum to the K97 continuum as a function of the ionization potential to create each ion. These ratios show that for ionization potentials less than ~ 10 eV, the column densities are approximately the same; the high point is Ca^+ , in which the column is a factor of 2.3 times greater in PHL 1811. For ionization potentials greater than 20 eV, the column densities are considerably lower in the gas illuminated by the PHL 1811 continuum. This is not surprising because the PHL 1811 continuum lacks high energy photons required to create these ions. For ionization potentials between 10 and 20 eV, the columns in PHL 1811 are higher than in K97. This also makes sense because these are the ions that occupy the H II region, instead of the high-ionization species that are usually there.

One might expect that if the column density of an ion is larger, the line emission from

that ion must also be larger. Fig. 20 shows the ratios of predicted emission-line strengths from gas illuminated by the PHL 1811 continuum compared to those from gas illuminated by the K97 continuum. The ratio is smaller for the high-ionization lines, as might be expected; those ions are few in the gas illuminated by the PHL 1811 continuum, so the high-ionization line emission is weak. However, for the low-ionization lines, the situation is much different, and in fact lines from the same ion exhibit different ratios. Some lines are stronger in PHL 1811; for example, Si II $\lambda 1194$ is predicted to be 3.3 times larger for PHL 1811. Other lines from the same ion are weaker in PHL 1811; for example, Si II $\lambda 1814$ is predicted to be 1.7 times weaker. This difference is a result of the different excitation mechanisms for the lines. Mg II $\lambda 2800$ and Si II $\lambda 1814$ are transitions from the lowest permitted levels; they are collisionally excited and their emission strengths depend on the temperature of the gas. Since the temperature is lower in gas illuminated by the PHL 1811 continuum, the emission from these lines is weaker. In fact, it can be shown that the ratios of the emission rates produced by the PHL 1811 continuum and the K97 continuum as a function of depth correspond fairly closely to the ratios one would expect based on the difference in temperatures through the Boltzmann excitation equation. This is demonstrated by the close correspondence between the solid grey line and the dashed grey line for Si II $\lambda 1814$ in Fig. 21 for large depths where Si^+ dominates. In contrast, high-excitation Si II, such as Si II $\lambda 1194$, is predominately excited by pumping by the continuum. As noted in §4.1.1, the UV continuum will be relatively strong in PHL 1811 for the same ionization parameter and therefore, lines that are excited by continuum pumping can be expected to be relatively strong. This is demonstrated by the great discrepancy in the ratio based on the *Cloudy* emissivity output (solid black line) and the ratio based on the Boltzmann equation (dashed black line) in Fig. 21.

Fig. 20 shows that several bands of Fe II behave differently for the PHL 1811 continuum compared with the K97 continuum. We discuss the Fe II further in §4.4. In addition, we find that the Fe^{+2} ion column is elevated in PHL 1811, similar to the other intermediate-ionization line columns, suggesting that Fe III should be strong. We cannot check this suggestion, however, because *Cloudy* does not model UV Fe III lines, such as Fe III UV 34, near 1900Å, or Fe III UV 68, near 1950Å.

It is important to note that common UV semiforbidden lines (C III] $\lambda 1909$, Si III] $\lambda 1892$, N III] $\lambda 1750$, C II] $\lambda 2325$, N II] $\lambda 2141$) are suppressed for the PHL 1811 continuum. This is a consequence of two factors. For the twice-ionized ions, with the exception of Si^{+2} , the column of the ion is lower in PHL 1811. In addition, these lines are all collisionally excited, arising from ions that have two electrons in their P-shell. Thus, since the gas temperature is lower in PHL 1811, these lines are weaker. This result has a consequence for plasma diagnostics. Semiforbidden lines are generally used as density indicators, since they have critical densities

in the range thought typical of broad-line region gas (e.g., for the lines above, the critical densities range from $3.16 \times 10^9 \text{ cm}^{-3}$ for C II $\lambda 2325$ to $3.12 \times 10^{11} \text{ cm}^{-3}$ for Si III $\lambda 1892$; Hamann et al. 2002). This means that the absence of these lines in objects with very soft continua like PHL 1811 does not require the presence of high-density gas.

4.1.4. Exploring the $\log U$, $\log n$ Parameter Space

The discussion above considers only a single ionization parameter and density; next we examine the properties of the gas as a function of these two parameters. We perform simulations for the PHL 1811 continuum and for the K97 continuum for ionization parameter $-3.5 \leq \log U \leq 0.5$ and for density $8.5 \leq \log n \leq 12.5$. In each case we adjust the column density so that $\log N_H - \log U = 26$; this ensures that the gas is very optically thick to the continuum, and probes approximately the same thickness relative to the hydrogen ionization front.

We first examine the column density of various ions as a function of ionization parameter and density. Since the total column density of the gas varies with ionization parameter, we look at the column density relative to the total column; this is equivalent to $\log(N_{ion}) - \log U$. Generally speaking, the behavior of the ionic column density for low and intermediate ionization metal ions relative to the total column density was divided into two groups according to ionization potential. For the singly-ionized ions C⁺ and N⁺, the relative column was principally density independent, and decreased as ionization parameter increased, as the ionization state of the gas shifted to a higher ionization state. O⁺ looked like H⁺, most probably because the strong influence of the Bowen effect. In contrast, the ions Mg⁺, Al⁺, Si⁺ and Fe⁺, were almost independent of ionization parameter and density. In both cases, the ionic structure was nearly the same for the PHL 1811 continuum and the K97 continuum; this is not surprising because they should both be roughly equally efficient in producing low-ionization ions.

For the twice-ionized ions, there are significant differences between the gas illuminated by the PHL 1811 continuum and the K97 continuum. First, there were differences in the total column densities. For the doubly-ionized ions with higher ionization potential (C⁺², N⁺², and O⁺²), the columns were higher for the K97 continuum. In contrast, for the doubly-ionized ions with lower ionization potential (Al⁺², Si⁺², and Fe⁺²), the columns were higher for the PHL 1811 continuum. This makes sense, and it is something that we noted previously in CLB: for softer continua, the cooling in the region of intermediate ionization shifts to ions that have lower ionization potential. For these ions, the dependence on ionization parameter and density were similar: there is an ionization parameter at which the column is maximized,

and at that ionization parameter, the column decreases as a function of density. This happens because at higher densities, recombination is stronger, and the overall ionization state of the gas is a little lower. At lower densities for the same ionization parameter, the ionization shifted to the next higher state. But for the higher-ionization doubly-ionized ions, that structure was apparent only for the K97 continuum; for the PHL 1811 continuum the column increases with ionization parameter almost independent of density.

More highly ionized ions (C^{+3} , N^{+4} , He^{+2}) were significantly deficient over the entire parameter space for the PHL 1811 continuum, as expected. However, these ions were present at highest ionization parameters.

We next look at equivalent widths of lines that are common in AGN. Note that by discussing the equivalent width rather than the line flux, we account for the fact that the optical and UV continuum against which the lines are measured is brighter by a factor of ~ 3.5 in PHL 1811 for the same ionizing flux. We first looked at lines that had equivalent widths using the PHL 1811 continuum that were predicted to be larger than or comparable to those obtained using the K97 continuum, both at our fiducial point ($\log U = -1.5$ and $\log n = 11$), and over the parameter space. The strongest lines were the UV Fe II and the high-ionization Si II. These are both among the strongest lines in the observed spectrum, a fact that suggests that we are on the right track. But not all low-ionization lines were strong in PHL 1811; notably weak ones were Mg II and Si II $\lambda 1814$. The difference again is the excitation mechanism: the high-excitation silicon and iron lines are pumped by the continuum, while the magnesium and low-excitation silicon are collisionally-excited. In addition, as expected, the high ionization lines such as C IV were among the weakest in PHL 1811 compared with K97 continuum. We illustrate this in Fig. 22. At the fiducial point, the equivalent width of C IV is a factor of more than 100 times lower for the PHL 1811 continuum compared with the K97 continuum.

The soft continuum also affects the semiforbidden lines in interesting ways. Fig. 23 shows the equivalent width contours of Si III] $\lambda 1892$ for the PHL 1811 continuum and the K97 continuum. This emission line has a critical density of $3 \times 10^{11} \text{ cm}^{-3}$, so the decline toward higher density at about this value for the K97 continuum is expected. But the PHL 1811 continuum simulations show a different behavior; the line begins to decrease at much lower densities, around 10^{10} cm^{-3} . Again, this means that the usual density indicators fail for soft continua, and the absence of semiforbidden lines does not require the presence of high-density gas.

The weakness of the collisionally-excited metal lines in PHL 1811 has important consequences for the physical conditions in the gas. If the gas cannot cool by emission of collisionally-excited lines, and yet there are plenty of photoionizing photons, the energy goes

into the production of hydrogen and other continua. This is what we see in PHL 1811. The situation is very similar to high-density gas (discussed by, e.g., Rees, Netzer & Ferland 1989). At high density, collisional deexcitation of metal ions prevents the gas from cooling by collisional-excitation of metal ions, and the high-density gas also becomes dominated by continua. In a sense, both types of gas are “cooling challenged”. They also have similar observational properties, in particular, the weakness of the semiforbidden lines.

To summarize this section, we find that properties of metal ions and their emission in gas illuminated by the soft PHL 1811 continuum is different from gas illuminated by the K97 continuum in the following ways. The column densities and line emission from high-ionization ions are lower in gas illuminated by the soft SED. The column density of the intermediate-ionization ions is larger, but the emission from those ions is lower if the line is collisionally dominated, or higher, if the line is pumped by the continuum. Thus, the strongest lines should be Fe II and high-excitation Si II, as observed, while high-ionization lines and semiforbidden lines are weak. As a consequence, semiforbidden lines are not good density diagnostics in gas illuminated by the soft SED. Line emission from gas illuminated by a soft SED has many similarities with high-density gas, and in principle may be mistaken for high-density gas, as a consequence of inefficient cooling by line emission in both cases.

4.2. A Locally Optimally-emitting Cloud Model

In the previous section, we showed that the soft SED from PHL 1811 results in low emission line flux and low equivalent widths compared to the more typical SED used by K97. We first showed this for the fiducial parameters ($\log U = -1.5$, $\log n = 11$, $\log N_H = 24.5$) and then for a range of ionization parameters and densities, with the column density adjusted so that $\log N_H + \log U = 26$. As a final investigation into this point, we compute a Locally Optimally-emitting Cloud (LOC) model, to ensure that our result is robust against averaging.

The LOC model was first presented by Baldwin et al. (1995). Motivated by the fact that it is unrealistic to expect that the net emission from the broad-line region could be from gas characterized by a single ionization parameter, density, and column density, they postulated that the observed emission should be an average of emission from gas characterized by a range of properties. In the standard LOC model, the radial distribution (equivalent to photoionizing flux) and density distribution of the line-emitting gas are characterized by power laws, with the radial and density indices equal to -1 , and the column density set equal to 10^{23} cm^{-3} . These parameters are rather arbitrary, but they seem to give relatively good fits to most quasars, at least for the high-ionization lines. For example, Casebeer, Leighly & Baron (2006) computed an LOC model for RE 1034+39, an object known for its hard SED, and

found that the ratio of the prominent lines with Ly α matched the observed ones well; the exceptions were C IV and Mg II, which were both predicted to be brighter with respect to Ly α than observed.

To compute the LOC model, we run *Cloudy* models for the following parameters: photon flux $17 < \log \Phi < 24$, with $\Delta\Phi = 0.125$; density $7 < \log n < 14$ with $\Delta n = 0.125$; column density $N_H = 10^{23} \text{ cm}^{-3}$ uniformly. This is the range of parameters computed by Korista et al. (1997), and extends the range originally used by Baldwin et al. (1995) and Casebeer, Leighly & Baron (2006) to higher photon fluxes and lower densities. We compute the LOC assuming the power law indices of -1 for the radial and density distributions; again, these are the standard choices. The outputs of the LOC program are the ratios of the line fluxes to the continuum at 1215\AA . We use the input continua to convert these values to equivalent widths. We choose a covering fraction of 0.25 because that seems to give values for the K97 continuum that correspond relatively well with equivalent widths of generally bright lines from composite spectra compiled by Francis et al. (1991) (LBQS quasars), Zheng et al. (1997) (*HST*), Brotherton et al. (2001) (*FIRST* survey), and Vanden Berk et al. (2001) (SDSS quasars). The results are given in Table 3.

Examination of the table shows that the LOC model for the K97 continuum gives a reasonable match to composite spectra equivalent widths overall, within a factor of two for most of the lines. For example, it predicts a C IV equivalent width of 47\AA , while the four composite spectra yield measured values of C IV of 37, 59, 33, and 24\AA . This good correspondence is expected, since the K97 continuum is intended to be representative of the continuum of an average AGN, and the LOC model was developed originally to explain the emission lines of composite spectra.

The equivalent widths of the lines observed in PHL 1811 are much smaller than observed in the composite spectra. For example, the observed equivalent width of C IV in PHL 1811 is only 6.6\AA , while the composite spectra yield 37, 59, 33, and 24\AA . Correspondingly, the LOC model for the PHL 1811 continuum yields consistently much smaller equivalent widths for all lines, in some cases by large factors. For example, the equivalent width of C IV for the PHL 1811 LOC model is 0.9\AA , compared with 47\AA for the K97 LOC model. In fact, the PHL 1811 LOC equivalent widths are generally smaller than the observed equivalent widths by large factors; the exception is Mg II in which the PHL 1811 LOC model gives an equivalent width of 15\AA , while the observed equivalent width is 13\AA . The largest discrepancies are Ly α and N V. This may be evidence for a separate optically-thin component that is not well described by the standard LOC parameters. We note that difficulties in using the standard LOC distributions have been reported for SDSS J154651.75+525313.1, an object that also has strong low-ionization lines (Dhanda et al. 2007).

Despite disagreement between the detailed predictions of the LOC models and the data, we have shown that the equivalent widths of the lines in gas illuminated by the PHL 1811 continuum remain low even when we average over a large range of ionization parameters and densities. In the spirit of the locally optimally emitting cloud concept, we note that the extremely soft continuum of PHL 1811 allows almost no cloud to emit lines very optimally, since gas illuminated by the soft SED has trouble producing line emission. However, even though the continuum may be relatively strong in the gas illuminated by the PHL 1811 continuum (as discussed in §4.1.2), we do not expect to see strong continuum emission. The ratio of the Balmer continuum flux to the continuum at 3645Å (for the 0.25 covering fraction) is 310Å for the K97 continuum, but only 94Å for the PHL 1811.

4.3. Fe II and Fe III Emission

In §3.2.1 we showed that the I Zw 1 Fe II template does not describe the Fe II and Fe III pseudocontinuum in PHL 1811. Thus, it is clear that understanding the Fe II and Fe III spectrum of PHL 1811 is important for understanding the physics of the line-emitting gas. However, the tools that we can use are limited. First of all, *Cloudy* does not include any near-UV Fe III lines. Second, the Fe^+ ion in *Cloudy* has only 371 levels and the highest one has an energy of just 11.6 eV; in §3.2.1 we discussed why we believe that significant emission arises from the levels between 13 and 14 eV. In addition, *Cloudy* uses an approximation for the radiative transfer; this might be expected to be a serious model weakness especially for the emission from the partially-ionized zone where radiative transfer can influence the thermal equilibrium. Furthermore, it has been shown that this Fe II model does not explain the spectra of AGN well at all (e.g., Baldwin et al. 2004). These are clearly serious inadequacies for understanding the Fe II and Fe III in this object; nevertheless, we can learn some very useful things using the *Cloudy* Fe II model.

We start with our baseline parameters ($\log U = -1.5$, $\log n = 11$, and $\log N_H = 24.5$), and run *Cloudy* models for the range of spectral energy distributions discussed in §4.1.1. We first examine the Fe II flux in each of several bands: 1000–2000Å (far UV), 2000–3000Å (UV), 4000–6000Å (optical), and 7800Å–3 microns (infrared). As can be seen in Fig. 24, in each of these bands, the flux from the gas illuminated by the PHL 1811 is second-greatest, following and comparable to gas illuminated by the $kT = 10$ eV continuum. In order to conveniently plot all the results in one panel, we show the ratio of the results with respect to the one from PHL 1811. The Fe II flux varies with SED differently in the different bands. In the far-UV band, the flux decreases smoothly as the SED becomes harder. For the other three bands, the flux first decreases as the flux becomes harder, but then recovers for hardest SEDs. This

effect is most pronounced for the optical band, in which the flux for the $kT = 320$ eV SED is almost the same as that from the PHL 1811 SED.

As discussed in §3.2.1 and in previous papers (e.g., Dietrich et al. 2002), the Fe II/Mg II ratio is used as an abundance diagnostic in quasars, although as discussed in Leighly & Moore (2006), an observed range in this ratio over a limited range in redshift observed in SDSS quasars makes this usage somewhat questionable without a better understanding of Fe II excitation. In the second panel of Fig. 24 we show the ratio of the Fe II model emission between 2200 and 3050Å to Mg II. This ratio is rather constant for harder SEDs, but is very high for PHL 1811, a factor of 5.2 higher than that from K97. This very high ratio is a consequence of both the higher flux in Fe II (a factor of 2.1 higher in PHL 1811 compared with K97) and a lower flux in Mg II (a factor of 2.4 lower in PHL 1811). We have already discussed in §4.1.3 the fact that Mg II is a collisionally-excited line and is thus suppressed in PHL 1811 because of the low electron temperature.

As noted in §3.2.1, PHL 1811 does not have a particularly high ratio of optical Fe II to H β compared with a previously-analyzed sample of NLS1s; the optical Fe II emission is not as spectacularly prominent in PHL 1811 as it is in some AGN. Indeed, the model predicts only a factor of 1.7 higher flux in the optical band in PHL 1811 compared with K97, in contrast to the factor of 2.2 higher flux in the UV band. Thus, the observed relatively high UV-to-optical flux ratio is qualitatively predicted.

Baldwin et al. (2004) discuss the properties of the 371-level Fe II atom currently implemented in *Cloudy*. The model does not fit the observed spectra from AGN at all well in the near UV. Specifically, strong emission from resonance lines and low-lying levels near 2400Å and 2600Å are predicted to produce strong “spikes” that are not seen in AGN spectra. Baldwin et al. (2004) parameterize this problem using a “spike/gap” flux ratio parameter. The parameter is defined as the flux in the 2312–2328 and 2565–2665Å bands (the spikes) divided by the flux in the 2462–2530Å band (the region between the spikes). Baldwin et al. (2004) note that the observed ratio is typically near 0.7 in AGN. We plot the spike/gap parameter in the bottom panel of Fig. 24. We find that this parameter is minimized for the PHL 1811 continuum, so although it is still much larger than observed, the trend is in the right direction.

We can understand these results using the supplemental output from *Cloudy* which includes the departure coefficients and populations of a few selected levels as a function of depth, the column density of the 371 levels, and the emissivity of various spectral bins as a function of depth. The departure coefficients show that the level populations are consistent with those predicted by the gas temperature for upper levels less ~ 7 eV. Referring to the diagram shown in Fig. 6, these are the upper levels of the resonance lines and low-lying

transitions. For higher levels, the departure coefficient for PHL 1811 is consistently higher than those from the harder SEDs, and can be very large in the partially-ionized zone. Fig. 25 shows one of the more extreme cases. High levels are apparently being selectively excited in PHL 1811, and since we see an inverse dependence with the hardness of the SED, it is most probable that the incident SED is responsible for the pumping.

The departure coefficients are high in gas illuminated by the PHL 1811 continuum, but the temperature in the partially-ionized zone is low, so we need to also examine the populations in the levels as well. For levels with energies less than ~ 7 eV, the populations in PHL 1811 were lowest, and the populations increased as the SED became harder. This is expected from the departure coefficient behavior, as the temperature in the partially-ionized zone is highest for the hardest SEDs. But for higher levels, the populations reverse, finally becoming much larger for PHL 1811 than for the other SEDs. An extreme example is seen in Fig. 25. Thus the departure coefficient is high for PHL 1811 both because the temperature is low, and because the density of highly-excited ions is high.

Examination of the populations and departure coefficient shown in Fig. 25 reveals another important feature of gas illuminated with the PHL 1811 continuum. As will be discussed in §4.4, the transition from He^+ to neutral He coincides with the hydrogen ionization front in gas illuminated by a typical AGN continuum. At the same time, Fe^+ is almost exclusively found in the partially-ionized zone. However, for soft continua, the He^+ to neutral He transition occurs at a shallower depth than the hydrogen ionization front. Thus, there exists a region in which hydrogen is fully ionized and He is neutral. Fe^+ is present in this region where hydrogen is fully ionized. This is the origin of the shelf between 8×10^{10} and 1×10^{11} cm seen in Fig. 25. These Fe^+ can contribute significantly to the emission. While this is not a very extensive region compared with the whole partially-ionized zone, it is worth remembering that the UV Fe II is highly trapped, and the bulk of the emission comes from the vicinity of the hydrogen-ionization front. The density of Fe^+ in the H^+ –neutral He zone is small, and thus they may be less trapped. Examination of the emissivity times depth confirms that a substantial fraction of the emission comes from this region (Fig. 26).

We are now in the position to understand the results shown in Fig. 24. High-energy lines in the far UV are purely pumped; thus they are strongest for the PHL 1811 continuum and other soft SEDs, and are weakest for the hardest SEDs. The UV lines have contributions from pumping in the higher-energy transitions, and contributions from collisional excitation for the resonance and low-lying transitions. Thus, they are strong for the soft SEDs, where pumping dominates, and strong for the hardest SEDs that produce the highest temperatures, allowing collisional excitation to become equally important. Optical emission comes from transitions from the UV levels near 5 eV down to the metastable levels near 3 eV; these

low-lying levels are predominately collisionally excited. Recall that the optical emission is not trapped like the UV emission, so the hotter partially-ionized zone produced by gas illuminated by the hard SED produces plenty of optical Fe II. Finally, the infrared emission is produced by Ly α pumping; it is thus approximately proportional to the diffuse continuum, which is shown in §4.1.2 to be strongest for the soft SEDs, becoming weaker for intermediate SEDs, and finally increasing again for the hardest SEDs.

Overall, the strong UV Fe II emission seems to come from continuum and Ly α pumping and a significant column of Fe $^+$ in the H $^+$ –neutral He zone. All levels of the 371-level atom are more highly populated in the gas illuminated by the PHL 1811 SED. At the same time, because of the lower temperature, collisional excitation is less important, producing less optical emission relative to UV in the partially-ionized zone. Mg II is also weak, as discussed in §4.1.3, and therefore the observed relatively high UV Fe II/Mg II and UV/optical ratios are explained. Finally, the “Spike/Gap” result is explained. The spikes are predominately collisionally excited, and are thus very strong for the hardest SEDs, while the gap is predominately emission from high levels, and are thus stronger for the softer SEDs. Thus the softer SEDs produce a lower “Spike/Gap” ratio, although for the fiducial choice of parameters is it still much larger than typically observed in AGN.

So far we have only examined the Fe II and Fe III emission for a single value of the ionization parameter and density. Next, we investigate the effect of varying the ionization parameter and density. As was done in §4.1.3, we compute the *Cloudy* models for the PHL 1811 continuum and the K97 continuum for $-3.5 < \log U < 0.5$, and $8.5 < \log n < 12.5$. The column density was adjusted so that $\log N_H + \log U = 26$. First, as we noted above, *Cloudy* does not output any Fe III lines; however, we find that the column density of Fe $^{+2}$ ions is consistently larger in the gas illuminated by the PHL 1811 continuum by a factor of ~ 2.5 , with the largest column densities produced at the highest densities and $\log U = -0.5$. This is evidence that the Fe III flux should be greater from gas illuminated by the PHL 1811 continuum.

We next examine the dependence of the Fe II properties considered in Fig. 24 as a function of ionization parameter and density for gas illuminated by the PHL 1811 and the K97 continua. For the Fe II flux, we see the same trends as seen in Fig. 24: the flux is uniformly larger for the gas illuminated by the PHL 1811 continuum. The largest PHL 1811/K97 flux ratio is seen in the FUV band, ranging from ~ 1 to 4.2 with a mean of 2.9, with the largest ratios observed at the highest ionization parameter and density. The same pattern is seen in the UV band, ranging from ~ 1 to 2.6, again with the largest values seen at highest ionization parameters and densities. The optical flux ratio ranges from ~ 1 to 1.65, with a mean of 1.3, and the IR flux ratio ranges from ~ 1 to 2.7 with a mean of

1.8. The maximum ratios for the optical and IR ratios occurs however at $\log U = -1.5$ and $\log n = 11$. However, perhaps a more relevant parameter is the equivalent width, since for any photon flux, the PHL 1811 continuum will be brighter than the K97 (Fig. 13). The equivalent widths in the far UV and IR bands are almost the same, and they are a factor of ~ 2 lower in the UV and optical.

We next look at the behavior of the ratio of the UV Fe II flux in the 2200–3050Å band to the Mg II flux as a function of ionization parameter and density (Fig. 27). Generally speaking, this ratio is larger for gas illuminated by the PHL 1811 continuum compared with the K97 continuum by a factor of ~ 3 or more. As can be seen in Fig. 27, the range in the ratio is large with a strong dependence on ionization parameter; however, the mean obtained from the log of the ratio is ~ 2.8 for the K97 continuum, which is not far from the value measured from composite spectra from the SDSS (3.9 or 5.3, depending on Fe II template, Leighly & Moore 2004). The mean ratio for the PHL 1811 continuum is much higher, around 7.9. The ratio is larger for the PHL 1811 continuum, both because the UV Fe II flux is higher by a factor of ~ 1.8 , and because the Mg II flux is lower by a factor of ~ 1.5 .

Finally, we investigate the dependence of the “spike/gap” ratio as a function of ionization parameter and density (Fig. 28). This ratio is consistently smaller for gas illuminated by the PHL 1811 continuum; the mean for the PHL 1811 continuum is 3.5, and the mean for the K97 continuum is 4.6. Thus the excitation differences discussed are maintained as the ionization parameter and density is varied. We note, however, that even though the spike/gap ratio is lower for PHL 1811, the minimum is 2, which is still much larger than the observed value of ~ 0.7 (Baldwin et al. 2004). But as discussed above, the relatively larger populations at high levels in the gas illuminated by the PHL 1811 is an indication that a more complete atom would produce emission from higher levels, plausibly filling in the gap further.

To summarize this section, we note that the prominence of the Fe II and Fe III in PHL 1811, and the unusual shape of the pseudocontinuum mean that understanding the emission of these lines is important for understanding PHL 1811 in general. Although the tools at our disposal are limited (*Cloudy* does not predict UV Fe III emission lines, does not do radiative transfer properly, and its Fe^+ model atom only goes up to 11.3 eV), we show that the soft SED can qualitatively explain features of the Fe II and Fe III emission. A higher predicted column density of Fe^{+2} predicts stronger Fe III, as observed. Fe II emission is predicted to be generally stronger in gas illuminated by the soft SED, as a consequence of the continuum pumping and interaction with the strong diffuse continuum. This trend is important in the near UV, resulting in a high Fe II/Mg II ratio, as observed. The optical is

less affected, resulting in a high UV-to-optical Fe II ratio, as observed. High excitation and departure coefficients, as well as a low Baldwin et al. (2004) “spike” to “gap” ratio, show that emission from high levels is stronger in gas illuminated by the soft SED, suggesting that the observed strong emission from very high levels may be predicted if a larger model atom were available.

4.4. “Filtering” and He I, H α , and narrow Ly α

As we show in §3.1, we do not detect He I $\lambda 5875$ in PHL 1181. Assuming that He I $\lambda 5875$ has the same profile of H α , we obtain a conservative upper limit of 0.0062 on the He I/H α ratio in PHL 1811. As noted before, Crenshaw (1986) tabulated the fluxes of He I and H α for 9 Seyfert galaxies; the mean He I/H α ratio is 0.061. Thompson (1991) tabulated He I/H α ratio for 6 quasars, and the mean ratio is 0.025. Thus, PHL 1811 has abnormally weak He I emission.

Before going any farther, it is worthwhile reflecting that He I and H α are recombination lines and are thus considerably different from the lines that we have discussed already. Also, in gas illuminated by a typical AGN SED, the transition from He $^+$ to neutral He occurs at approximately the same depth as the transition from H $^+$ to neutral H – the hydrogen ionization front. In a gas illuminated by a soft SED, the continuum runs out of photons that can ionize helium before it runs out of photons that can ionize hydrogen. The result is that there is a region in which hydrogen is ionized and helium is neutral. He I is produced in this region, which means a low He I/H α ratio is more difficult to produce for soft SEDs than for hard ones.

We first use the *Cloudy* simulations using the CLB continua to explore whether we can produce a low He I/H α ratio, especially for soft continua. In this set of simulations we examine the ratio of the simulated flux to the observed flux evaluated at Earth. Representative results as a function of kT_{cut} , ionization parameter, density and depth D , where depth is measured in terms of the depth of the hydrogen ionization front are shown in Fig. 29. We find that H α is almost independent of kT_{cut} and increases with column density. H α decreases at high density at a given ionization parameter because of thermalization. We find that we can produce the H α emission that we see for $kT_{cut} = 10$ and $D = 10$ when $\log(U) = -2$ and $\log(n) = 11.5$, although we note that we have assumed 100% covering fraction, and including a more realistic covering fraction would reduce the model flux. In this region of parameter space, and every other where we can match the H α emission, the predicted He I emission is far too strong. He I decreases with density; however, H α decreases more quickly, and at very high densities and ionization parameters, H α is predicted to be too weak. As discussed

above, we see that at a given depth the He I flux increases as the SED becomes softer.

It is possible to obtain a low He I/H α ratio using the concept of “filtering” that was first introduced in Leighly (2004). In that paper, it was shown that the intermediate- and low-ionization lines of two NLS1s could be better explained if the continuum were transmitted through the wind creating the blueshifted high-ionization lines observed from these objects *before* it illuminates the intermediate- and low-ionization line-emitting gas (see Leighly 2004, for details).

PHL 1811 has blueshifted high-ionization lines, and perhaps filtering can help with the He I/H α problem. Specifically, the continuum may be transmitted through a wind so that the emerging spectrum lacks photons in the He I continuum and yet the column density is such that the hydrogen continuum remains relatively strong. In fact, it is easier to produce such a filtered continuum in gas illuminated by a soft SED, because of the presence of the region of gas in which hydrogen is ionized and helium is neutral. The presence of this region means that the continuum will run out of photons in the He I continuum before it runs out of photons in the hydrogen continuum, yielding the transmitted continuum that we need.

We test this scenario using *Cloudy*. We first show that a continuum with the necessary features can be produced. We use the PHL 1811 continuum shown in Fig. 12. The high N V/He II ratio implies that the metallicity in PHL 1811 may be enhanced; as in Leighly (2004), we assume metals augmented by a factor of five, and nitrogen enhanced by a factor of ten. We first locate the column density at which the ratio of the He $^+$ column to the H $^+$ column is the largest for a range of densities $7.875 \leq \log(n) \leq 12.75$ and ionization parameters $-3.0 \leq \log(U) \leq -1.125$. We then run *Cloudy* models using these column densities, and output the transmitted continua. We identify SEDs with weak He $^+$ continua by taking the ratio of the transmitted plus diffuse emission at 23.9 eV, just below the He I edge at 24.6 eV, and at 28.8 eV, just below the N II edge at 29.6 eV, which seems to be the most prominent feature toward higher energies from the He I edge. We find a very large range in this ratio, from 2.6 to larger than 10^6 . In fact, there is a plateau in the ionization parameter/density plane such that the ratio high for densities less than about $10^{11.5}$, and for ionization parameters higher than -2.0 (Fig. 30). We choose a representative continuum with $\log(U) = -1.5$ and $\log(n) = 11.5$, where the column density at which He $^+/\text{H}^+$ is maximized is $10^{21.3} \text{ cm}^{-2}$. We note that any continuum from the afore-mentioned plateau should produce the same result. The continuum is shown in Fig. 30.

The gas that the continuum is transmitted through will produce line emission. This gas may be the wind that emits the blueshifted lines, as was assumed and required in Leighly (2004). The *Cloudy* simulations show that the strongest predicted line relative to the observed emission lines is Ly α . A covering fraction of 10% ensures that it is predicted

to be no stronger than observed. Also, if the gas filtering the continuum is a wind, the line emission may be broadened and blueshifted, and would be more difficult to distinguish from the continuum than a narrow line. As shown in Fig. 30, much of the energy of the absorbed continuum is emitted as bremsstrahlung in the infrared. This emission will join the transmitted continuum in illuminating the low-ionization line-emitting gas, where it may enhance the low-ionization line emission through free-free absorption (Ferland & Persson 1989).

Finally, we run *Cloudy* simulations to determine whether the predicted He I is reduced as expected; the results for He I are shown in Fig. 31, and the results for H α are shown in Fig. 32. Each figure shows the predicted emission compared with observed as a function of ionization parameter and density for the unfiltered and filtered continuum shown in Fig. 30. We assumed a covering fraction of 10%, noting that the covering fraction must be equal to or smaller than the one required by the line emission in the filtering gas, above. These figures show that H α is predicted to be nearly the same for the direct PHL 1811 continuum and for the transmitted continuum shown in Fig. 30. This is not surprising because the Lyman continuum, responsible for photoionizing the hydrogen, is not much different for the direct and transmitted continua. Including the covering fraction means that we produce sufficient H α for moderate-to-low ionization parameters, high column densities and moderate densities, although we are a factor of two lower than the observed. In contrast, the He I is much weaker for the transmitted continuum, and is now in the vicinity of the measured upper limit for the same parameter choices.

To summarize this section, we used *Cloudy* models to try to understand the very low He I/H α ratio observed from PHL 1811. We found that a soft spectral energy distribution exacerbates the problem; He I should be stronger in objects with soft SEDs because of the large H $^+$ /neutral He zone. We postulated that transmitting the continuum through a wind may yield a “filtered” continuum with a large He I edge, noting that a similar scenario was successful in explaining the intermediate- and low-ionization lines in IRAS 13224–380 and 1H 0707–495 (Leighly 2004). To test this idea, we showed that for column densities chosen to maximize the He $^+$ column to the H $^+$ column ratio, a large area of log(U)–log(n) parameter space would produce transmitted spectral energy distributions with the He I continuum suppressed by a factor of up to 10 6 . That we can create such a continuum is a direct consequence of the presence of a region in gas illuminated by a soft spectral energy distribution where fully ionized hydrogen and He $^+$ coexist; it means that the column density of the filtering gas can be chosen to lie in this region, producing a large He I edge in the transmitted continuum. We show also that transmission through such gas would not be predicted to produce strong line emission that is not observed if we assume a 10% covering fraction. Rather, for a representative case, we see that most of the energy goes

to bremsstrahlung emission in the infrared. We illuminate gas with the filtered continuum, and find that while $\text{H}\alpha$ remains very similar to the unfiltered case, He I is significantly suppressed. Thus, we have demonstrated again that some line emission in AGN can be explained by illumination by continua that have been transmitted through a wind.

4.5. Is PHL 1811 Unique?

PHL 1811, being intrinsically X-ray weak, and lacking strong emission lines, is a very unusual AGN. Are there any others like it? We do not know of any exactly like it, but there are a few that are similar.

As seen in Fig. 9, PHL 1092 and RX J0134.2–4258 have similar far UV spectra; they both also lack strong and prominent $\text{Ly}\alpha$ and C IV lines. PHL 1811 is also similar to these objects in that they all have extreme Eigenvector 1 properties; specifically, they have very high Fe II/[O III] ratios, because they all lack or have relatively weak [O III] emission (PHL 1811: Fig. 2; PHL 1092: e.g., Leighly (1999b); RX J0134.2–4258: Grupe et al. (2000)). They also have unusual X-ray properties. RX J0134.2–4258 had one of the softest X-ray spectra of any AGN observed in the *ROSAT* All Sky Survey, which implies a steep α_{ox} ; later *ROSAT* PSPC and *ASCA* observations found it to have a more typical X-ray spectrum and α_{ox} . It showed rather high amplitude X-ray variability during the *ROSAT* pointed observation and the *ASCA* observation, although typical for a luminous NLS1. The *ROSAT* spectrum of PHL 1092 revealed a very steep spectrum (Forster & Halpern 1996), similar to RX J0134.2–4258. It also showed rather high amplitude short and long time scale X-ray variability for such a luminous quasar (Forster & Halpern 1996; Leighly 1999a; Brandt et al. 1999; Gallo et al. 2004). There may be other objects that are similar for which we have less information, such as RX J2219.9–5941, a luminous NLS1 which shows high amplitude X-ray variability (Grupe et al. 2001, 2004).

The common properties among these three objects are their unusual UV spectrum, their high luminosity for NLS1s (e.g., PHL 1811 is more luminous than all but 2 of the 87 quasars in the Boroson & Green (1992) subsample of the PG quasars), their extreme X-ray properties, and their extreme Eigenvector 1 properties. As noted by Laor (2000), high luminosity NLS1s should have high Eddington ratios. We previously speculated that X-ray weakness in NLS1s is a characteristic of a high Eddington ratio (Leighly 2001). *XMM-Newton* observations of four luminous NLS1s found that one (RX J1225.7+2055) was X-ray weak with $\alpha_{ox} \sim -2.0$ (Matsumoto, Leighly & Kawaguchi 2004). Furthermore, a compilation of α_{ox} values from NLS1s from the literature indicated that X-ray weakness may be more common in luminous NLS1s. In Paper I, we speculated that a high Eddington ratio leads to a weak corona; the

quenching mechanism proposed by Proga (2005) may be applicable.

In the Sloan Digital Sky Survey, some unusual high-redshift QSOs have been discovered that have very blue rest-frame UV spectra, but no discernible emission lines. They are identified as quasars, and their redshifts are obtained from the onset of Ly α forest absorption. The prototype object is SDSSp J153259.96–003944.1 (Fan et al. 1999, hereafter referred to as SDSS J1532–0039). Featureless continua are typically found in BL Lac objects. However, SDSS J1532–0039 does not appear to have other characteristic properties of BL Lac objects; it was not detected in a deep radio observation and was not strongly optically polarized. It has recently been found to be optically variable (Stalin & Srianand 2005); however, this may not be conclusive evidence that it is a BL Lac object, since one luminous NLS1 (PHL 1092; Gallo et al. 2004) has been observed to be tentatively variable in the UV on short time scales. Furthermore, follow-up observations with *Chandra* failed to detect the quasar, indicating an $\alpha_{ox} < -1.74$ (Vignali et al. 2001). We thought that the lack of broad emission lines and the X-ray weakness suggest a similarity to PHL 1811 (Leighly, Halpern & Jenkins 2004).

A few other objects appear equally puzzling. The $z \sim 1$ quasar PG 1407+265 is possibly the first known weak-line object (McDowell et al. 1995). Two more such high redshift objects were found in SDSS (SDSS J130216.13+003032.1 and SDSS J144231.73+011055.3; Anderson et al. 2001). The $z=0.494$ quasar 2QZJ215454.3–305654 (Londish et al. 2004) was found in the 2dF/6dF QSO redshift survey. It has a blue continuum, no detected radio or X-ray emission, and is not polarized. In the Hamburg/ESO survey, the $z=1.8$ quasar HE 0141–3932 was found to have unusually weak Ly α emission; It also has blueshifted high-ionization lines, similar to PHL 1811 (Reimers et al. 2005).

Because of their steep spectra and high amplitude X-ray variability, it has been proposed that NLS1s are characterized by a high accretion rate. Luminous NLS1s should have exceptionally high accretion rates compared with their Eddington value. Luminous high redshift quasars should have large black holes, and in order to grow so large in the short amount of time implied by the standard cosmology, they should be accreting at a rapid rate. If the weak X-ray emission and UV line emission is characteristic of a high accretion rate in a large black hole, it may mean that PHL 1811 is the local prototype of the high- z lineless QSOs (see also Leighly, Halpern & Jenkins 2004).

The observations, however, do not unequivocally support this argument. First of all, not all of the lineless quasars found in the SDSS have weak X-ray emission; some have normal α_{ox} . For example, PG 1407+265 has $\alpha_{ox} = -1.44$ (Wilkes et al. 1999), which is actually flat for a quasar of its 2500Å luminosity ($\log(l_o) = 32.01$; Wilkes et al. 1994). Also, SDSS J144231.73+011055.3 has a relatively flat α_{ox} of -1.37 (Schneider et al. 2005). Furthermore, it is quite possible that some line-less objects are radio-quiet BL Lac objects

(Collinge et al. 2005), i.e., a hypothetical class of objects in which the beamed continuum overwhelms the lines, but unlike ordinary BL Lacs, there is for some reason weak radio and X-ray emission. Thus, it could be that lineless quasars are a heterogeneous population.

Although there are a number of other objects that are quite similar to PHL 1811, the group comprises just a handful, insignificant compared with, for example, the thousands of quasars identified in the SDSS. But can we be confident that we would be able to identify all of these objects? X-ray emission is considered to be an identifying feature of AGN, and it has been shown to be useful for identifying AGN in deep fields (e.g., Brandt & Hasinger 2005), and is even thought to be a key for constraining the AGN contribution to the power in ultraluminous *IRAS* galaxies (e.g., Ptak et al. 2003). PHL 1811 is a powerful quasar with a large black hole, but if it were embedded in a ULIRG it would not be identified as such because of its weak X-ray emission. Quasars are also identified by their radio emission, and PHL 1811 was rediscovered as a member of the FIRST Bright quasar survey. However, it is a weak radio source, and had it been further away, it would not have been found. AGN are commonly identified by their blue color in photometric surveys, and PHL 1811 would have been easily identified as a PG quasar, if it has been in the region of the sky covered by that survey. However, if it were embedded in a dusty starburst host, the continuum would be reddened, and it would be much more difficult to find. One way that we might be able to identify these objects is through their rest-frame infrared properties. It has been shown that AGN can be distinguished from starbursts on the basis of the $F_{25\mu m}/F_{60\mu m}$ flux ratio, which measures the temperature of the dust (e.g., de Grijp, Lub & Miley 1987). Otherwise, if we speculate that X-ray weakness, and weak line emission is a characteristic of a high accretion rate, one might imagine legions of PHL 1811s lying, unidentified, in high redshift galaxies.

5. Summary

In this paper, we report the results and analysis of *HST* STIS optical and UV spectroscopic observations that were coordinated with the *Chandra* observations discussed in Paper I, and contemporaneous ground-based optical observations of the unusually luminous, nearby narrow-line quasar PHL 1811. Here, we summarize the primary results of the paper.

- The optical spectrum indicates that PHL 1811 is a luminous example of a Narrow-line Seyfert 1 galaxy, but the emission lines are not typical of any type of AGN. Overall, the line emission is weak. There is no evidence for forbidden or semi-forbidden line emission. Very low ionization lines are present, including Na I D and Ca II H&K, that are not typically observed in AGN. These lines appear to be narrower than H β . The near-UV region of the spectrum is dominated by Fe II and Fe III. The UV Fe II

emission is strong with respect to both the optical Fe II and Mg II. We find evidence that the UV Fe II and Fe III pseudocontinuum has a different shape in PHL 1811 compared with other AGN including the prototype NLS1 I Zw 1; this appears to be a consequence of a higher ionization/excitation state of the iron in PHL 1811. The C IV line is remarkably weak, with an equivalent width of only 6.6\AA , about 5 times weaker than C IV in quasar composite spectra; it is also broad and blueshifted, similar to the NLS1s IRAS 13224–3809 and 1H 0707–495, indicating an outflow (Leighly & Moore 2004). The region around Ly α is strongly blended, but can be successfully deconvolved using a template created from the C IV profile into Ly α , N V, Si II and C III*. We also find that Si III* is clearly present near 1112\AA .

- In Paper I, we showed that PHL 1811 is intrinsically X-ray weak, and therefore we infer that it has an unusually soft spectral energy distribution. Can a soft SED by itself produce the observed unusual line emission? We explore this question using *Cloudy*, and find that it can. A soft spectral energy distribution is stronger in the UV for a particular photoionizing flux than a hard SED; this is one factor that reduces the observed equivalent widths, but it also enhances lines that are pumped by the continuum, such as high-excitation Si II. The gas is cooler than gas illuminated by a hard SED, but has a higher hydrogen ionization fraction in the partially-ionized zone than might be naively expected. The low temperature means that collisionally-excited line emission, including semforbidden lines and Mg II, is weak. Without the collisionally-excited line emission to cool the gas, the photoionization energy goes to excited states of hydrogen and continuum emission, rather than to the electrons, resulting in the cool temperature. We conclude that the soft SED alone can qualitatively explain the line emission: high-ionization lines are weak because the continuum lacks photons to create the highly-ionized ions, semforbidden and low-ionization collisionally-excited lines are absent because the gas is too cool to excite them, but lines excited by continuum pumping are strong because a soft SED continuum is stronger for a given photoionizing flux than a typical SED. We also compute an LOC model and show that the above results are robust to averaging.
- Fe II and Fe III are very important in the near-UV spectrum. The *Cloudy* iron ion models are too limited to sufficiently model this line emission in detail. Specifically, we see strong Fe III in the spectrum, but no UV Fe III lines are output by the model. In addition, we infer Fe II emission from highly excited levels near 14 eV, but the highest level treated by the model is only 11.3 eV. Finally, *Cloudy* uses a approximation for radiative transfer, and that may be a significant shortcoming in the partially-ionized zone. Nevertheless, *Cloudy* simulations reveal evidence that the Fe II and Fe III emission is qualitatively explained by soft SED. The Fe $^{+2}$ columns are larger in

gas illuminated by the soft SED, for a range of ionization parameters and densities, due to the fact that the H II region is dominated by intermediate-ionization ions, since the usual high-ionization ions are not produced by the soft SED. The predicted Fe II emission is uniformly higher in gas illuminated by the soft SED. This is a consequence of several factors including strong continuum and Ly α pumping, as mentioned above, as well as the presence of a region of gas in which hydrogen is ionized but helium is neutral and where Fe $^+$ is also present. The excitation of Fe $^+$ is higher in the gas illuminated by the soft SED, and relatively high departure coefficients are seen in the highest levels treated by the model, suggesting that emission from even higher levels might be strong. Overall, as far as we can tell given the limitations of the model, the soft SED is responsible for the unusual Fe II and Fe III observed.

- PHL 1811 has a very low ratio of He I $\lambda 5876/\text{H}\alpha$. This is not easy to explain using the soft SED because a soft SED predicts a larger value of this ratio as a consequence of the presence of a region in which hydrogen is ionized but helium is neutral. We observe blueshifted high-ionization lines in this object and postulate that if the continuum were transmitted through optically-thin gas, the resulting “filtered” continuum may be strong in the hydrogen continuum, necessary to create H α , but absorbed in the He I continuum, with a large He I edge. Leighly (2004) showed that a “filtered” continuum was able to better explain the intermediate- and low-ionization line emission in the NLS1s IRAS 13224–3809 and 1H 0707–495. We locate the regions of parameter space for the filtering gas where the required large He I edge will be produced, and demonstrate that illuminating gas with the resulting continuum will produce a low He I/H α ratio as observed.

In this paper, we present a detailed analysis of a single unusual object, PHL 1811. However, a number of things that we have learned may carry over to our understanding of AGN in general. For example, the PHL 1811 spectrum lacks forbidden and semiforbidden lines. Generally, one would interpret weak semiforbidden lines to be a consequence of high density. We showed, however, that weak semiforbidden lines are expected from gas illuminated by a soft SED, which means that semiforbidden lines do not perform well as density indicators when the illuminating SED is soft. How many times have weak semiforbidden lines been taken to be evidence for high density, when in reality, a soft SED is the culprit? The similarity between emission from a high-density gas and gas illuminated by a soft SED is not accidental; they are both a consequence of the inefficiency of collisionally-excited line emission. In the case of PHL 1811, the soft SED is intrinsic, but it is also possible that the soft SED may be the result of filtering. Whether or not a filtered continuum can mimic a high density gas will be the topic of a future paper.

PHL 1811 is a high-luminosity NLS1, and according to the currently-accepted paradigm, these objects should be accreting at the largest rates. Therefore, we may expect that they are present at high redshift. However, they may be difficult to identify as AGN, and there plausibly be a large number embedded in dusty galaxies. The line emission is weak, and in spectra with low signal-to-noise ratio, the optical and UV spectra may appear not to have any emission lines at all. The continuum colors are blue, but that would not be seen if embedded in a dusty galaxy. The X-ray emission is a hallmark of AGN, but it is weak in PHL 1811. The best way to identify similar objects at high redshift may be through their infrared properties.

We thank Bob Becker for observing SDSS J094257.80–004705.2 and SDSS J105023.68–010555.5. KML thanks Eddie Baron and Joe Shields for useful discussions. Part of the work presented here was done while KML was on sabbatical at the Department of Astronomy at The Ohio State University, and she thanks the members of the department for their hospitality. Support for proposal # 09181 was provided by NASA through a grant from the Space Telescope Science Institute, which is operated by the Association of Universities for Research in Astronomy, Inc., under NASA contract NAS5-26555. This research has made use of the NASA/IPAC Extragalactic Database which is operated by the Jet Propulsion Laboratory, California Institute of Technology, under contract with the National Aeronautics and Space Administration.

Facilities: HST (STIS), KPNO:2.1m ()

A. Appendix

In §4 we showed that gas illuminated by the soft spectral energy distribution has rather unique properties that have not been discussed in the literature in the context of AGN emission lines, and these properties produce the unusual line emission in PHL 1811. These unique properties include weak high-ionization lines, low temperatures that result in weak collisionally-excited lines, a strong UV continuum for a given value of photoionizing flux that results in strong pumped lines, and high level of hydrogen ionization in the partially-ionized zone due to the inability of the gas to cool via collisionally-excited line emission. In this appendix we further investigate aspects of the properties of the gas illuminated by the soft spectral energy distribution that are not directly related to interpretation of the spectra, but are nevertheless interesting and are included for completeness. In particular, we are interested in precisely what characteristics of the continuum result in the observed properties; is it the weak X-ray or the weak extreme UV, or both? This issue is examined

in §6.1. We are also interested in whether we can destroy these characteristic properties by including turbulence and changing the metallicity; these issues are discussed in §6.2.

A.1. Effect of the Spectral Energy Distribution

The PHL 1811 spectral energy distribution shown in Fig. 12 differs from a typical quasar in two respects: it is weaker in the extreme UV, and it is weaker in the X-ray. In fact, we do not know the shape of the spectrum in the extreme UV, so in principle it could be brighter in that band. In this section, we examine the influence of these two factors by varying the extreme UV cutoff and the α_{ox} independently.

The spectral energy distributions were constructed from the PHL 1811 SED shown in Fig. 12, with a few changes. First, the PHL 1811 UV continuum extends to $\log \nu = 15.53$ before dropping to the hard X-rays. We round this value down to $\log \nu = 15.5$. We then create another break in the spectrum, in the extreme UV, and vary the frequency of that break between $\log \nu = 15.5$ and 16.4. The upper limit corresponds to about 100 eV. These new points are extrapolated from $\log \nu = 15.5$ along a power law with a slope (in $\log \nu F_\nu$) of 0.5. Then, they are joined to the X-ray, but while the PHL 1811 continuum shown in Fig. 12 joins the X-ray at $\log \nu = 16.76$, we instead join at 17.1, as that better approximates the position of the break in the K97 spectrum. Finally, the X-rays are renormalized to produce an α_{ox} between -2.25 (approximately the observed value for weaker X-ray observation of PHL 1811) and -1.4 (approximately the observed value for K97). The spectral energy distributions are shown in Fig. 33. *Cloudy* models for these 324 SEDs are run for the fiducial parameters ($\log U = -1.5$, $\log n = 11.0$, $\log N_H = 24.5$), yielding a grid of results as a function of α_{ox} and the extreme UV cutoff. PHL 1811 is characteristic of steep α_{ox} and low EUV cutoff (lower left corner of the plots that follow) and K97 is characteristic of flat α_{ox} and high EUV cutoff (upper right corner of the plots that follow).

We first look at the physical characteristics of these spectral energy distributions as a function of α_{ox} and EUV cutoff. The flux at 2500Å is nearly purely dependent on the EUV cutoff, with the largest values being found for the lowest cutoff energies; this makes sense because the majority of the photoionizing photons have energies just larger than 13.6 eV due to the steep dependence of photoionizing flux on energy. Thus, the larger the EUV cutoff, the lower the overall normalization for the same photoionizing flux. In contrast, the Compton temperature is nearly purely dependent on α_{ox} .

We next look at gas properties as a function of depth and normalized to the depth of the hydrogen ionization front. In the H II region, the temperature depends on both α_{ox} and

the EUV cutoff, with the lowest temperatures found for the steepest α_{ox} and lowest-energy EUV cutoff, and the highest temperatures for the flattest α_{ox} and highest-energy EUV cutoff. Then, for lines produced in the H II region, the behavior of the column density of the ion producing the line and the lines themselves depends on the ionization potential, primarily, so that there is dependence on α_{ox} if the ionization potential is high, and limited to dependence on EUV cutoff if the ionization potential is low, roughly speaking. Contours of flux for the high-ionization line C IV and the intermediate-ionization lines C III] λ 1909 and Si III] λ 1892 are shown in Fig. 34.

Turning to the properties of the partially-ionized zone, we examine the temperature, the hydrogen ionization fraction, and the ratio of the excitation temperature to the electron temperature at $n = 2$ at the representative depth of ten times the depth of the hydrogen ionization front (Fig. 35). The temperature depends primarily on α_{ox} for flatter α_{ox} with some dependence on EUV cutoff for steeper α_{ox} . The lowest temperatures occur, not surprisingly, for objects with the steepest α_{ox} and lowest energy EUV cutoff. The hydrogen ionization fraction depends primarily on the EUV cutoff, which shows that photoionization from $n = 2$ by the input continuum is the dominant process. However, at the flattest values of α_{ox} , the hydrogen ionization fraction increases somewhat, due to the additional ionization by nonthermal electrons from photoionization by soft X-rays. That this depends on α_{ox} is not surprising, because the break to the X-ray power law, at 100 eV, is in the soft X-ray band so that the X-ray power law includes a region of high opacity to photoelectric absorption by metals. Finally, the ratio of the excitation temperature to the electron temperature of $n = 2$ hydrogen is a convolution between the temperature and the hydrogen fraction, and the highest values occur for the steepest α_{ox} and lowest EUV cutoff, similar to the PHL 1811 continuum.

The low-ionization lines, excluding Fe II, divide naturally into those that are pumped and those that are collisionally excited. Collisionally excited lines are weakest for the steepest α_{ox} and the lowest values of the EUV cutoff. Examples of such lines are Mg II, C II λ 1335, and Si II λ 1814. The pumped lines follow the UV flux and are strongest for the lowest values of the EUV cutoff. Examples of such lines are the high-ionization Si II lines including those at 1260 and 1194Å. Contours for Mg II, Si II λ 1814, and Si II λ 1194 are shown in Fig. 34. The Fe II lines are all stronger for low values of the EUV cutoff, but in some cases, they increase for flat α_{ox} at a particular value of the EUV cutoff. In this way they resemble the hydrogen ionization fraction shown in Fig. 35. These may be responding to Ly α pumping. Examples of Fe II that appears to be pumped are UV 191, the infrared lines between 7300Å and 3 microns, which are thought arise predominately in cascades after Ly α pumping, and the “gap”. Example of lines that may be responding to Ly α pumping are the “spike” lines and other low-lying levels, and the near-UV band between 2000 and 3000Å. Fig. 34 shows

the results for UV 191, the “spike” and the “gap”.

We also computed the equivalent widths, but since the continuum is much stronger for continua with low EUV cutoffs, they are almost all weaker for low EUV cutoffs and steep α_{ox} . Lines that are purely pumped by the continuum have equivalent widths independent of SED shape.

In this section, we have investigated simulations for only single values of the ionization parameter and the density; computing an average or LOC would provide more robust results but is clearly beyond the scope of this paper and will be pursued in the future. Nevertheless, it seems that we can differentiate between SEDs by the behavior of the high-, intermediate- and low-ionization lines. Intermediate-flux high-ionization line emission will be produced for either high EUV cutoff or flat α_{ox} , or both. Weak high-ionization line emission requires both a low EUV cutoff and a steep α_{ox} . The same is true for intermediate- and collisionally-excited low-ionization line emission. Pumped lines are stronger for low EUV flux.

A.2. Effect of Turbulence and Metallicity

In the simulations presented in §4 and in §6.1, we assumed solar metallicity and no microturbulence. Both of these factors influence the cooling of the gas, and can therefore potentially disrupt the effects of the soft spectral energy distribution discussed previously.

The most extensive investigation of the influence of microturbulence on the line emission in quasars was performed by Bottorff et al. (2000). They noted that microturbulence has two main effects on the spectrum. First, the line optical depths decrease as the line profile is spread over a larger range in wavelength. This causes the lines to be brighter overall as they can escape more freely. The second effect is that continuum pumping becomes more important, again because the line profile has a larger width. As far as the gas properties are concerned, Bottorff et al. (2000) indicated that the temperature will be lower for very large V_{turb} as the photons escape more readily and cool the gas better, but higher for intermediate values due to continuum pumping of lines. They found that most lines become brighter as V_{turb} is increased, but by the same amount, which means that they would not be good diagnostics of the influence of turbulence. Some lines, however, become a lot brighter, including Si II $\lambda 1260$, Si II $\lambda 1305$, C II $\lambda 1335$, and Fe II $\lambda 1787$. Thus, Bottorff et al. (2000) suggested that ratios of these lines with respect to intercombination lines and Si II $\lambda 1814$ would be good diagnostics of turbulence.

There have been a number of publications that discuss the influence of enhanced metallicity. Ferland et al. (1996) discussed the effects of increasing the metallicity on production

of the high-ionization lines, especially N V, with the goal of explaining the high velocity component of Q0207–398. Snedden & Gaskell (1999) discussed the fact that enhanced cooling by higher metallicity gas will result in a somewhat higher characteristic ionization parameter, allowing a smaller characteristic radius and higher characteristic density, thus alleviating discrepancies between photoionization models and reverberation mapping. Hamann et al. (2002) investigated the behavior of various lines as a function of metallicity, with the aim of determining the line ratios that are most robustly sensitive to metallicity variations to use as diagnostics. Finally, Leighly (2004) showed that enhanced metallicity is required to explain unusual high-ionization line ratios in two NLS1s that have very blueshifted high-ionization lines.

In this section, we discuss the effects of the metallicity and turbulence on the properties of the gas illuminated by a soft spectral energy distribution. Our goal is qualitative insight, so we limit ourselves to the fiducial gas parameters ($\log U = -1.5$, $\log n = 11.0$, and $\log N_H = 24.5$). It would be interesting to explore the full parameter space, but that is beyond the scope of this paper.

We first investigate the temperature of the gas as a function of depth normalized to the hydrogen ionization front, shown in Fig. 36. Addition of turbulence results in a higher temperature in both the H II region, and the partially-ionized zone. In the H II region, most of the temperature increase occurs in the neutral He/ionized hydrogen region, and is a consequence of the disappearance of that region; that is, the transition from He^+ to neutral helium moves closer to the hydrogen ionization front. There is an overall increase in the level of ionization in the H II region, including a decrease in the Fe^{+2} column. This is probably a consequence of the fact that ions are better able to absorb continuum photons, and so the energy of the continuum is released into the gas. In the partially-ionized zone, the temperature increase is a consequence of the loss of the synergy described in §4. Once the temperature becomes high enough that metal ions can be collisionally excited, the amount of energy in the continuum decreases, the excitation temperature decreases, and the energy previously locked up in the excited hydrogen and continua is released to heat the gas.

Turning to the metallicity, we find that the temperature is lower for higher metallicities only for the highest ionization regions of the gas. In this region, the optical depth is relatively low and the photons escape, cooling the gas. In the intermediate-ionization regions, and the partially-ionized zone, the temperature is higher for higher metallicity. In this case, the region where hydrogen is ionized and helium is neutral becomes larger as the metallicity increases. Practically all metal-ion columns increase along with metallicity, although with different slopes. Photoionization of a metal ion releases more energy than a hydrogen ion, and in regions where the gas is starting to have appreciable optical depth, those photons may

not be able to readily escape to cool the gas. In the partially-ionized region, the temperature increases because the availability of more metal ions to excite means that not so much energy goes into the continuum and excited-state hydrogen, so it is released into the gas.

Next we turn to the lines. The behavior of the lines as a function of turbulence has already been investigated by Bottorff et al. (2000); we look at only a few lines that behave differently for the PHL 1811 and K97 continuum for this particular choice of ionization parameter. As discussed in §4.1.3, Mg II is weak in PHL 1811 because the temperature is low. As seen in the top left panel of Fig. 37, Mg II increases more quickly with increasing turbulence in gas illuminated by the PHL 1811 continuum compared with the K97 continuum as a result of the increasing temperature in the line emitting gas. This is also true for the collisionally excited line Si II λ 1814. In contrast, the Si II λ 1263, which is predominately excited by continuum pumping, increases at the same rate in both cases. Next, we turn to the semiforbidden lines Si III] λ 1892 and C III] λ 1909. The transitions producing these lines have low gf values, so they do not become optically thick, and should not be influenced by lower opacity of the turbulent gas. Indeed, for the gas illuminated by the K97 continuum, there is very little dependence on turbulence. However, there is fairly strong increase in the flux of these collisionally-excited lines in gas illuminated by the PHL 1811 continuum that is a consequence of the increase in temperature.

The results when the metallicity is varied are somewhat different (Fig. 37, right). Generally speaking, the generally prominent high-ionization metal lines (e.g., C IV) do not vary much with metallicity; their emission is primarily a function of gas temperature. The intermediate- and low-ionization metal lines increase with metallicity, generally speaking, although with a range of slopes. Mg II increases more quickly with metallicity for the gas illuminated by the PHL 1811 continuum compared with the gas illuminated by the K97 continuum; this is probably a consequence of the increase in gas temperature in the partially-ionized zone as the metallicity is increases. Both Si III] and C III] increase with metallicity, although with different slopes, again pointing to a lack of robustness as a density indicator. Also, the increase is more rapid for the K97 continuum for many of the intermediate ionization lines. This seems to be a consequence of changes in the ionization structure of the gas as well as the change in temperature. Finally, we examine the “spike” and “gap” Fe II bands (Baldwin et al. 2004). We see that both increase more rapidly for the PHL 1811 continuum, but with the “spike” (resonance lines and low-lying levels) increasing more rapidly than the “gap” (high-excitation Fe II). Recall that the model spike/gap ratio is much larger than observed; thus a high metallicity only exacerbates the problem.

To summarize this section, we have investigated the effects of turbulence and metallicity changes on the gas properties and emission. In order to obtain a qualitative understanding,

we have limited ourselves to a single representative ionization parameter and density. We find that as the metallicity and turbulence increase, the temperature increases and the energy in the continuum decreases, and this generally causes an increase in the emission line fluxes. Naturally, lines that are collisionally excited are more sensitive to the temperature increase. Weak collisionally-excited line emission is a characteristic of the PHL 1811 spectrum, so these results may mean that a high degree of turbulence and high metallicity are not present in this object.

REFERENCES

Anderson, S. F., et al. 2001, AJ, 122, 503

Baldwin, J. A. 1977, MNRAS, 178, 67

Baldwin, J. A., Ferland, G. J., Korista, K. T., Carswell, R. F., Hamann, F., Phillips, M. M. Verner, D., Wilkes, B. J., & Williams, R. E. 1996, ApJ, 461, 664

Baldwin, J. A., Ferland, G. J., Korista, K. A., Hamann, F., & LaCluyzé, A. 2004, ApJ, 615, 610

Baldwin, J., Ferland, G., Korista, K., & Verner, D. 1995, ApJ, 455, 119

Baskin, A., & Laor, A. 2004, MNRAS, 350, 31

Becker, R. H., White, R. L., & Helfand, D. J. 1995, ApJ, 450, 599

Begelman, M. C. 2002, ApJ, 568, L97

Blundell, K. M., Beasley, A. J., & Bicknell, G. V. 2003, ApJ, 59, L103

Boroson, T. A., & Green, R. F. 1992, ApJS, 80, 109

Bottorff, M., Ferland, G., Baldwin, J., & Korista, K. 2000, ApJ, 542, 644

Brandt, W. N., Boller, T., Fabian, A. C., & Ruszkowski, M. 1999, MNRAS, 303, 53

Brandt, W. N., & Hasinger, G. 2005, ARAA, 43, in press

Brandt, W. N., Laor, A., & Wills, B. J. 2000, ApJ, 528, 637

Brotherton, M. S., Tran, H. D., Becker, R. H., Gregg, M. D., Laurent-Muehleisen, S. A., & White, R. L. 2001, ApJ, 546, 775

Cardelli, J. A., Clayton, G. C., & Mathis, J. S. 1992, *ApJ*, 345, 245

Casebeer, D. A., Leighly, K. M., & Baron, E. 2006, *ApJ*, 637, 157

Collinge, M. J., et al. 2005, *AJ*, 129, 2542

Collin-Souffrin, S., & Dumont, A. M. 1989, *A&A*, 213, 29

Corbin, M. R., & Boroson, T. A. 1996, *ApJS*, 107, 69

Crenshaw, D. M. 1986, *ApJS*, 62, 821

de Grijp, M. H. K., Lub, J., & Miley, G. K. 1987, *A&AS*, 70, 95

Dhanda, N., Baldwin, J. A., Bentz, M. C., & Osmer, P. S., 2007, *ApJ*, in press, astro-ph/0612610

Dietrich, M., Crenshaw, D. M., & Kraemer, S. B. 2005, *ApJ*, 623, 700

Dietrich, M., Hamann, F., Appenzeller, I., & Vestergaard, M. 2003, *ApJ*, 596, 817

Dietrich, M., Hamann, F., Shields, J. C., Constantin, A., Vestergaard, M., Chaffee, F., Foltz, C. B., & Junkkarinen, V. T. 2002, *ApJ*, 581, 912

Fan, X., et al. 1999, *ApJ*, 526, 57

Ferland, G. J. 1999, in Proc. “Quasars and Cosmology”, Eds. G. Ferland & J. Baldwin (ASP: San Francisco), p. 147

Ferland, G. J., Baldwin, J. A., Korista, K. T., Hamann, F., Carswell, R. F., Phillips, M., Wilkes, B., & Williams, R. E. 1996, *ApJ*, 461, 683

Ferland, G. J., & Persson, S. E. 1989, *ApJ*, 347, 656

Forster, K., Green, P. J., Aldcroft, T. L., Vestergaard, M., Foltz, C. B., & Hewitt, P. C. 2001, *ApJS*, 134, 35

Forster, K., & Halpern, J. P. 1996, *ApJ*, 468, 565

Francis, P. J., Hewett, P. C., Foltz, C. B., Chaffee, F. H., Weymann, R. J., & Morris, S. L. 1991, *ApJ*, 373, 465

Gallagher, S. C., Brandt, W. N., Chartas, G., & Garmire, G. P. 2002, *ApJ*, 567, 37

Gallo, L. C., Boller, T., Brandt, W. N., Fabian, A. C., & Grupe, D. 2004, *MNRAS*, 352, 744

Goodrich, R. W., 2000, *NewAR*, 44, 519

Grupe, D., Leighly, K. M., Burwitz, V., Predehl, P., & Mathur, S. 2004, *AJ*, 128, 1524

Grupe, D., Leighly, K. M., Thomas, H.-C., & Laurent-Muehleisen, S. A. 2000, *A&A*, 356, 11

Grupe, D., Thomas, H.-C., & Leighly, K. M. 2001, *A&A*, 369, 450

Hall, P. B., et al. 2004, Proc. “Multiwavelength AGN Surveys,” eds. R. Mujica & R. Maiolino, astro-ph/0403347

Hamann, F., & Ferland, G. 1993, *ApJ*, 418, 11

Hamann, F., Korista, K. T., Ferland, G. J., Warner, C., & Baldwin, J. 2002, *ApJ*, 564, 592

Haro, G., & Luyten, W. J. 1962, *Bol. Inst. Tonantzintla*, 3, 37

Jenkins, E. B., Bowen, D. V., Tripp, T. M., & Sembach, K. R. 2005, *ApJ*, 623, 767

Jenkins, E. B., Bowen, D. V. Tripp, T. M., Sembach, K. R., Leighly, K. M., Halpern, J. P., & Lauroesch, J. T. 2003, *AJ*, 125, 2824

Johansson, S., Brage, T., Leckrone, D. S., Nave, G., & Wahlgren, G. M. 1995, *ApJ*, 446, 361

Johansson, S., & Hansen, J. E. 1988, in “Physics of Formation of Fe II lines outside LTE”, eds R. Viotti, A. Vittone, & M. Friedjung (Dordrecht: Reidel), 13

Johansson, S., Zethson, T., Hartman, H., Ekberg, J. O., Ishibashi, K., Davidson, K., & Gull, T. 2000, *A&A*, 361, 977

Joly, M. 1989, *A&A*, 208, 47

Kim Quijano, J., et al., 2003, “STIS Instrument Handbook”, Version 7.0, (Baltimore: STScI)

Korista, K. T., et al. 1995, *ApJS*, 97, 285

Korista, K., Baldwin, J., Ferland, G., & Verner, D. 1997, *ApJS*, 108, 401 (K97)

Krolik, J. H., & Kallman, T. R. 1988, *ApJ*, 324, 714

Kwan, J., & Krolik, J. H. 1981, *ApJ*, 250, 478

Laor, A. 2000, *NewA Rev.*, 44, 503

Laor, A., Jannuzzi, B. T., Green, R. F., & Boroson, T. A. 1997, *ApJ*, 489, 656

Laor, A., & Netzer, H. 1989, MNRAS, 238, 897

Leighly, K. M. 1999, ApJS, 125, 297

Leighly, K. M. 1999, ApJS, 125, 317

Leighly, K. M. 2001, in “X-ray Emission from Accretion onto Black Holes”, eds. T. Yaqoob & J. H. Krolik, published electronically (<http://www.pha.jhu.edu/groups/astro/workshop2001/>)

Leighly, K. M. 2004, ApJ, 611, 125

Leighly, K. M., Halpern, J. P., Helfand, D. J., Becker, R. H., & Impey, C. D. 2001, AJ, 121, 2889

Leighly, K. M., Halpern, J. P., & Jenkins, E. B. 2004, in Proc. “AGN Physics with the Sloan Digital Sky Survey”, eds. G. T. Richards & P. B. Hall (ASP: San Francisco), 277

Leighly, K. M., Halpern, J. P., Jenkins, E. B., Grupe, D., Choi, J., & Prescott, K. B., 2007, accepted for publication in ApJ, astro-ph/0611349

Leighly, K. M., & Moore, J. R. 2004, ApJ, 611, 107

Leighly, K. M., & Moore, J. R. 2006, ApJ, 644, 748

Londish, D., Heidt, J., Boyle, B. J., Croom, S. M., & Kedziora-Chudczer, L. 2004, MNRAS, 352, 903

Matsumoto, C., Leighly, K. M., & Kawaguchi, T. 2004, Progress of Theoretical Physics Supplement, 155, 377

McDowell, J. C., Canizares, C., Elvis, M., Lawrence, A., Markoff, S., Mathur, S., & Wilkes, B. J., 1995, ApJ, 450, 585

Netzer, H. 1987, MNRAS, 225, 55

Nomoto, K., Nakamura, T., & Kobayashi, C. 1999, ApJS, 265, 37

Persson, S. E., 1988, ApJ, 330, 751

Proga, D., 2005, ApJ, 630, L9

Ptak, A., Heckman, T., Levenson, N. A., Weaver, K., & Strickland, D. 2003, ApJ, 592, 782

Reimers, D., Janknecht, E., Fechner, C., Agafonova, I. I., Levshakov, S. A., & Lopez, S. 2005, A&A, 435, 17

Rees, M. J., Netzer, H., & Ferland, G. J. 1989, ApJ, 347, 640

Rudy, R. J., Mazuk, S., Puetter, R. C., & Hamann, F. 2000, ApJ, 539, 166

Schlegel, D. J., Finkbeiner, D. P., & Davis, M. 1998, ApJ, 500, 525

Schneider, D. P., et al. (2005), AJ, 130, 367

Shang, Z., et al., 2005, ApJ, 619, 41

Snedden, S. A., & Gaskell, C. M. 1999, ApJ, 521, L91

Stalin, C. S., & Srianand, R. 2005, MNRAS, 359, 1022

Steffen, A. T., Strateva, I., Brandt, W. N., Alexander, D. M., Koekemoer, A. M., Lehmer, B. D., Schneider, D. P., & Vignali, C., 2006, AJ, 131, 2826

Telfer, R. C., Zheng, W., Kriss, G. A., & Davidsen, A. F. 2002, ApJ, 565, 773

Thompson, K. L. 1991, ApJ, 374, 496

Vanden Berk, D. E., et al. 2001, AJ, 122, 549

Véron-Cetty, M.-P., Joly, M., & Véron, P. 2004, A&A, 417, 515

Véron-Cetty, M.-P., Joly, M., Véron, P., Boroson, T., Lipari, S., & Ogle, P. 2006, A&A, 451, 851

Verner, E., Bruhweiler, F., Verner, D., Johansson, S., Kallman, T., & Gull, T. 2004, ApJ, 611, 780

Vestergaard, M., & Wilkes, B. J. 2001, ApJS, 134, 1

Vignali, C., Brandt, W. N., Fan, X., Gunn, J. E., Kaspi, S., Schneider, D. P., & Strauss, M. A. 2001, AJ, 122, 2143

Walter, R., Orr, A., Courvoisier, T. J.-L., Fink, H. H., Makino, F., Otani, C., & Wamsteker, W. 1994, A&A, 285, 119

White, R. L. Becker, R. H., Helfand, D. J., & Gregg, M. D. 1997, ApJ, 475, 479

Wilkes, B. J., Tananbaum, H., Worrall, D. M., Avni, Y., Oey, M. S., & Flanagan, J. 1994, ApJS, 92, 53

Wilkes, B. J., Kuraszkiewicz, J., Green, P. J., Mathur, S., & McDowell, J. C. 1999, ApJ, 513, 76

Zheng, W., Kriss, G. A., Telfer, R. C., Grimes, J. P., & Davidsen, A. F. 1997, ApJ, 475, 469

Table 1. Observing log

| Spectrometer | Date | Exposure (seconds) | Bandpass | Slit Width | Resolution |
|------------------------------|------------|-----------------------|-------------|------------|------------|
| HST STIS FUV MAMA (G140L) | 2001-12-03 | 2640 | 1119–1715 Å | 0.2'' | 1.2Å |
| HST STIS NUV MAMA (G230L) | 2001-12-03 | 1667 | 1576–3159 Å | 0.2'' | 5.2Å |
| HST STIS Optical CCD (G430L) | 2001-12-03 | 240 | 2894–5702 Å | 0.2'' | 5.5Å |
| KPNO 2.1m Goldcam | 2001-07-23 | 2700 | 6080–9160Å | 1.9'' | 4Å |
| KPNO 2.1m Goldcam | 2001-10-24 | 900 | 3938–7597 Å | 1.9'' | 5Å |
| KPNO 2.1m Goldcam | 2001-10-25 | 900 | 5466–8532 Å | 1.9'' | 4Å |

Table 2. Emission-line properties

| Emission Line | Line Model ^a | Measured Wavelength ^{b,c} (Å) | Lab. Wavelength ^{b,c} (Å) | Flux (10^{-14} erg cm $^{-2}$ s $^{-1}$) | Equivalent Width (Å) | Velocity Width ^d (km s $^{-1}$) |
|---------------------------|-------------------------|---|---------------------------------------|---|-------------------------|--|
| He I | L (UL) | 7067.2 (f ^e) | 7067.2 | < 0.048 | < 0.17 | 1752(f) |
| H α ^f | L | 6564.12 \pm 0.04 | 6564.7 | 100.6 \pm 0.2 | 302 | 1752 \pm 6 |
| H β ^g | L | 4864.2 \pm 0.09 | 4862.7 | 29.4 \pm 0.2 | 50 | 1943 \pm 19 |
| H γ ^g | L | 4347.1 \pm 0.3 | 4341.7 | 9.5 \pm 0.3 | 12 | 1716 \pm 60 |
| Na I D | L(2,thick) | 5893.5 \pm 0.6 | 5893.58 | 1.95 \pm 0.06 | 4.9 | 1590 \pm 125 |
| Na I D | L(2,thick,+He I) | 5894.5 \pm 1.1 | 5893.58 | 1.61 \pm 0.12 | 4.1 | 1365 \pm 180 |
| He I | L(+Na I D; UL) | 5879.2 \pm 0.7 | 5877.45 | 0.63 | 1.6 | 1752(f) |
| Ca II H | G | 3936.6 \pm 0.4 | 3934.8 | 1.30 \pm 0.12 | 1.3 | 993 \pm 82 |
| Ca II K | G | 3971.4 | 3969.6 | 1.02 \pm 0.10 | 1.1 | 993 |
| Mg II | G(2,thick) | 2800.3 \pm 0.4 | 2800.0 | 28.2 \pm 0.5 | 12.9 | 2550 \pm 110 |
| C III] | integrated flux UL | 1915.8 | 1908.7 | < 7.3 | < 1.7 | |
| Al III | G(2,thick) | 1850.5 \pm 0.8 | 1858.8 | 8.3 \pm 0.4 | 1.9 | 3210 \pm 340 |
| Fe III ₁₉₁ | G(3) | 1783.18 \pm 0.25 | 1786.3 | 3.27 \pm 0.13 | 0.74 | 1140 \pm 120 |
| Si II | T (UL) | 1815.02 (f) | 1815.02 | < 6.1 | < 1.4 | |
| He II | T (UL) | 1640.41 (f) | 1640.41 | < 5.2 | < 1.11 | |
| C IV | T | 1549.5 | 1549.5 | 32.0 \pm 0.7 | 6.6 | |
| unidentified ^h | G | 1395.2 \pm 1.7 | | 28.0 \pm 3.0 | 5.0 | 8470 \pm 710 |
| C II | T (UL) | 1335.31 (f) | 1335.31 | < 7.9 | < 1.3 | |
| Si II | T | 1302.0 \pm 0.95 | 1307.62 | 14.9 \pm 0.8 | 2.4 | |
| Si II | T | 1259.9 \pm 1.8 | 1263.32 | 52.0 \pm 1.1 | 7.9 | |
| N V | T | 1236.3 \pm 0.4 | 1240.15 | 60.5 \pm 1.3 | 9.0 | |
| Ly α | T | 1216.0 \pm 0.5 | 1215.67 | 41.5 \pm 1.2 | 6.0 | |
| Si II | T | 1193.6 \pm 0.6 | 1194.12 | 25.6 \pm 1.0 | 3.6 | |
| C III* | T | 1175.4 \pm 0.5 | 1175.67 | 13.8 \pm 0.9 | 1.9 | |
| Si III* | G(1) | 1110.9 \pm 0.5 | 1111.59 | 1.5 \pm 0.3 | 0.20 | 1160 \pm 230 |
| Si III* | G(6) | 1110.5 \pm 0.3 | 1111.59 | 1.7 \pm 0.03 | 0.22 | 690 \pm 130 |
| N II | G(1) | 1084.2 \pm 0.2 | 1085.12 | 0.90 \pm 0.20 | 0.11 | 460 \pm 110 |
| N II | G(6) | 1084.2 \pm 0.2 | 1085.12 | 0.95 \pm 0.02 | 0.12 | 370 \pm 150 |

^aCodes for line models are as follows: L=Lorentzian profile; UL=upper limit ($\Delta\chi^2 = 6.63$); “thick” means that we set multiplet ratios equal to one; G=Gaussian line profile; T=C IV template was used for the profile; a number gives the number of components in the fit, usually the number of multiplets, or “1” if fitted with a single line.

^bFor multiplets, we list the gf weighted values, unless marked “thick” in column 2, in which case we give the average wavelength.

^cVacuum wavelengths.

^dUncorrected for detector resolution.

^d(f) means that the parameter was fixed at the value given.

^fUsing the Véron-Cetty, Joly, & Véron Fe II template subtraction.

^gUsing the Boroson & Green Fe II template subtraction.

^hThis 1400Å feature is likely to be a blend of Si IV and O IV]; since the identification is ambiguous, it is labeled as unidentified.

Table 3. LOC Model Results

| Emission Line | Composite Spectra Equivalent Widths ^a | | | | K97 LOC ^b | PHL 1811 LOC ^b | PHL 1811 Observed |
|--------------------------|--|-------|------------------|-------------------|----------------------|---------------------------|-------------------|
| | Francis | Zheng | Brotherton | Vanden Berk | | | |
| Ly α +N V feature | 52 | | 87 | | 94.6 | | |
| Ly α | | 85 | | 92.9 | 90.2 | 26.5 | 6.0 |
| N V | | 10 | | 1.11 | 4.4 | 0.06 | 9.0 |
| 1400 Å feature | 10 | 7.3 | 8 | 8.1 | 5.9 | 0.3 | 5.0 |
| C IV | 37 | 59 | 33 | 23.8 | 47.2 | 0.9 | 6.6 |
| He II | 12 ^c | 3.9 | 7.0 ^c | 0.51 | 12.7 | 0.24 | < 1.1 |
| 1900 Å feature | 22 | | 17 | | 14.2 | 3.0 | |
| Al III | | 3.5 | | 0.40 | 1.3 | 0.14 | 1.9 |
| Si III] | | 3.5 | | 0.16 ^d | 6.4 | 1.1 | |
| C III] | | 17.0 | | 21.2 ^e | 6.4 | 1.7 | < 1.7 |
| Mg II | 50 | 64 | 34 | 32.3 | 107 | 15.0 | 12.9 |

Note. — All values are equivalent widths in Å.

^aReferences for composite spectra are Francis et al. (1991), Zheng et al. (1997), Brotherton et al. (2001), and Vanden Berk et al. (2001).

^bA covering fraction of 0.25 was assumed.

^cHe II λ 1640+O III] λ 1663.

^dIncludes also part of Fe III UV 34.

^eIncludes also part of Fe III UV 34, UV 68, and UV 61.

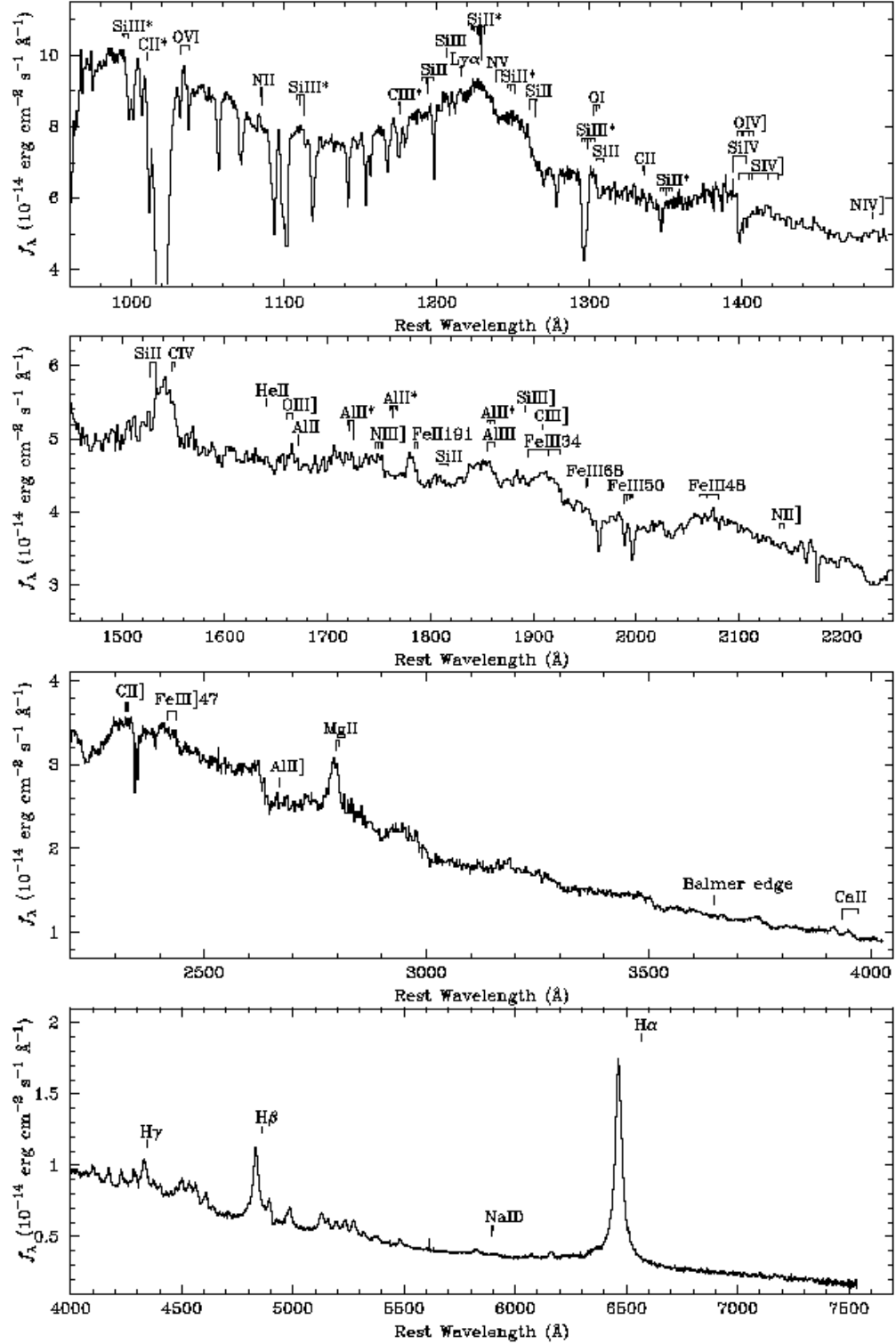


Fig. 1.— Merged UV and optical spectra. Prominent lines expected in active galaxies are labeled, along with a number of metastable lines. Length of tick marks is proportional to gf for individual multiplets. Absorption lines, almost all of which are identified as originating in our Galaxy or in intervening absorption systems, are identified in Jenkins et al. (2003).

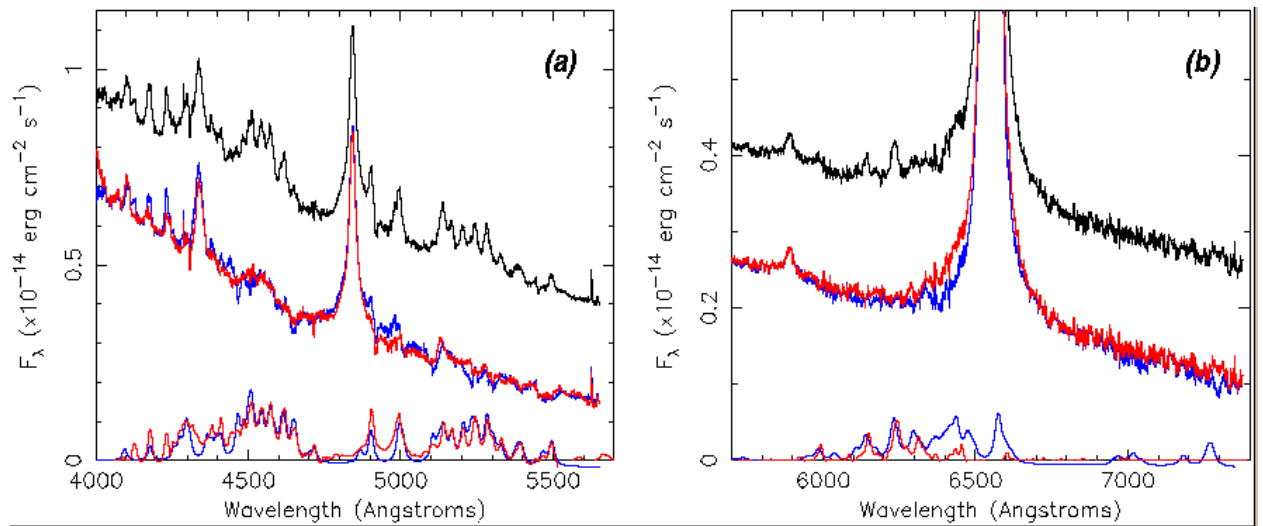


Fig. 2.— Optical spectra near the H β (a) and H α regions (b). The top lines show the original spectra. The offset middle lines show the Fe II subtracted spectra, where the blue and red lines show the results using the Véron-Cetty, Joly, & Véron (2004) and Boroson & Green (1992) iron emission templates, respectively (bottom lines). Note that the Véron-Cetty, Joly, & Véron (2004) template subtraction yields a more symmetric H α line.

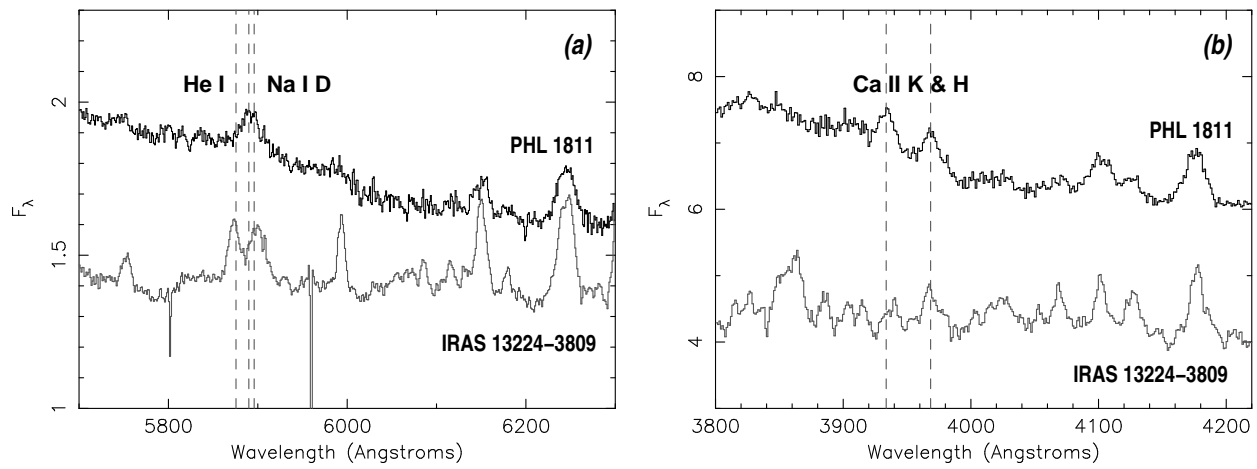


Fig. 3.— We observe unusual very low-ionization line emission from Na ID (a) and Ca II K&H (b) in PHL 1811, but we observe no convincing evidence for He I. For comparison, the offset spectrum from the narrow-line Seyfert 1 galaxy IRAS 13224–3809 is shown.

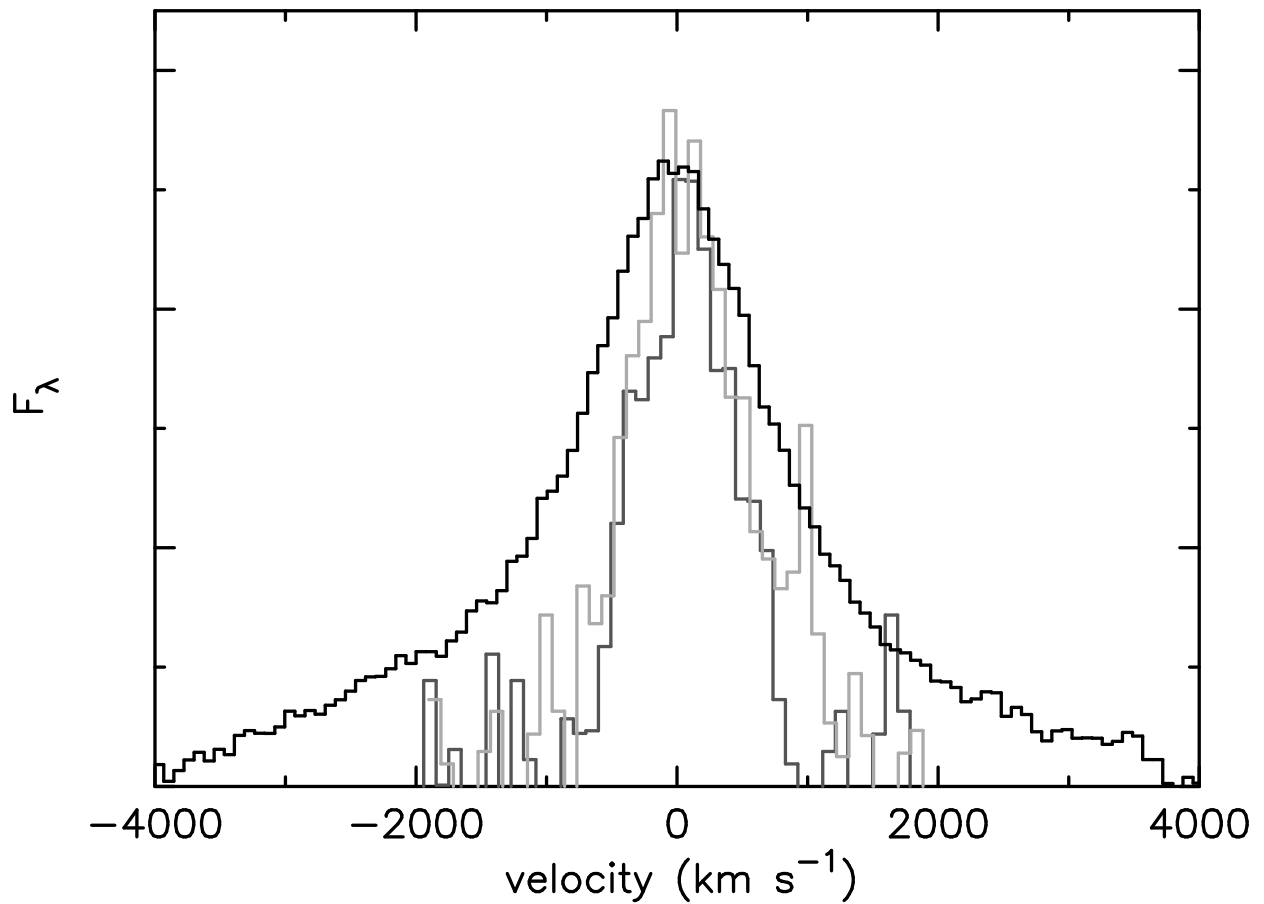


Fig. 4.— A comparison of the Ca II H&K (grey lines) and H β (black line) profiles in velocity space shows that the Ca II lines are distinctly narrower.

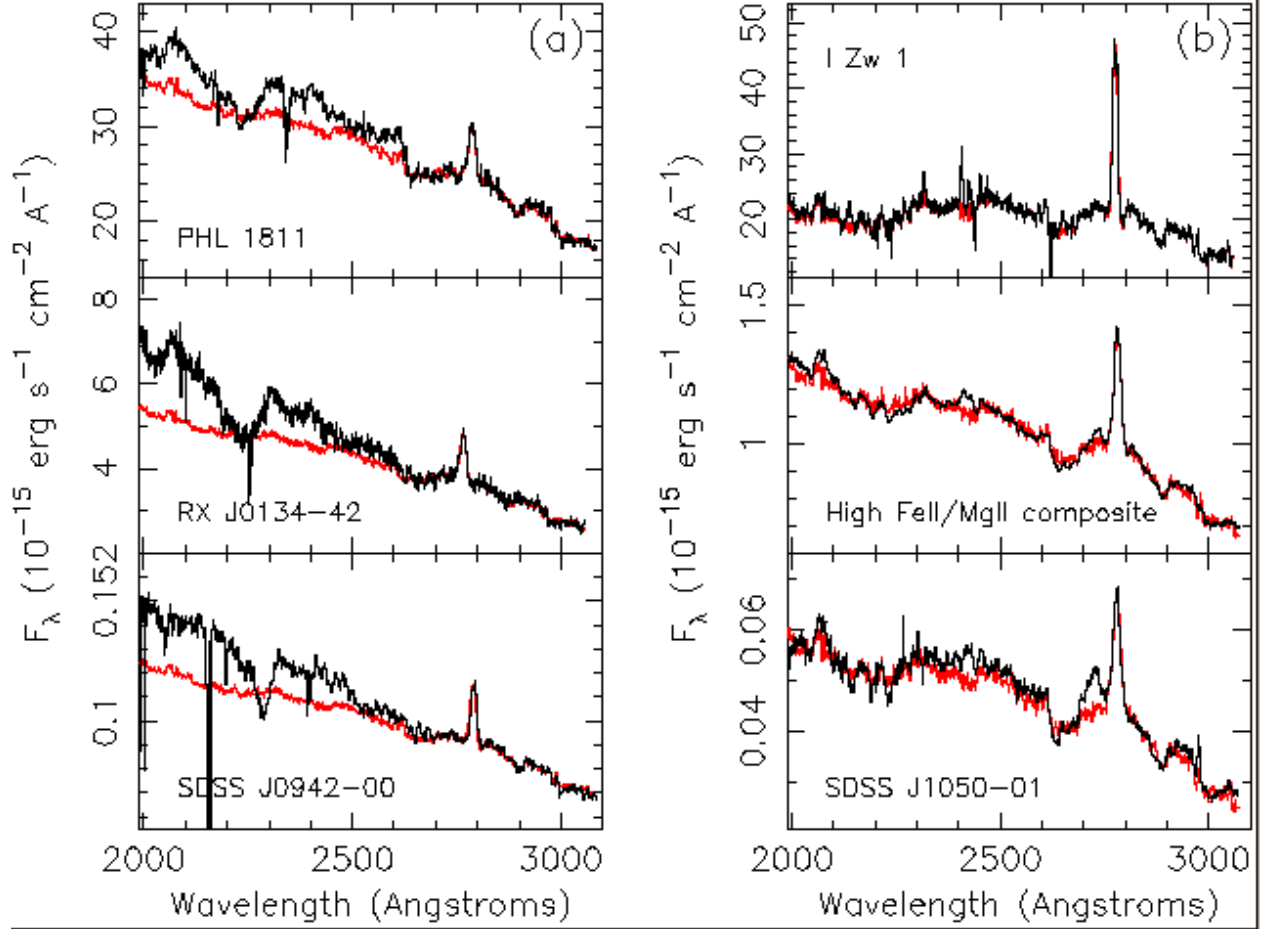


Fig. 5.— UV Fe II in PHL 1811 and other quasars. The spectra shown were fitted between 2650 and 3090 Å with a model that included two Gaussians to model the Mg II emission at 2800Å and the Fe II template plus a line to model the continuum. Then the model was extrapolated toward shorter wavelengths. (a) The extrapolated model leaves excesses between 2300 and 2500 Å, originating in high-excitation Fe II, and shortward of 2200 Å, originating in Fe III. PHL 1811 falls into this category. (b) the extrapolated model fits these spectra well.

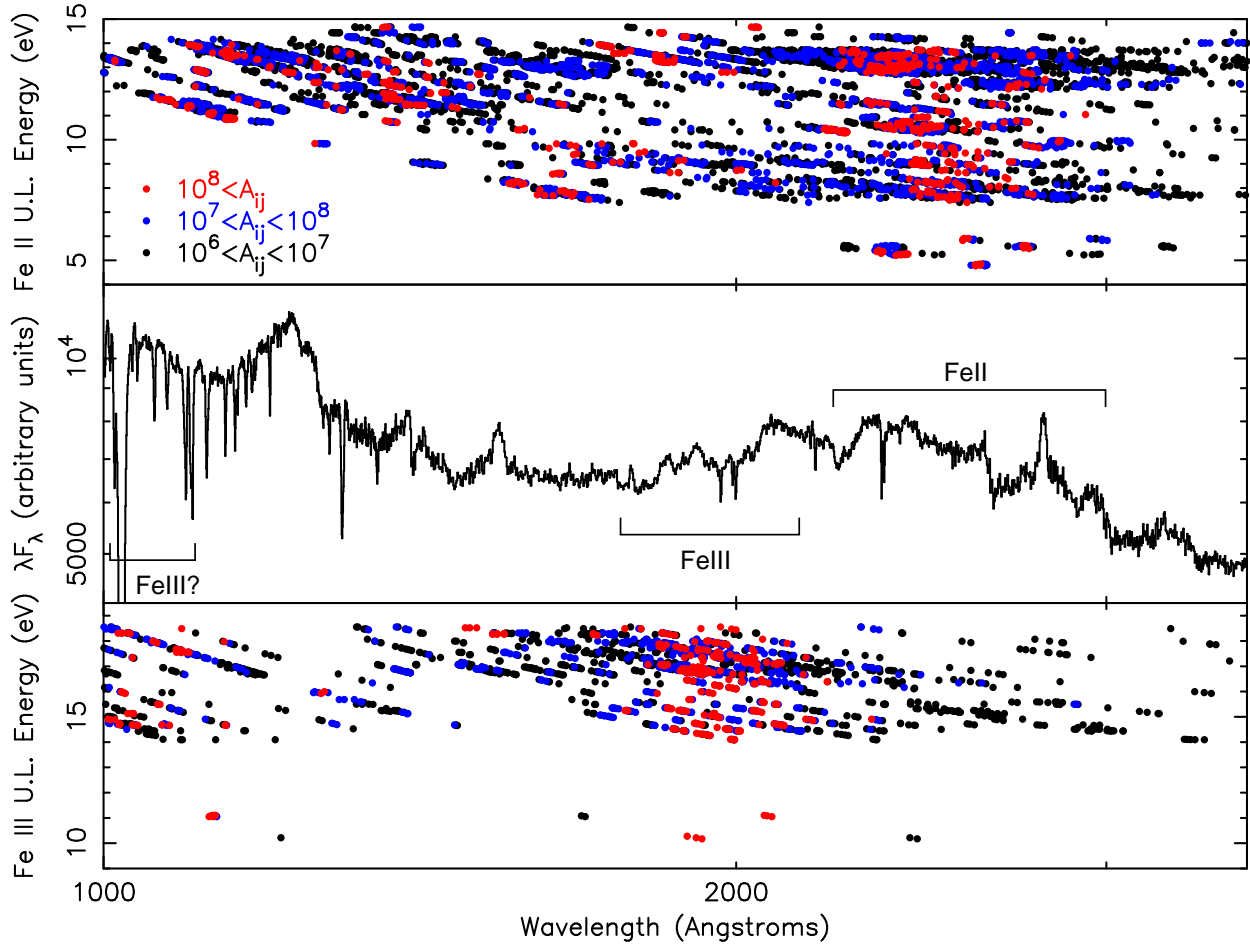


Fig. 6.— *Top:* The upper level energies for Fe II emission lines, color coded according to their A_{ij} value. *Middle:* the λF_λ spectrum of PHL 1811. *Bottom:* Same as the top panel, for Fe III.

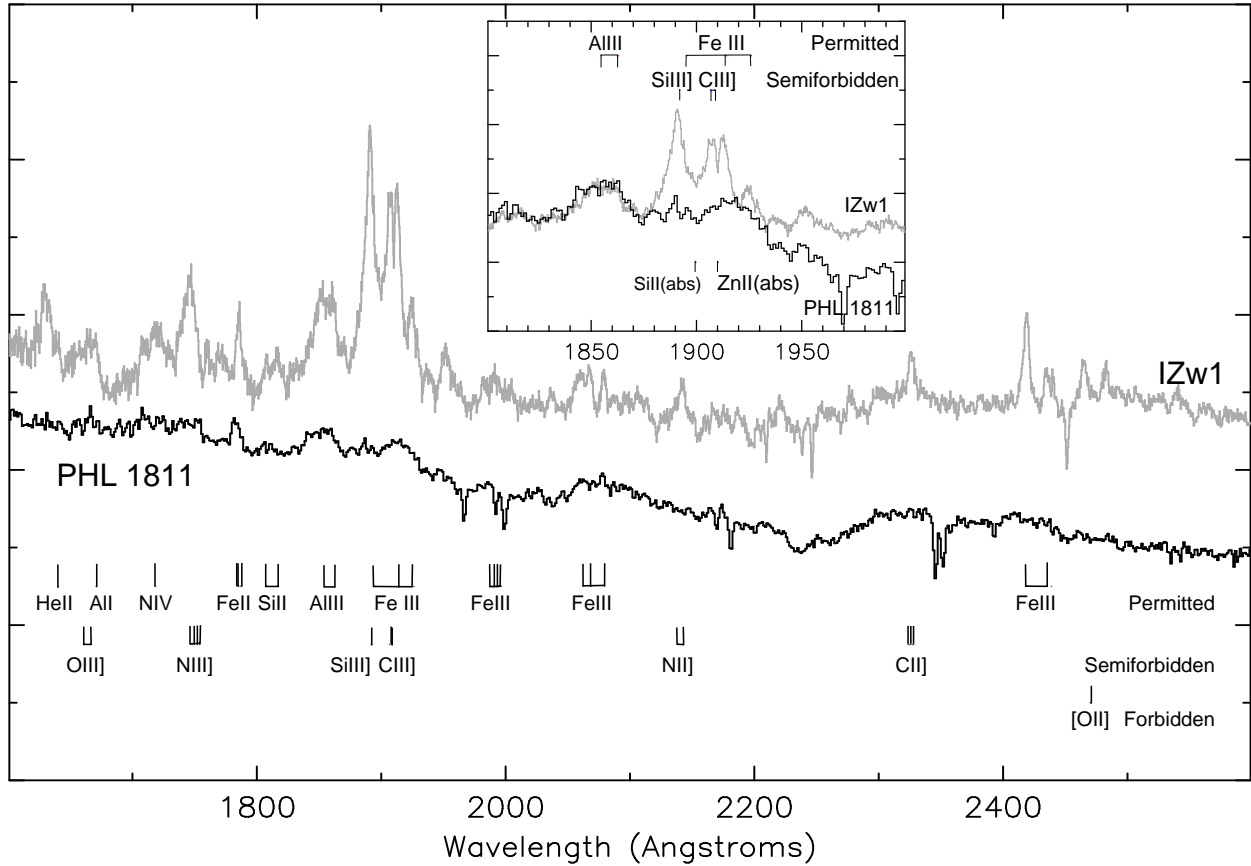


Fig. 7.— The near-UV spectrum of PHL 1811. Positions of permitted, semiforbidden and forbidden lines commonly seen in AGN spectra are marked. All of these lines are present in the I Zw 1 spectrum, but forbidden and semiforbidden lines are absent in PHL 1811. A feature near 1915\AA is near the expected position of C III] $\lambda 1909$. The inset shows that the centroid of this feature is redward of the expected position of C III], and it is more likely to be the 1914.1\AA component of Fe III UV34 (see text for details).

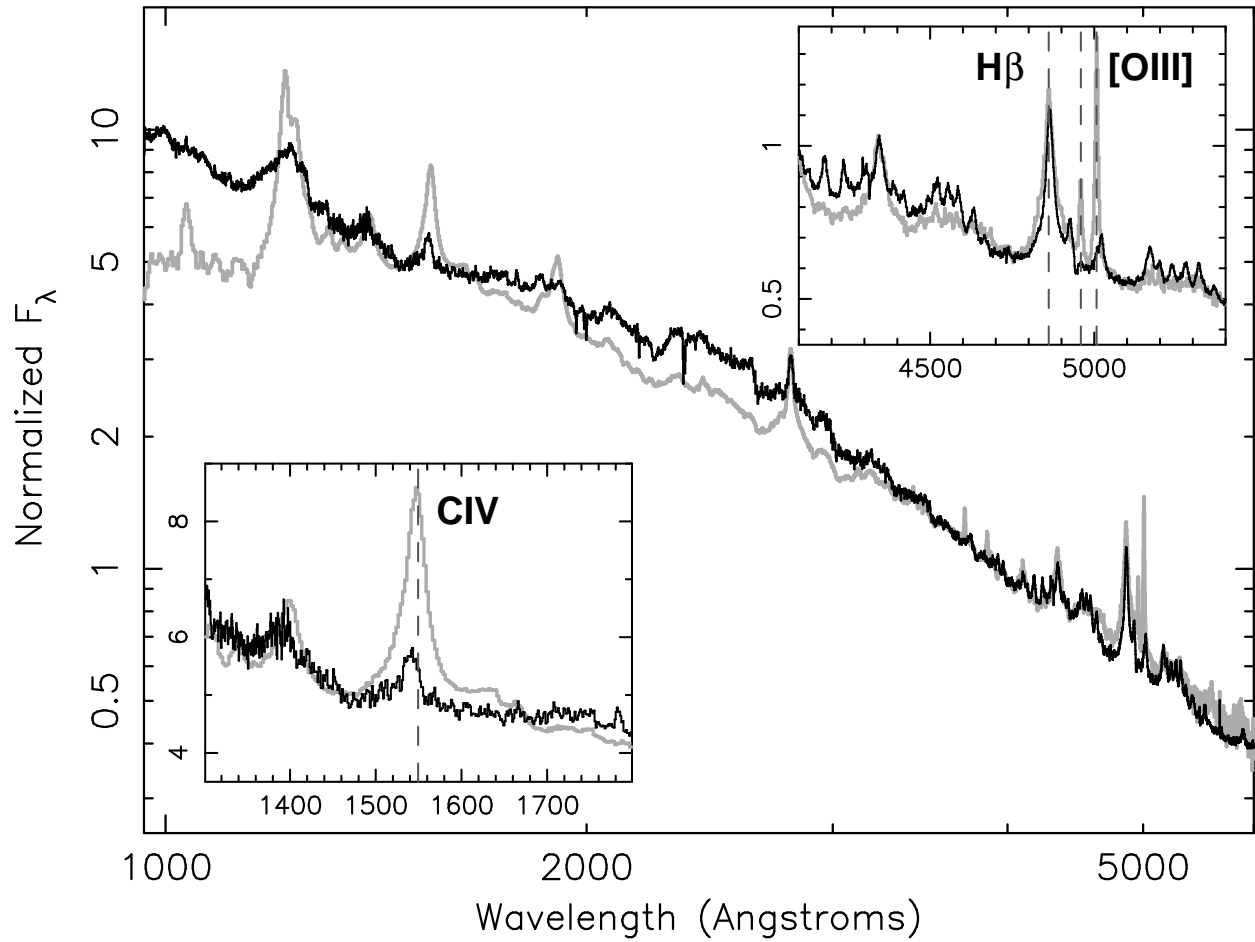


Fig. 8.— A comparison of the PHL 1811 continuum (black line) with the Large Bright Quasar Survey composite spectrum (light grey line; Francis et al. 1991). Notable features are the lack of a break in the PHL 1811 continuum toward short wavelengths in the far UV, and the large excess iron emission in the near UV. Insets show a comparison of the C IV lines and the H β region.

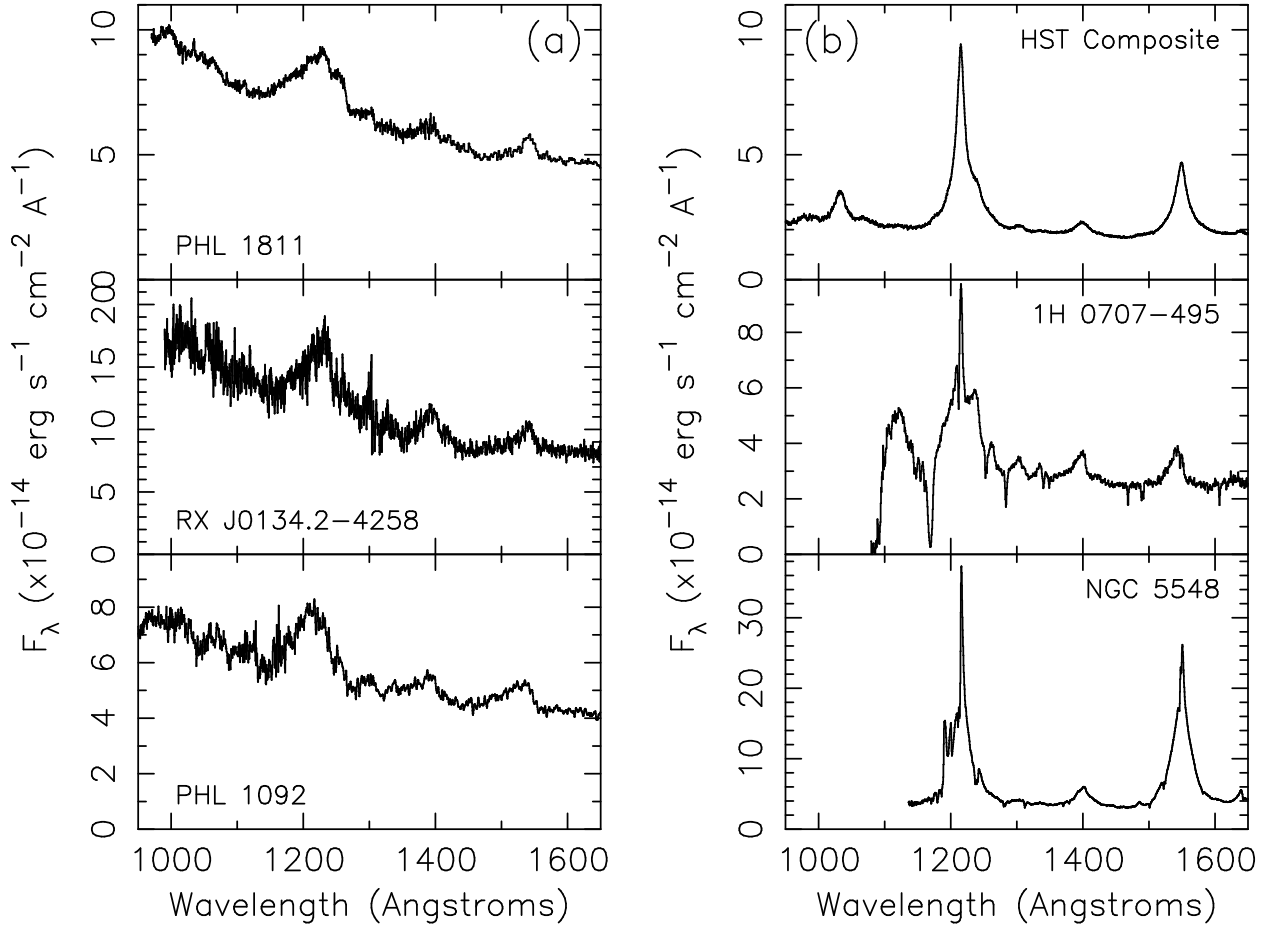


Fig. 9.— A comparison of the far UV spectra of AGN. *Left:* PHL 1811 and similar high-luminosity narrow-line quasars RX J0134.2–4258, and PHL 1092. *Right:* Comparison spectra include an *HST* composite spectrum (Zheng et al. 1997), the NLS1 1H 0707–495 (Leighly & Moore 2004; Leighly 2004), and a broad-line Seyfert 1 galaxy, NGC 5548 (Korista et al. 1995). PHL 1811 and similar objects have unusually blue spectra shortward of $\sim 1450\text{\AA}$, very weak C IV emission, and a severely blended low equivalent width Ly α /N V feature.

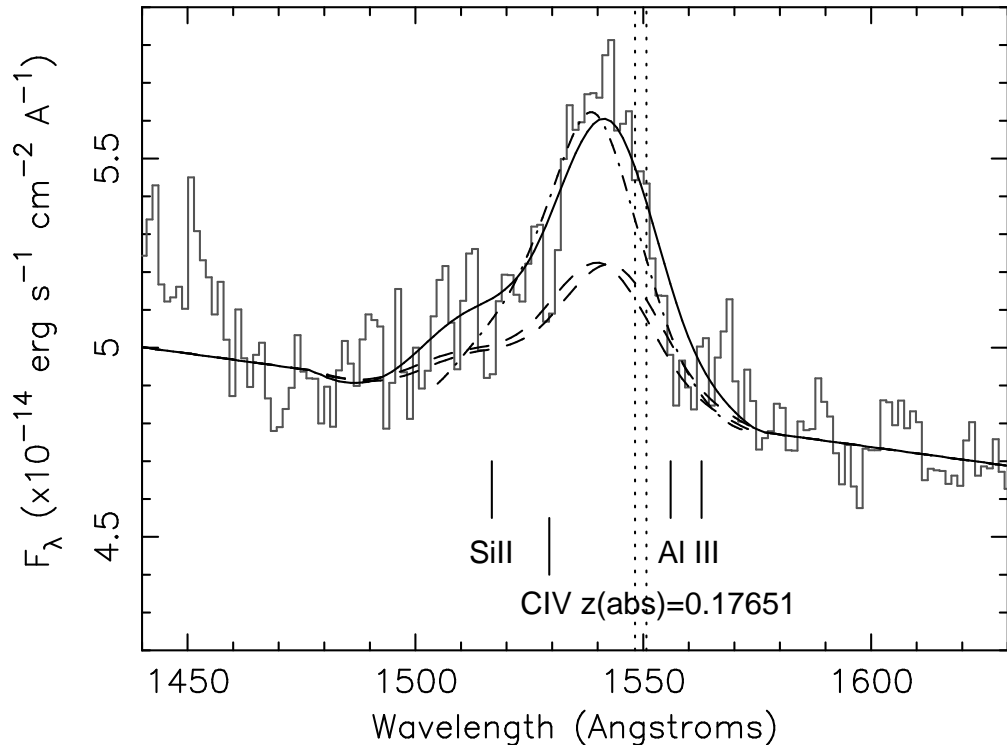


Fig. 10.— The region of the spectrum near C IV. The rest positions of the C IV doublet lines are marked by dotted lines. Also marked are the positions of plausible weak Galactic absorption lines, and an absorption line from C IV in the $z(\text{abs}) = 0.17651$ intervening system reported in Jenkins et al. (2003). The template model for the C IV profile is shown; the dashed lines show the doublet components, derived from the sum profile (solid line) using the method described in Leighly & Moore (2004). The dot-dashed line shows the template obtained for the NLS1 IRAS 13224–3809 (Leighly & Moore 2004).

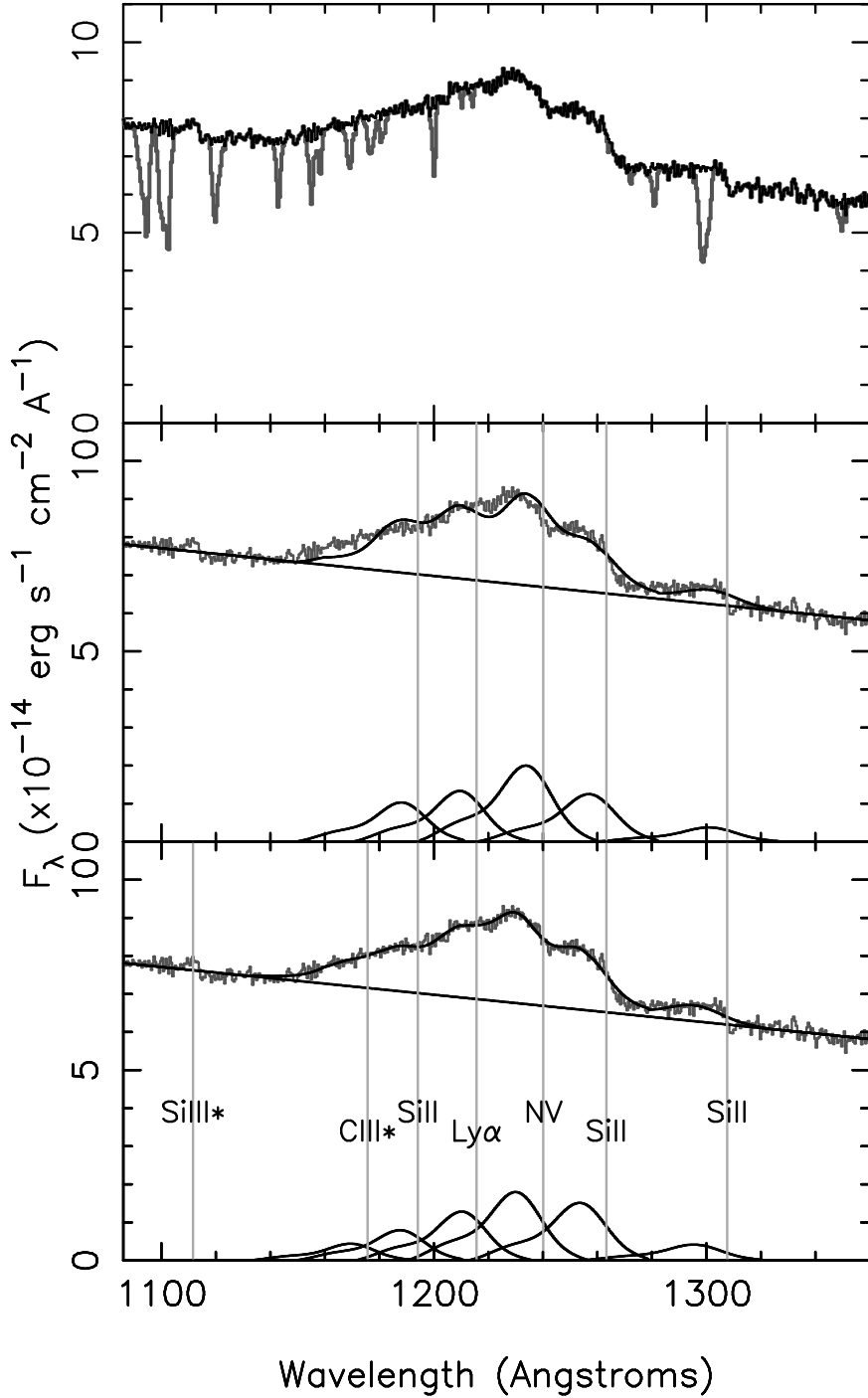


Fig. 11.— Modeling the Ly α /N V feature. *Top*: The far UV spectrum with the absorption lines (grey) modeled out. *Middle*: The fit using five templates corresponding to Ly α , N V, Si II λ 1308, Si II λ 1263, and Si II λ 1194, fixed at their rest wavelengths shown by the vertical grey lines. *Bottom*: The fit using the five templates above, and one for C III* λ 1176 as well, in which the wavelengths of the templates were free parameters. The detected metastable Si III* λ 1112 is marked as well. See §3.3.2 of the text for details.

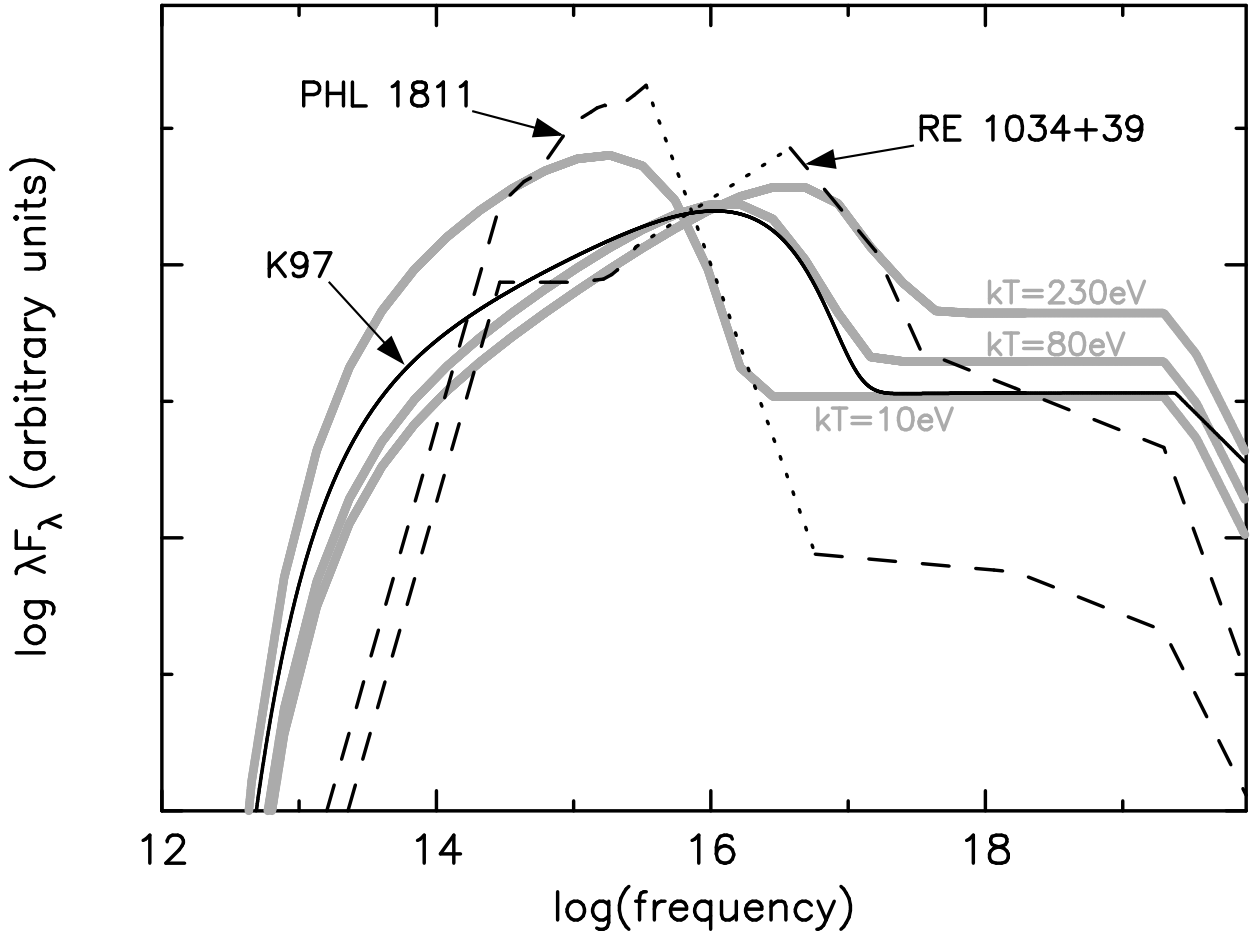


Fig. 12.— Comparison of spectral energy distributions. The dashed lines (dotted lines in the unobservable EUV) show SEDs derived from coordinated observations of PHL 1811 and the narrow-line Seyfert 1 galaxy RE 1034+39 (Casebeer, Leighly & Baron 2006). The solid black line shows the K97 continuum intended to represent the SED of a typical AGN (Korista et al. 1997). The thick grey lines show the semiempirical SEDs used for *Cloudy* simulations (Casebeer, Leighly & Baron 2006), labeled by temperature of the big-blue-bump rollover, that correspond most closely to the observed SEDs ($kT_{cut} = 10$ eV for PHL 1811 and $kT_{cut} = 230$ eV for RE 1034+39, respectively), and to the K97 SED ($kT_{cut} = 80$ eV). The SEDs used for the *Cloudy* simulations correspond reasonably well with the observed SEDs and K97 SED, at least in terms of the position of the peak of emission.

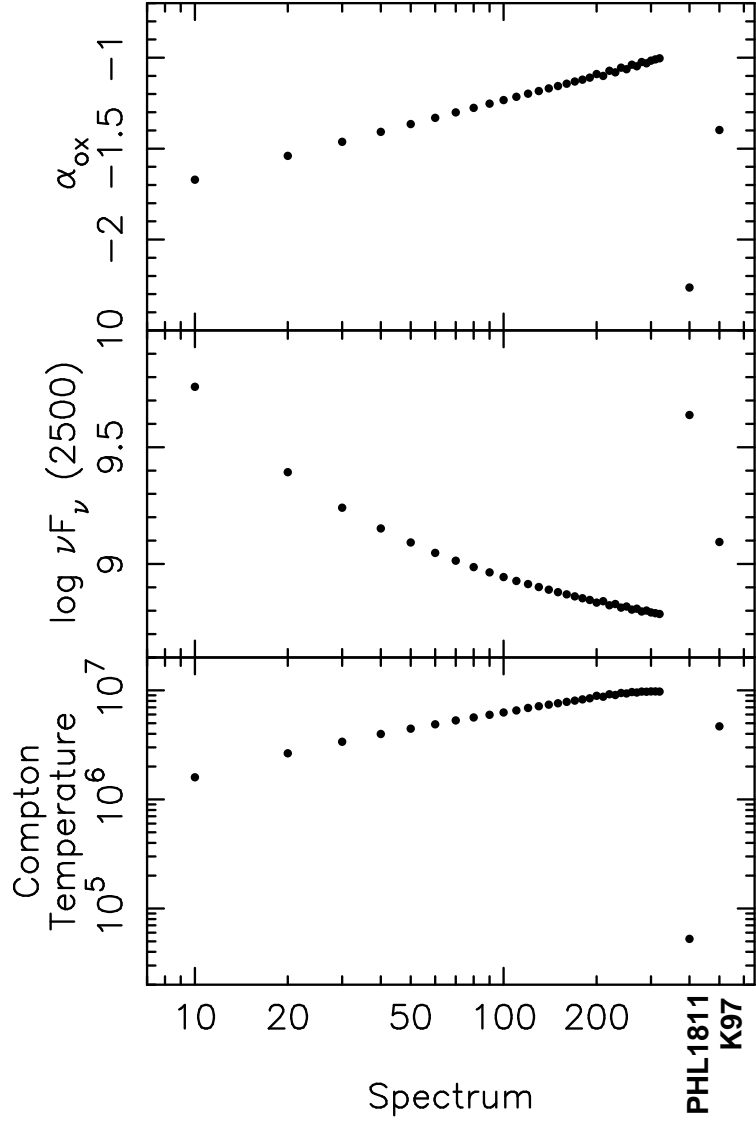


Fig. 13.— Gross properties of the SEDs used for simulations. Information for each SED is plotted as a function of the SED, where the CLB continua are coded by the big blue bump cutoff temperature (leftmost 32 points; see Casebeer, Leighly & Baron 2006, for details), and the two points on the right-hand side are for the observed PHL 1811 continuum, and the AGN continuum used by Korista et al. (1997). The top panel shows the α_{ox} , the middle panel shows the continuum flux at 2500Å for a photoionizing flux of 10^{20} photons $s^{-1} cm^{-2}$, and the lower panel shows the Compton temperature. The PHL 1811 continuum is characterized by a very steep α_{ox} , and requires a relatively bright optical and UV in order to produce the same photoionizing flux as the other continua. This will reduce the line equivalent widths. The soft spectral energy distribution produces a very low Compton temperature of around 5×10^4 K.

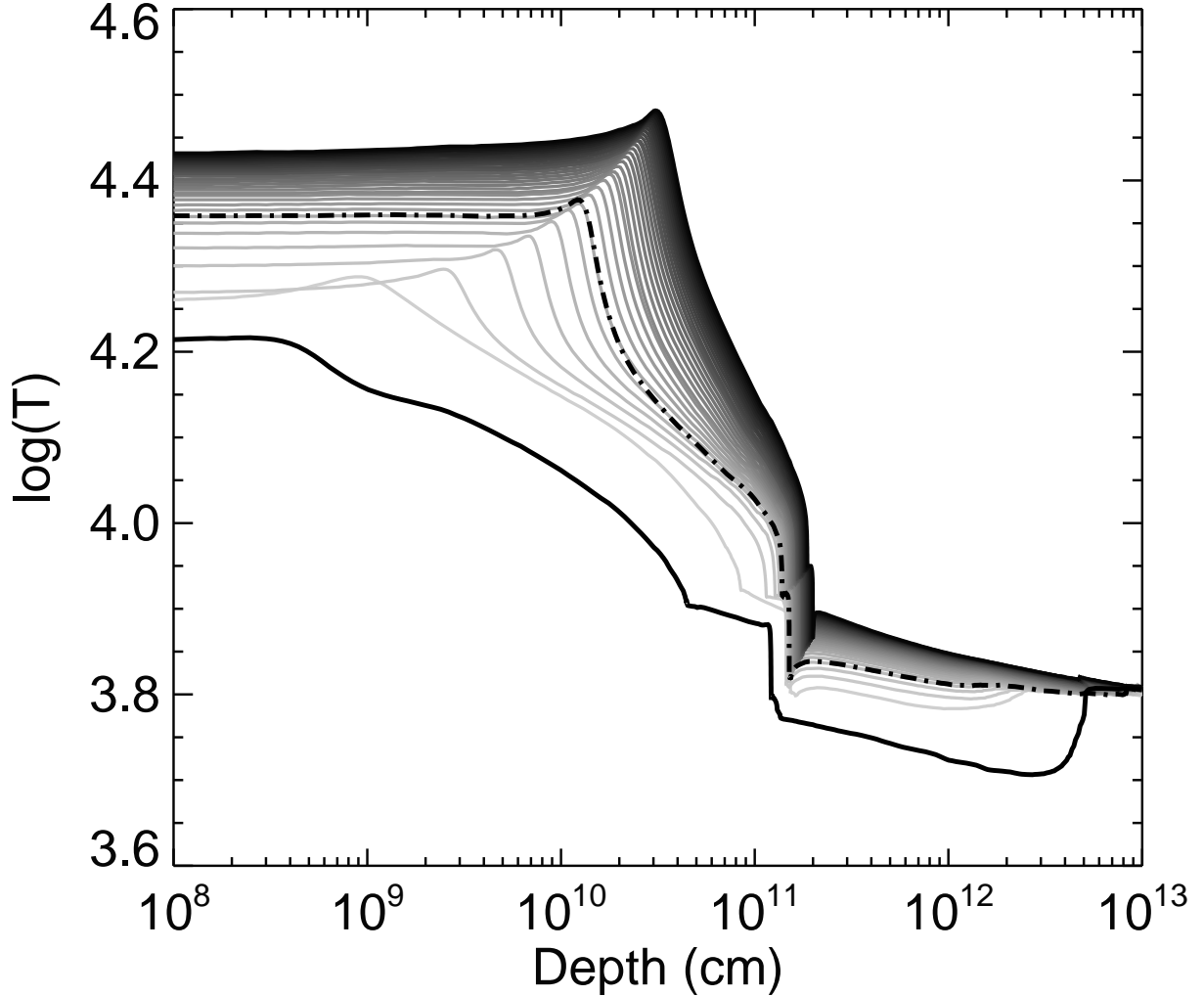


Fig. 14.— The electron temperature as a function of depth for our range of spectral energy distributions and the fiducial ionization parameter $\log U = -1.5$ and density $\log n = 11$. The thin lines show the CLB continua with light to dark showing the progression of soft SEDS ($kT_{cut} = 10$ eV) to hard ones ($kT_{cut} = 320$ eV). The solid thick line and the dash-dot line shows the result for the PHL 1811 continuum and the K97 continuum, respectively. The electron temperature is lower for the PHL 1811 continuum than any other continuum.

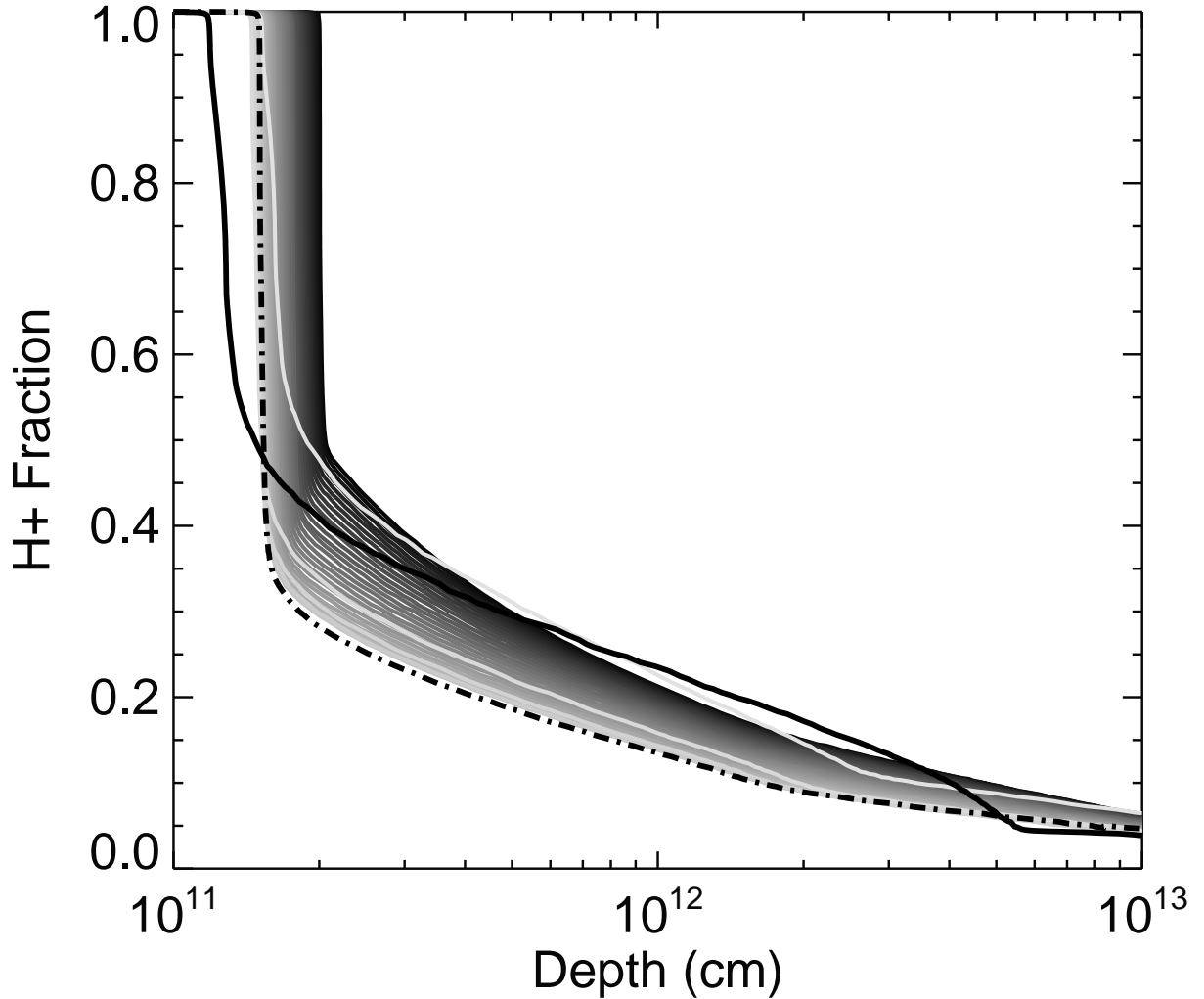


Fig. 15.— The hydrogen ionization fraction in the vicinity of the hydrogen ionization front and into the partially-ionized zone for the range of spectral energy distributions and the fiducial ionization parameter $\log U = -1.5$ and density $\log n = 11.0$. The lines have the same meaning as in Fig. 14. For the CLB continua, the fraction of ionized hydrogen at a particular depth decreases as the continuum becomes softer (kT_{cut} decreases), but then increases again for the softest continua. Likewise, the hydrogen ionization fraction is higher for the PHL 1811 continua. The resulting total ionized hydrogen column is 25% greater for the PHL 1811 continuum than for the K97 continuum.

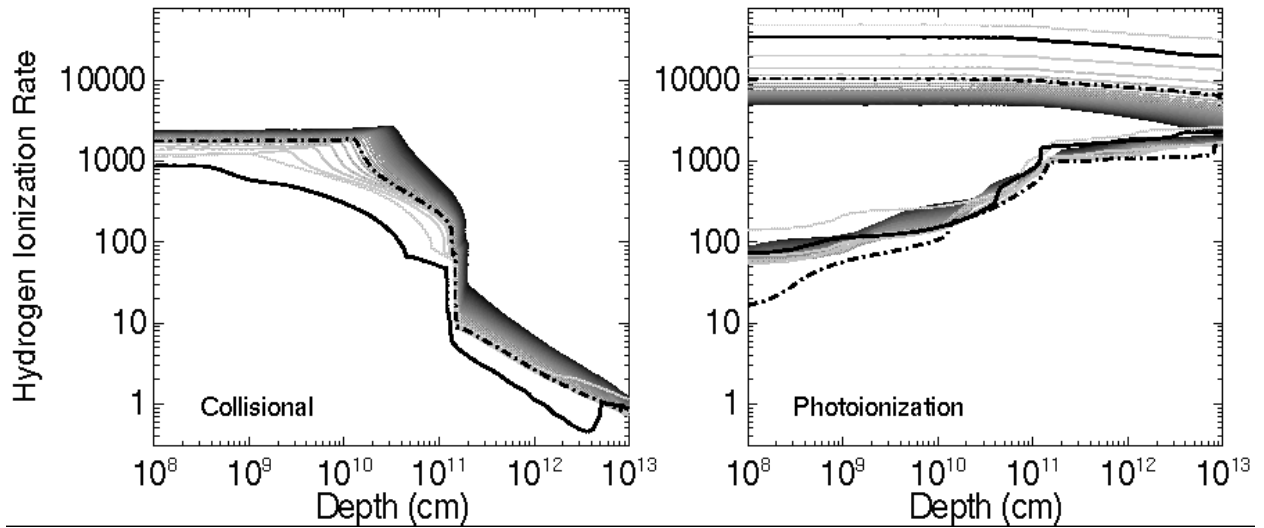


Fig. 16.— The rate of ionization of hydrogen from $n = 2$ from collisional ionization (left panel) and photoionization (right panel). The upper group of lines in the photoionization plot shows the rate from the direct continuum, and the lower group of lines shows the rate from the diffuse emission. The lines and shading have the same meaning as in Fig. 14. The rates are dominated by photoionization from the direct continuum, and are very large for PHL 1811 and other soft SEDs.

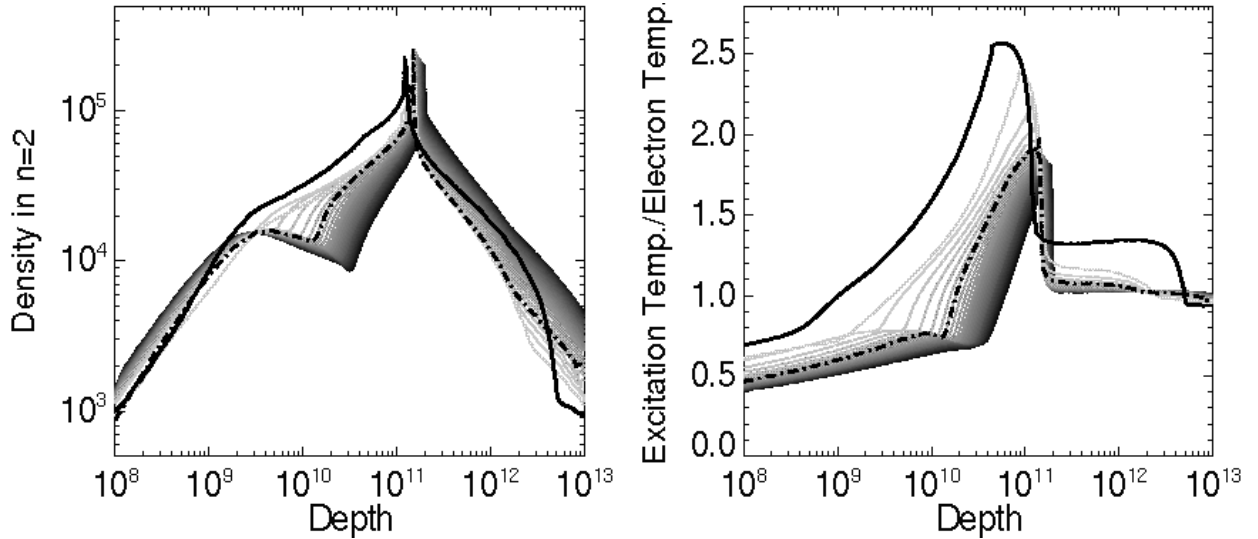


Fig. 17.— *Left*: The density of hydrogen in $n = 2$ as a function of depth for the fiducial parameters ($\log U = -1.5$ and $\log n = 11$). The lines have the same meaning as in Fig. 14. In the partially ionized zone, the density of excited hydrogen is larger in gas illuminated by hard SEDs than in gas illuminated by soft SEDs, but recovers for PHL 1811. *Right*: The ratio of the excitation temperature to the electron temperature for the fiducial parameters. The ratio is near one for the hard SEDs, implying that the number of hydrogen in $n = 2$ are consistent with that expected from the electron temperature of the gas, and therefore the excitation mechanism is collisions. In contrast, the excitation of PHL 1811 is higher than predicted by the rather low temperature.

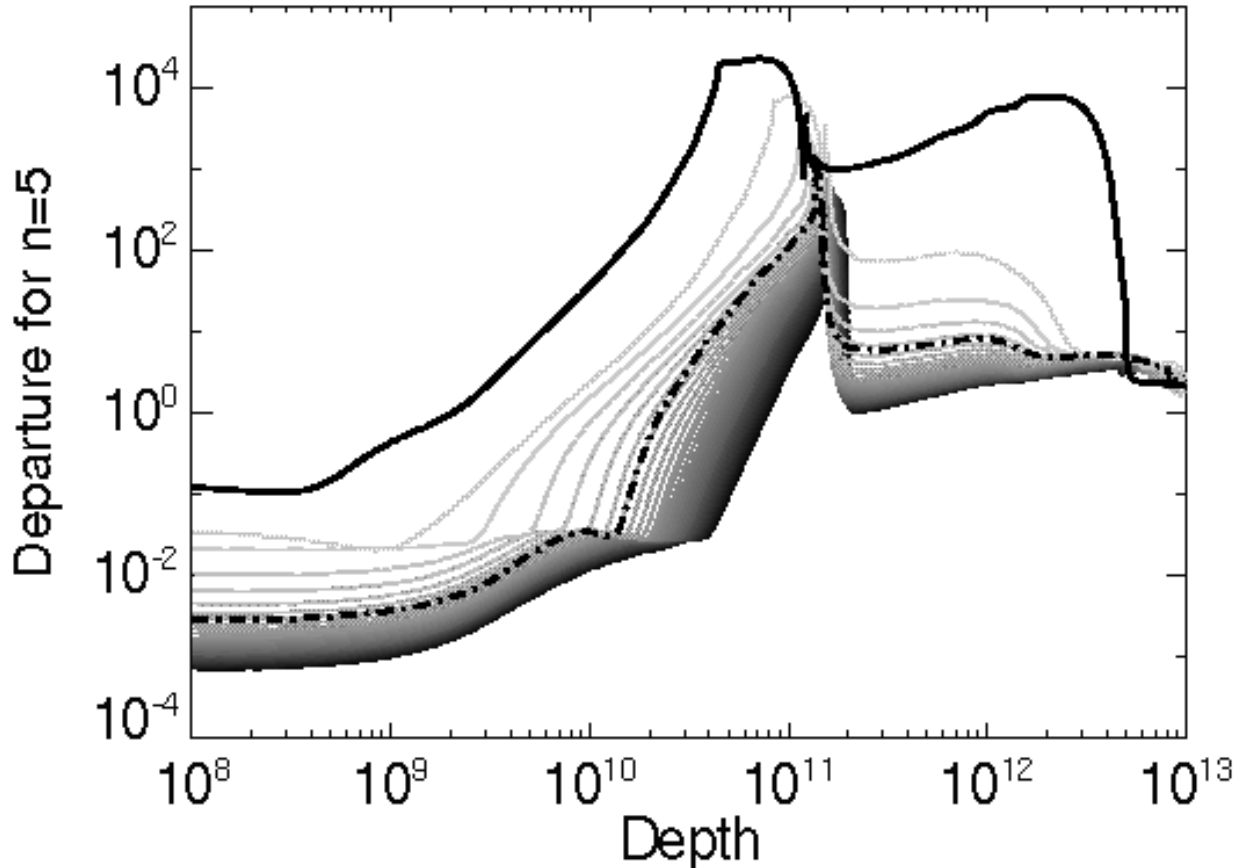


Fig. 18.— The ratio of the density of hydrogen in $n = 5$ from the *Cloudy* output to the density expected based on the density in $n = 1$ and the electron temperature for the fiducial gas parameters ($\log U = -1.5$ and $\log n = 11$); this parameter is proportional to the departure coefficient for $n = 5$. The lines have the same meaning as in Fig. 14. The departure coefficient is very large for PHL 1811.

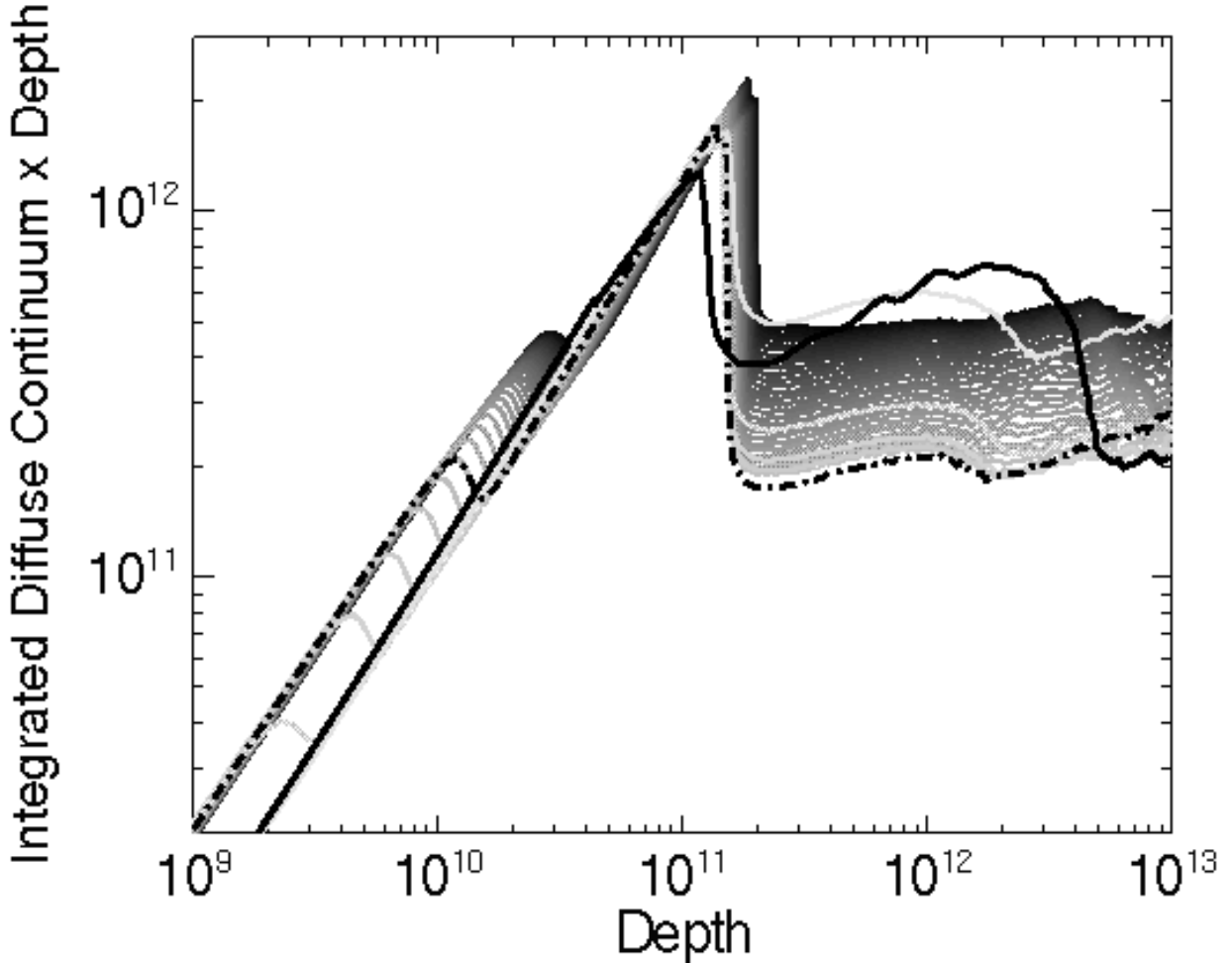


Fig. 19.— Integrated diffuse continuum times the depth (in $\text{erg s}^{-1} \text{cm}^{-1}$) as a function of depth for the fiducial parameters ($\log U = -1.5$ and $\log n = 11$). The lines have the same meaning as in Fig. 14. The energy in the diffuse continuum is greater in gas illuminated by the hard continuum compared with the gas illuminated by the softer continua, but is even higher in PHL 1811. The energy in the continuum is large in objects with hard SEDs because of the greater amount of energy injected into that region by the soft X-ray photoionization. The energy in the continuum is large in PHL 1811 because the gas is so cool that usual channels of cooling (e.g., excitation of metal ions) are less important, and the gas has no options besides emission of continuum. The gas illuminated by the hard continuum resembles gas with a high density in that cooling options are limited.

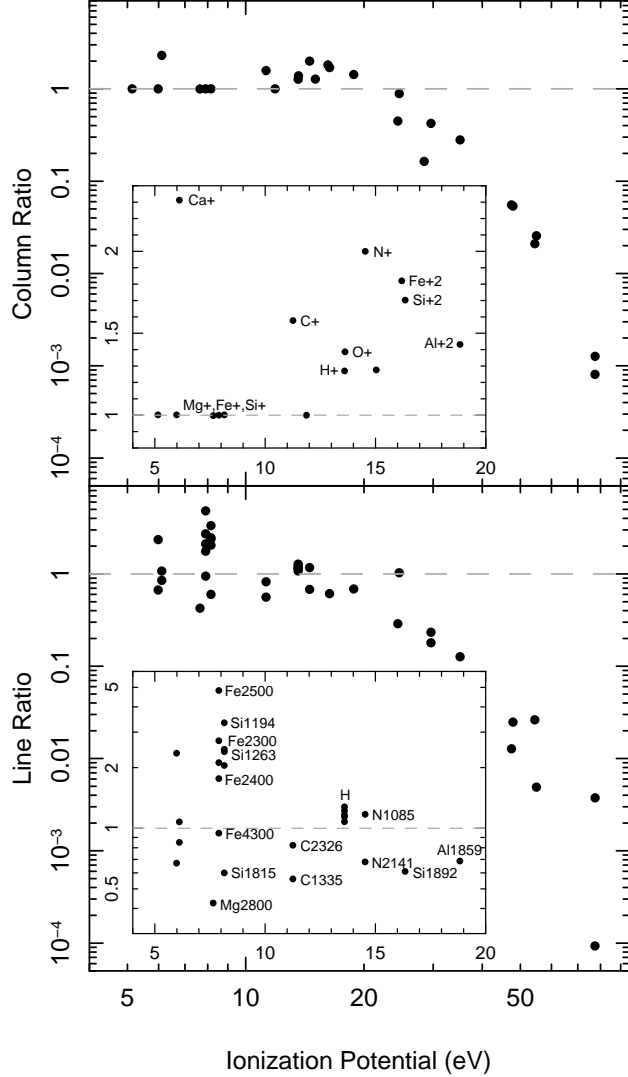


Fig. 20.— A comparison of the predicted ion and emission-line properties for the PHL 1811 continuum and the K97 continuum for the fiducial gas parameters ($\log U = -1.5$ and $\log n = 11.0$). In both cases, the column density is $10^{24.5}$, which is sufficiently large to be very optically thick to the hydrogen continuum. The embedded small panels show the same information as the larger panels on an expanded scale. The top plot shows the ratio of the predicted ion columns for PHL 1811 to K97 as a function of the ionization potential. For the lowest ionization potentials, the columns are nearly the same. For the highest ionization potentials, the column is much lower for PHL 1811 continuum, as it is too soft to create or excite highly-ionized ions. Intermediate-ionization ions fill the region above the hydrogen ionization front, and thus their levels are elevated in PHL 1811. The bottom panel shows the ratio of resulting common emission lines. The dispersion for a lines emitted by a particular ion arises from the fact that lines that are collisionally excited are generally weaker for PHL 1811 because the temperature is lower, whereas lines that are excited by continuum fluorescence are brighter because the UV continuum is relatively brighter for the same ionization parameter and density in PHL 1811 compared with K97.

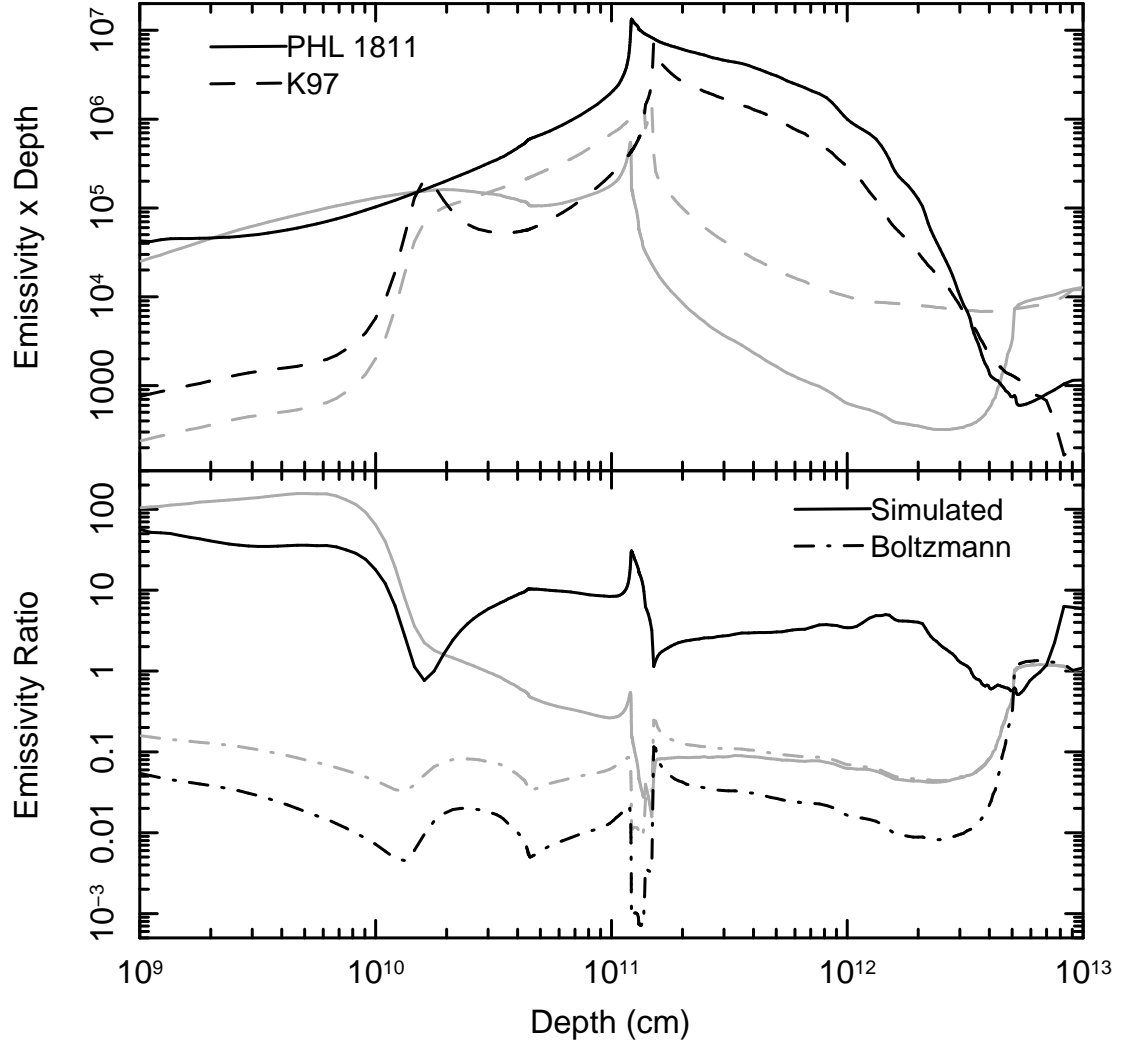


Fig. 21.— A comparison of the line emissivity and ratios for the PHL 1811 continuum and the K97 continuum for Si II $\lambda 1814$ (grey lines) and Si II $\lambda 1194$ (black lines). The top panel shows the line emissivity multiplied by the depth as a function of the depth. For the 1814\AA line, the emissivity of PHL 1811 is smaller than that of K97 particularly in the partially-ionized zone where Si^+ dominates (depths $>\sim 10^{11}$ cm). In contrast, the emissivity of the 1194\AA line is much higher for PHL 1811. The lower panel shows the ratios from the gas illuminated by the PHL 1811 continuum to that of the gas illuminated by the K97 continuum. The solid lines show the ratios computed from the *Cloudy* predictions of the line emissivity as a function of depth, while the dashed lines show the ratios computed using the electron temperatures and the Boltzmann excitation equation. The two ratios match well for the collisionally-excited line at 1814\AA ; deviations at low depths are a consequence of different fractional abundances of Si^+ ions. But the observed ratio is much larger than the Boltzmann equation ratio for the 1194\AA line. This is because the 1194\AA line is predominately excited by continuum fluorescence, and much brighter in PHL 1811 due to its relatively brighter UV continuum for the same ionization parameter and density.

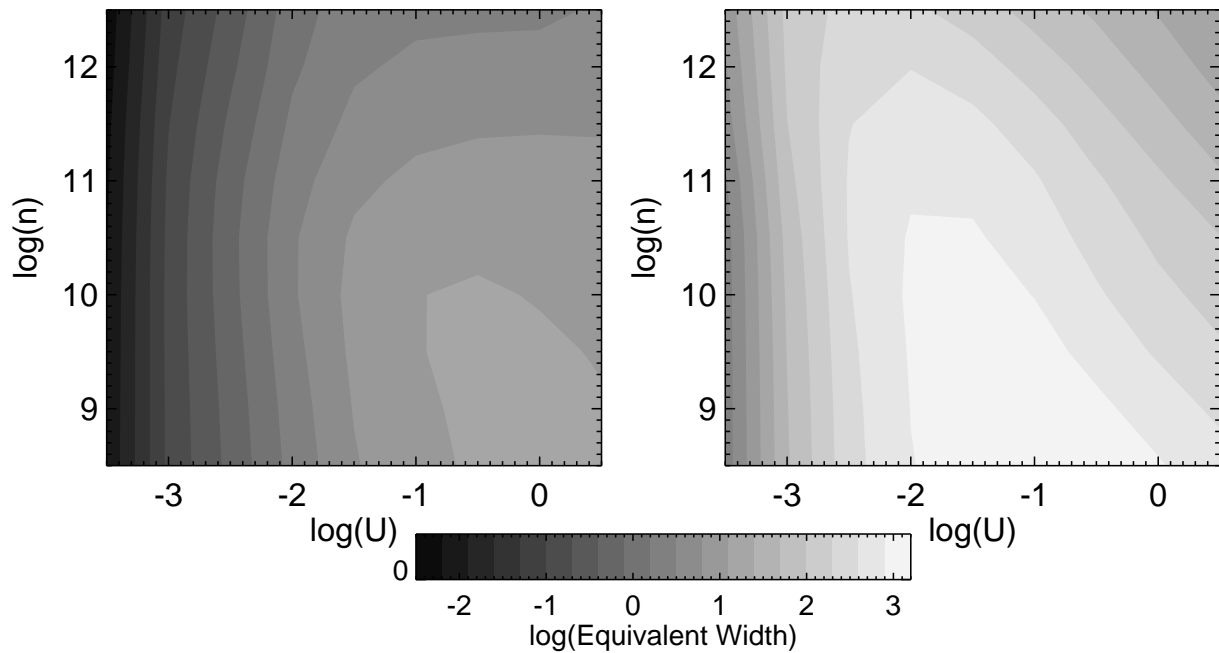


Fig. 22.— A comparison of the line equivalent widths of C IV for the PHL 1811 continuum (left) and the K97 continuum (right) as a function of ionization parameter and density. C IV is predicted to be weak in PHL 1811 because of the low column of C^{+3} ions and the lower temperature in the emitting gas of this collisionally excited line.

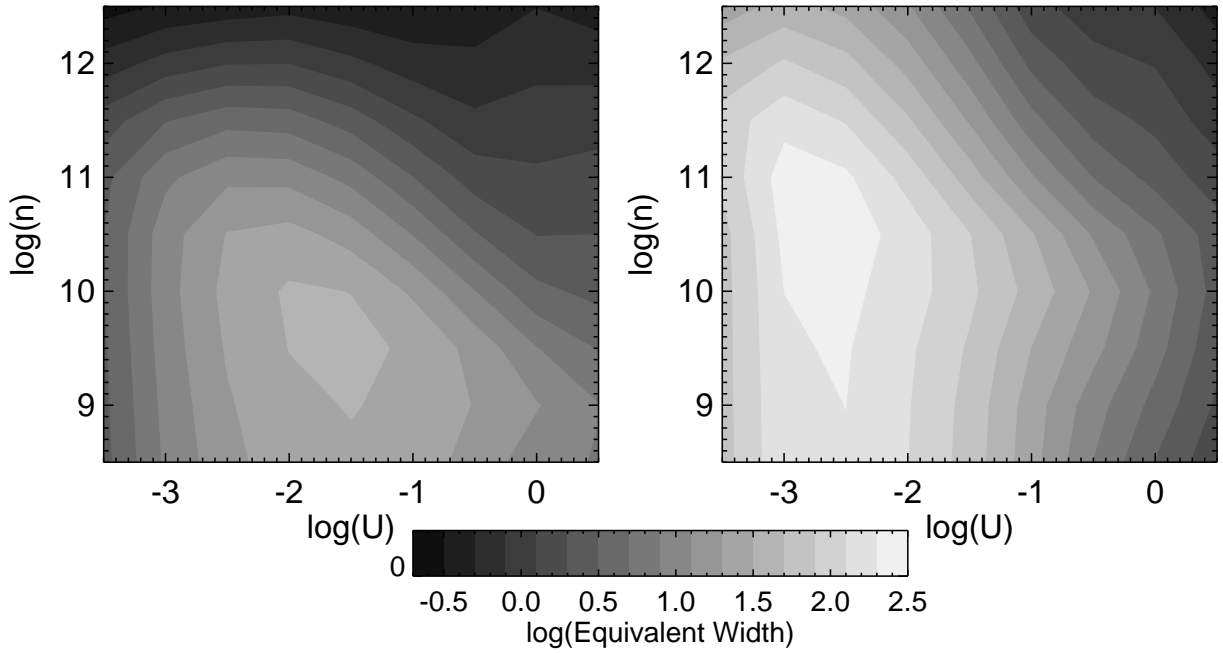


Fig. 23.— A comparison of the line equivalent widths of Si III] for the PHL 1811 continuum (left) and the K97 continuum (right) as a function of ionization parameter and density. This semiforbidden line has a critical density of $3 \times 10^{11} \text{ cm}^{-3}$, so a decline toward higher densities in the K97 simulation is expected. In contrast, in the PHL 1811 continuum simulations, the onset of the decline toward higher densities occurs at much lower densities, around 10^{10} cm^{-3} . This implies that for gas illuminated by soft continua, the usual density indicators are not reliable.

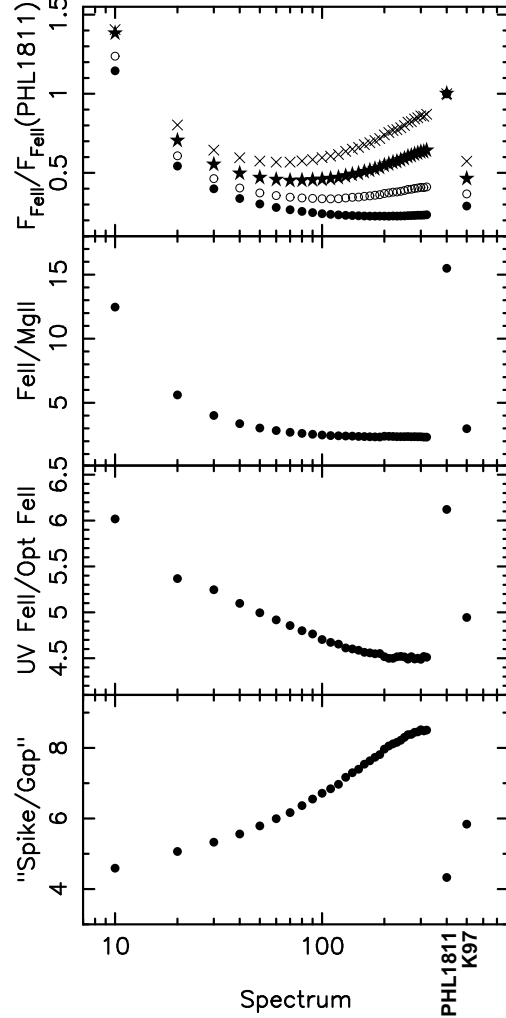


Fig. 24.— Properties of Fe II using the *Cloudy* 371-level atom for the fiducial parameter ($\log U = -1.5$ and $\log n = 11$). *Top*: The ratio of the Fe II emission in broad bands for the range of spectral energy distributions compared to that of PHL 1811. Solid circles: 1000–2000Å, solid stars: 2000–3000Å, \times 's: 4000–6000Å, open circles: 7800Å–3 microns. *Second from top*: Ratio of Fe II flux in the 2200–3050Å band to the Mg II flux. The large ratio for PHL 1811 is a combination of higher Fe II flux, a consequence of stronger continuum pumping, and lower Mg II flux, a consequence of lower electron temperature. *Third from the top*: The ratio of the Fe II emission in the UV (2000–3000Å) to the Fe II emission in the optical (4000–6000Å). This ratio is high in PHL 1811 because the continuum pumping enhances the UV emission, and because of Fe II emission in the H^+ –neutral He region. *Bottom*: The “spike/gap” ratio, defined by Baldwin et al. (2004). This ratio is essentially the emission from the low-lying, collisionally-excited levels that produce the spikes, to the emission from high levels. The high-level emission is enhanced in PHL 1811 due to continuum pumping.

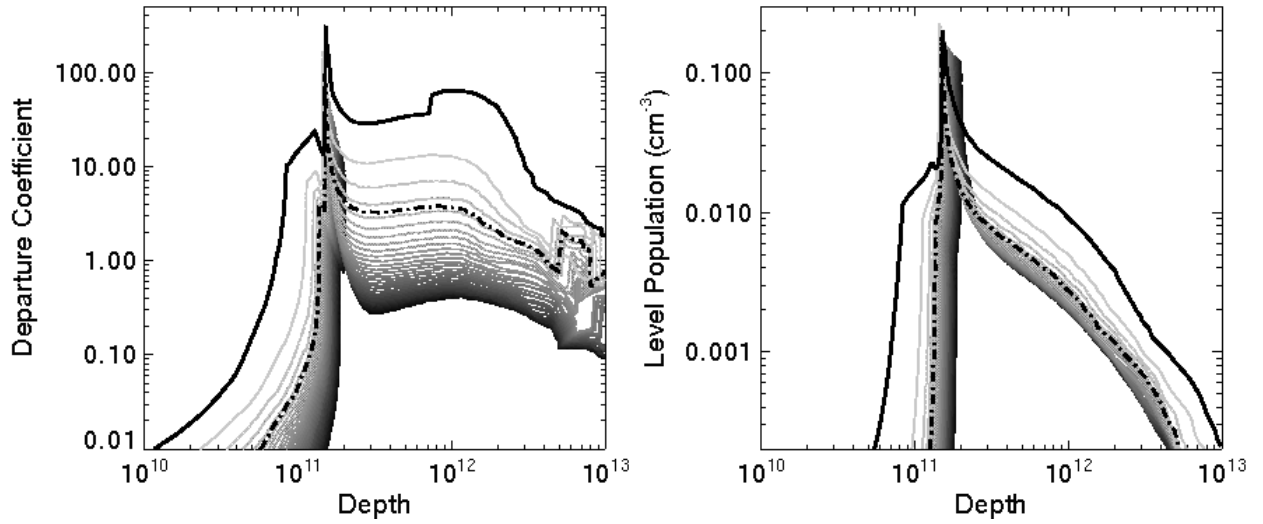


Fig. 25.— Properties of level number 295 (10.85 eV) as a function of depth for a range of spectral energy distributions for the fiducial parameters ($\log U = -1.5$, $\log n = 11$, and $\log N_H = 24.5$). The lines have the same meaning as in Fig. 14. *Left:* The departure coefficient shows that level 295 is much more highly populated (by a factor of almost 100 in the partially-ionized zone) in the gas illuminated by the PHL 1811 spectral energy distribution than expected from the local electron temperature. *Right:* The density of Fe^+ ions in level 295 shows that the departure coefficient is high for gas in PHL 1811 both because the temperature is low (Fig. 14) and because the number of atoms with electrons in this level is high.

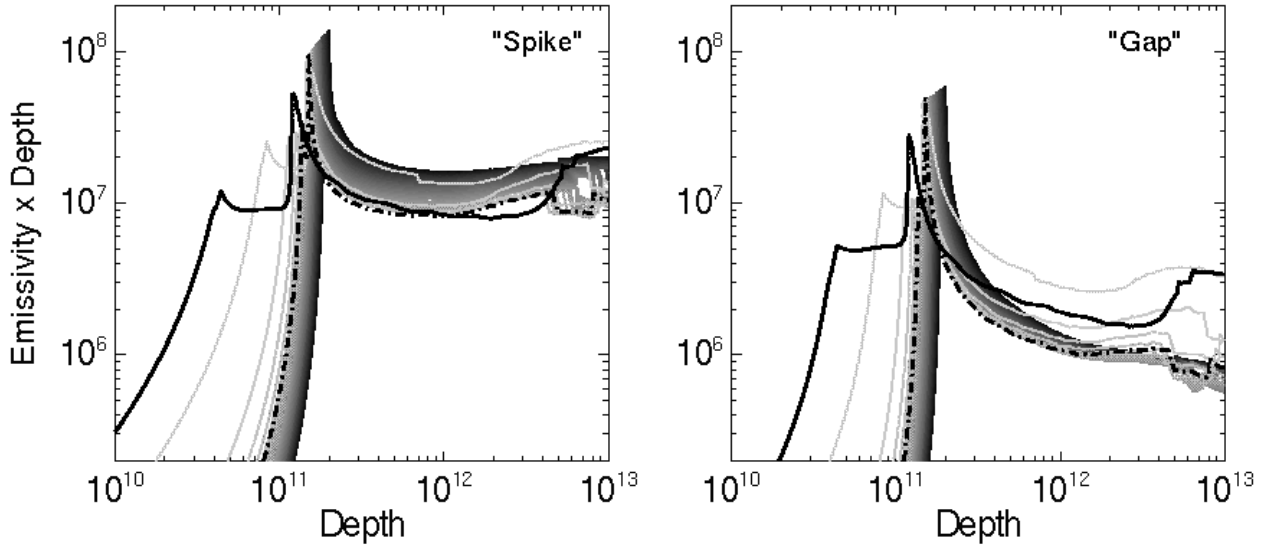


Fig. 26.— The emissivity times depth as a function of depth for two regions of the Fe II spectrum for the fiducial parameters ($\log U = -1.5$, $\log n = 11$, and $\log N_H = 24.5$). The lines have the same meaning as in Fig. 14. Note that the emissivity has the opacity factored in; the value is the amount reaching the surface. The left side shows the “spike” region of the spectrum (2312–2328 and 2565–2665 Å) and the right side shows the “gap” region (2462–2530 Å; Baldwin et al. 2004). In both cases, the “hook” between $\sim 3 \times 10^{10}$ and $\sim 10^{11}$ cm for PHL 1811 originates in the H^+ -neutral He region. The spike is predominately resonance transitions, and the emission in the partially-ionized zone is approximately proportional to the temperature of the gas (although somewhat elevated for the softest continua). The gap is predominately emission from higher levels; these levels are pumped by the continuum and Ly α when the SED is soft, and they are higher in the partially-ionized zone.

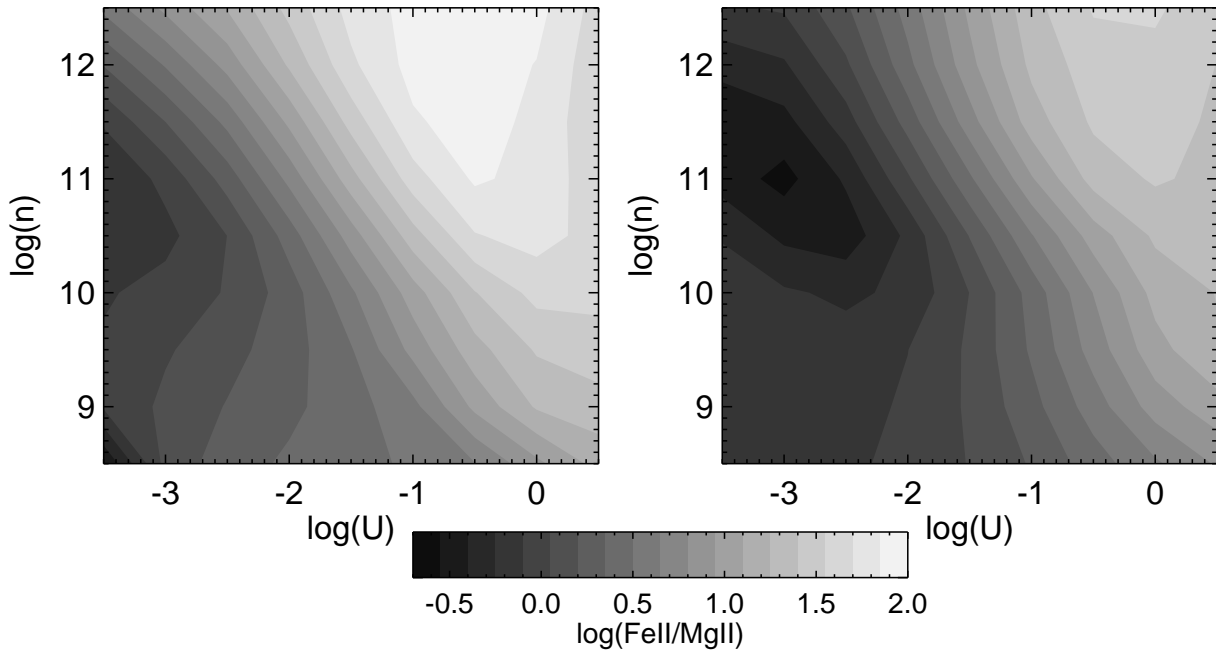


Fig. 27.— The log of the ratio of the Fe II emission in 2200-3050Å band to the Mg II emission as a function of ionization parameter and density. In each case, the column density is proportional to the ionization parameter such that $\log N_H + \log U = 26$. The ratio is consistently higher for PHL 1811 (left) compared with the K97 continuum (right).

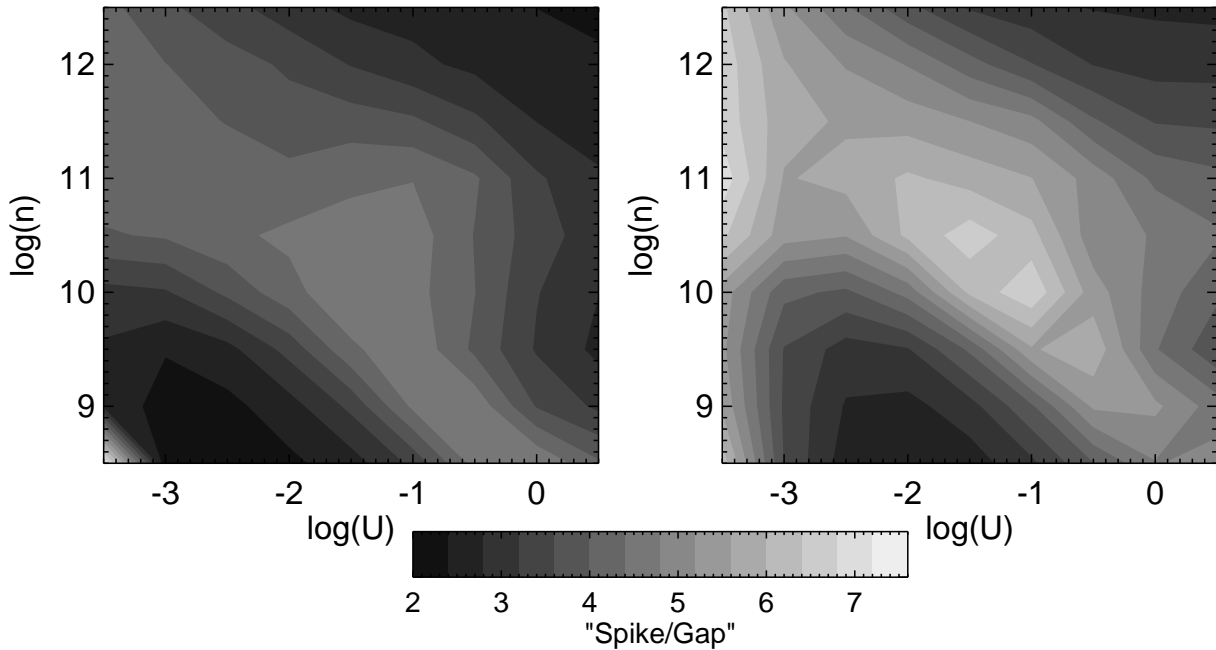


Fig. 28.— The “spike/gap” ratio for the PHL 1811 (left) and K97 (right) SEDs as a function of ionization parameter and density. The ratio for the PHL 1811 continuum is consistently lower than for the K97 continuum, although still much larger than the observed value (0.7; Baldwin et al. 2004). As discussed in the text, the lower ratio originates from higher emission from high levels that comprise the “gap” emission in gas illuminated by the PHL 1811 continuum.

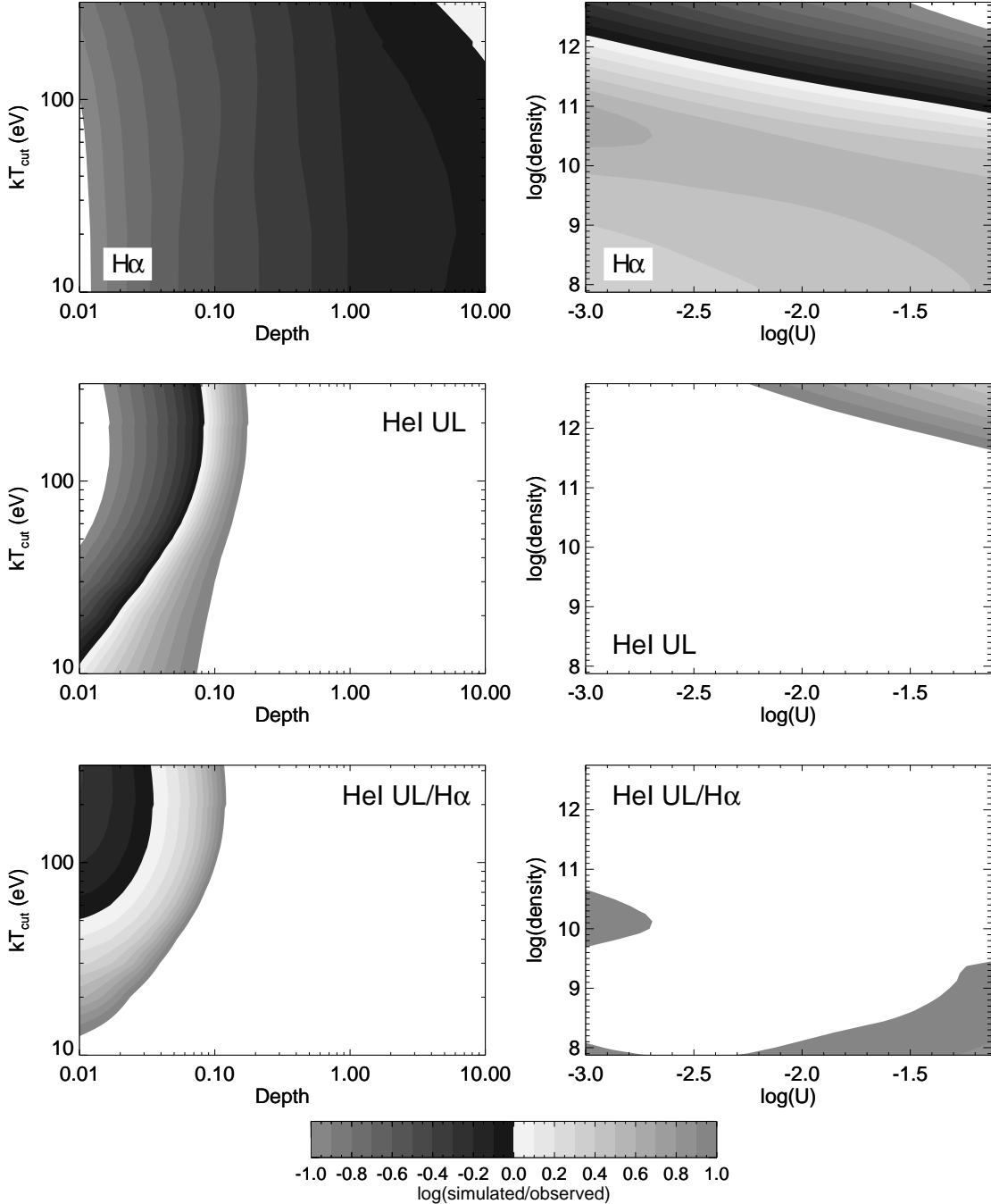


Fig. 29.— Contours for *Cloudy* simulations of $H\alpha$, the upper limit for $He\ I\ \lambda 5875$, and their ratio. Only regions in which the log of the ratio of the simulated to observed is between -1 and 1 (i.e., 1 dex from a perfect match) are shaded. Four parameters (kT_{cut} , D , $\log(density)$ and $\log(U)$) define the parameter space of the simulations, where D is ratio of the depth to the depth of the hydrogen ionization front. Shown are contours in planes defined by two of the four parameters: kT_{cut} and D on the left side, and $\log(density)$ and $\log(U)$ on the right side. These planes intersect at the point $kT_{cut} = 10$, $\log(density) = 11.5$, $\log(U) = -2.0$, and $D = 10$.

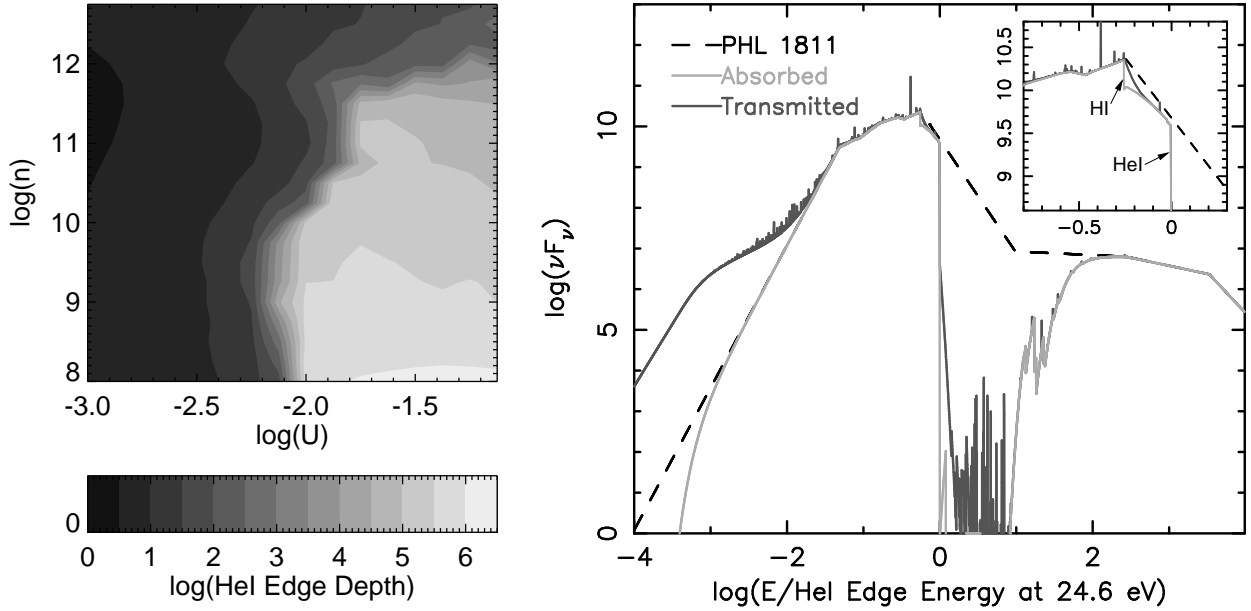


Fig. 30.— Results from *Cloudy* simulations in which the column density is chosen to maximize the ratio of the He^+ and H^+ columns. *Left:* The log of the ratio of the transmitted continuum just below the He I edge (23.9 eV) to the transmitted continuum just below the N II edge (28.8 eV). A plateau exists upon which the He I edge is very prominent in the transmitted spectrum. *Right:* A representative example continuum for $\log(U) = -1.5$ and $\log(n) = 11.5$. The dashed black line shows the PHL 1811 continuum. The light grey line shows the continuum after it is absorbed by the gas. The dark grey line shows the absorbed plus diffuse continuum, or the transmitted continuum. The inset shows a magnified view of the region around the Lyman and He I edges. The diffuse continuum fills in the Lyman edge.

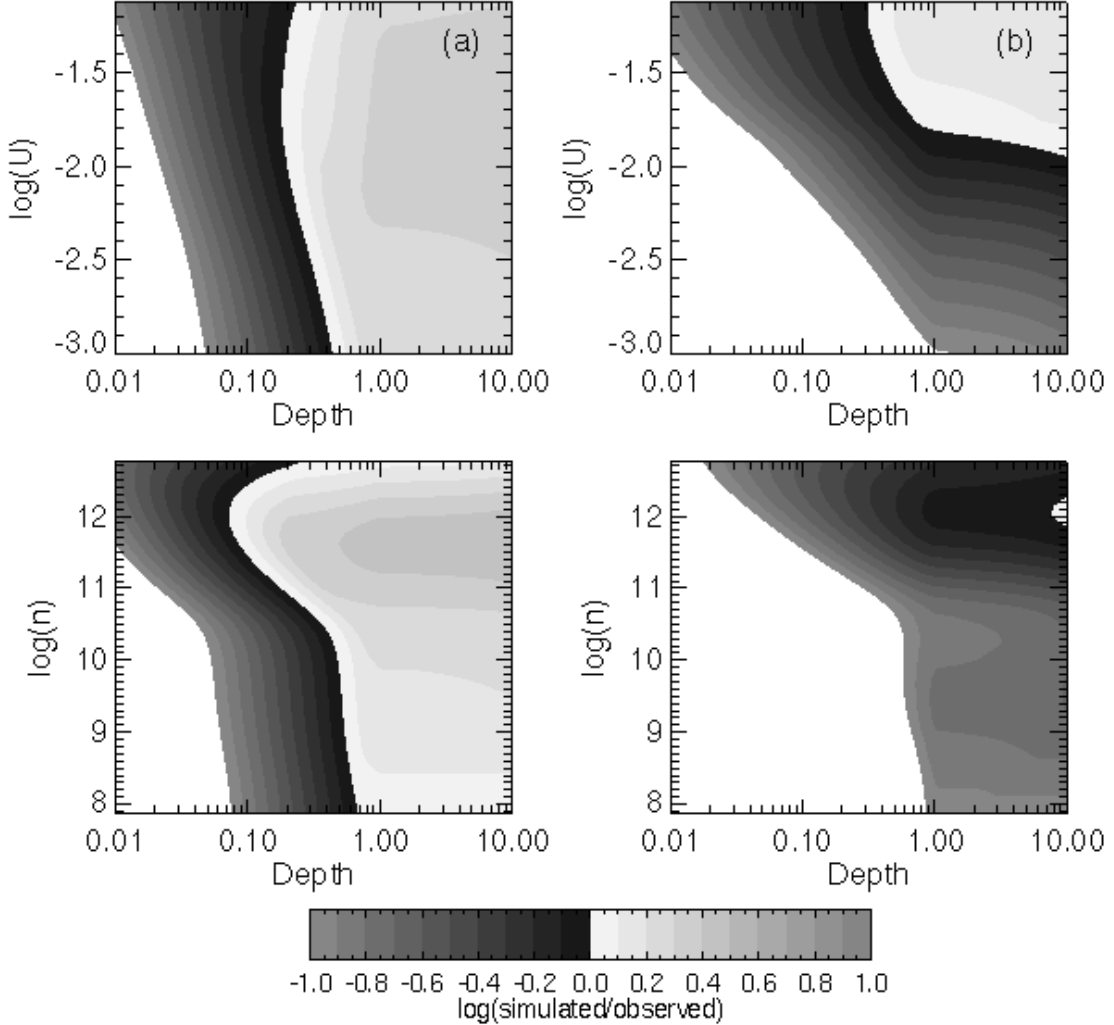


Fig. 31.— The results of filtering the continuum on the He I $\lambda 5786$ emission for the case of the PHL 1811 continuum. The left column, labeled (a.), shows the He I emission with respect to the upper limit when the emitting gas is illuminated directly by the continuum (no filtering). A covering fraction of 10% is assumed. Except for low column densities, the predicted He I exceeds the upper limit by a large factor. The right column, labeled (b.), shows the He I emission with respect to the upper limit when the emitted gas is illuminated by the transmitted continuum shown in Fig. 30 (the filtered continuum). The predicted He I emission is lower than the upper limit for low to moderate ionization parameters. In both columns, the top panel shows the case where $\log(n) = 10.5$, and the bottom panel shows the case where $\log(U) = -2.75$. Note that the ionization parameter shown is the one appropriate for the unfiltered continuum in both cases.

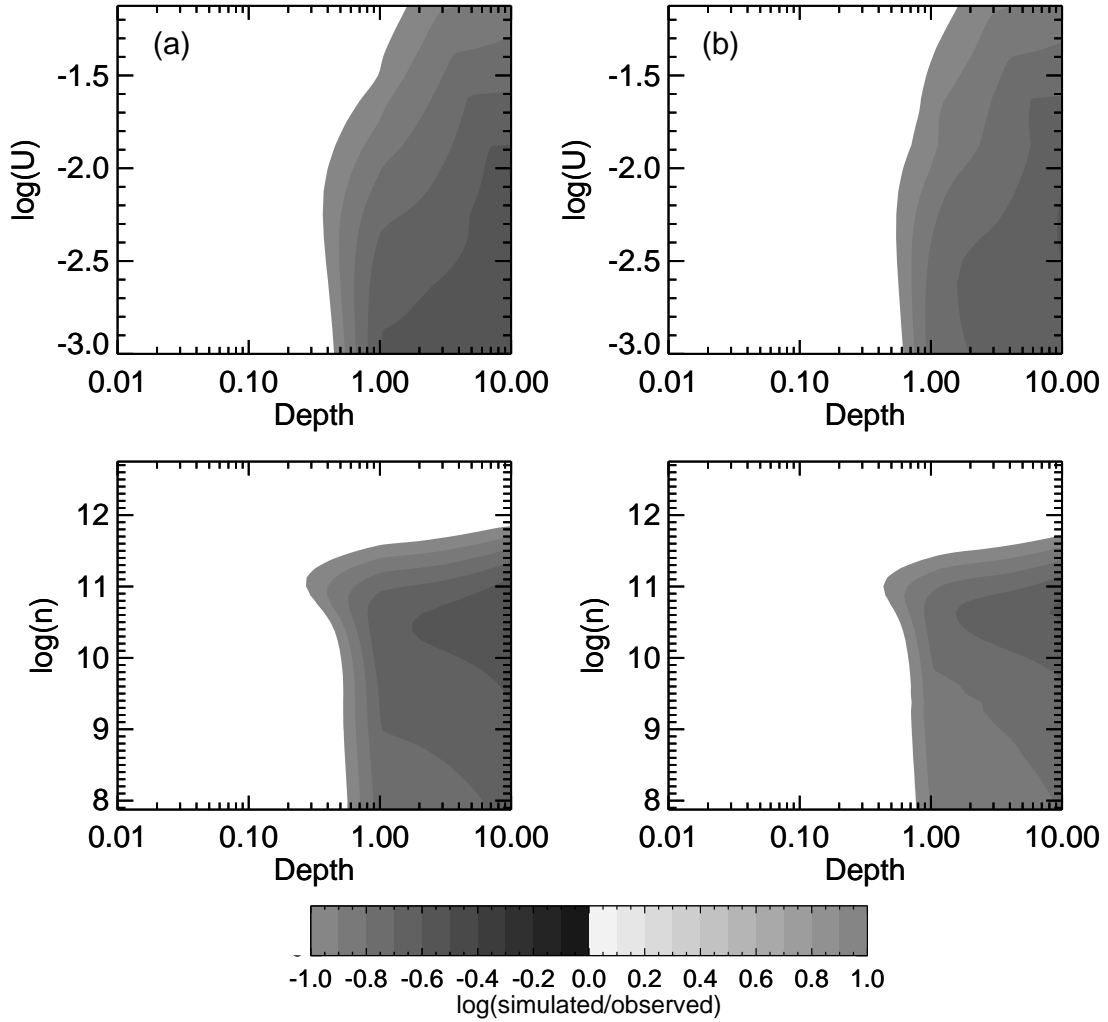


Fig. 32.— The corresponding results of filtering the continuum on the $\text{H}\alpha$ emission for the same case as shown in Fig. 31. In both columns, the top panel shows the case where $\log(n) = 10.5$, and the bottom panel shows the case where $\log(U) = -2.75$. Again, a covering fraction of 10% is assumed. Note that the ionization parameter shown is the one appropriate for the unfiltered continuum in both cases. There is little difference between the non-filtered case (left) and the filtered case (right). This is expected because the Lyman continuum is not much altered by the transmission, as shown in Fig. 30. $\text{H}\alpha$ is in the vicinity of the observed value (although lower by a factor of two) at high column densities and moderate densities.

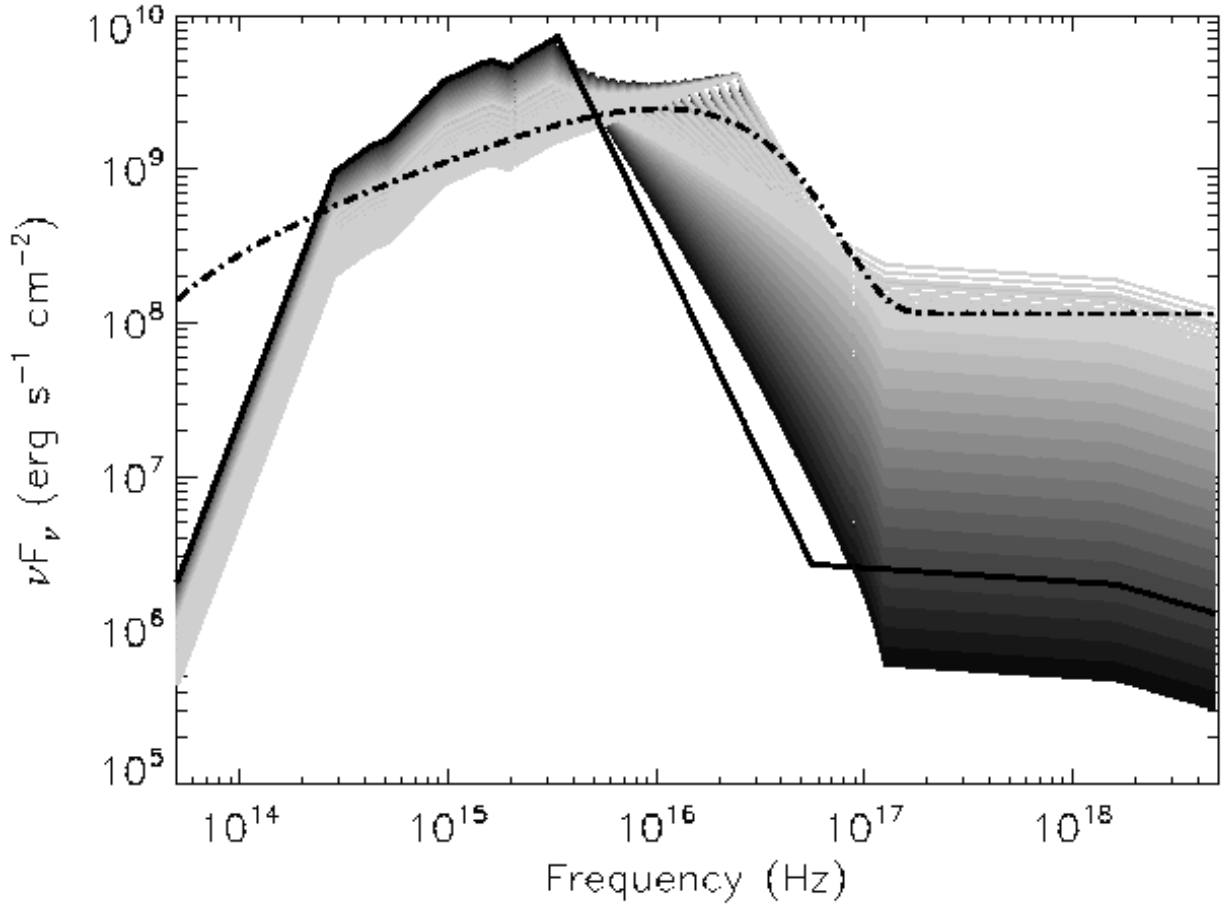


Fig. 33.— The spectral energy distributions used in Appendix A.1. The SEDs are based on the PHL 1811 and are described by two parameters: α_{ox} , and the break between the UV and the X-ray. All SEDs are shown for the same value of the photoionizing flux. These SEDs span parameter space described by the strength of the extreme UV and the strength of the X-ray between the PHL 1811 (thick solid line) and the K97 (thick dash-dot line).

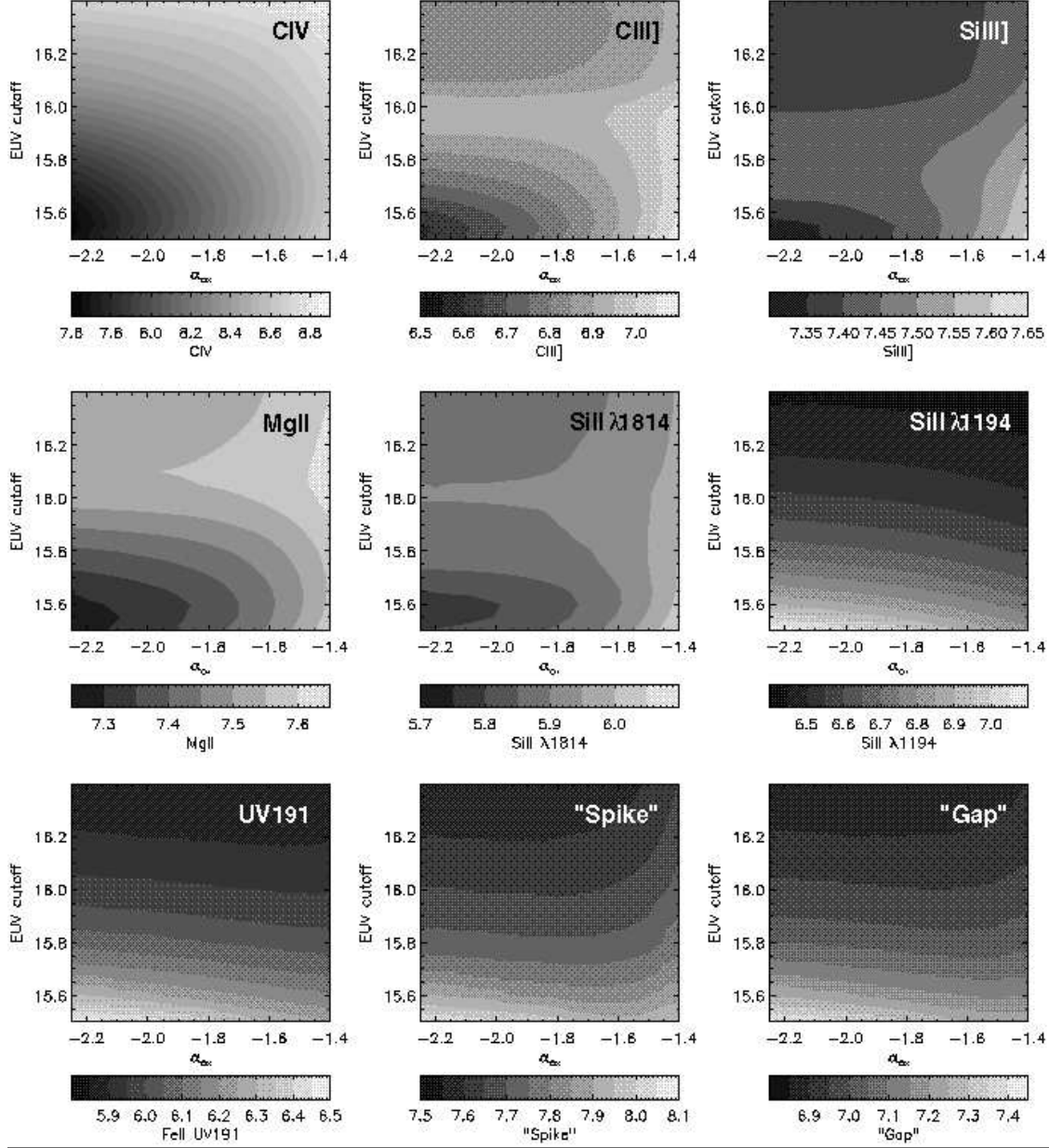


Fig. 34.— Contours of the log of the line flux as a function of the parameters describing the SEDs shown in Fig. 33, α_{ox} and the EUV cutoff, evaluated for the fiducial parameters ($\log U = -1.5$, $\log n = 11.0$, and $\log N_H = 24.5$). A variety of lines are shown, including lines emitted in the H II region (top row), the partially-ionized zone (middle row), and UV Fe II lines (bottom row). In each graph the shaded contour interval is 0.05. The behavior of high-ionization lines is governed by the ionization potential of the lines. Collisionally excited intermediate- and low-ionization lines such as C III], Si III], Mg II, and Si II $\lambda 1814$ depend primarily on the temperature. Pumped lines including Si II $\lambda 1194$, and Fe II lines UV 191, and the Baldwin et al. (2004) “spike” and “gap” lines depend on the UV flux, which is stronger for a given photoionizing flux for lower values of the EUV cutoff, and the temperature.

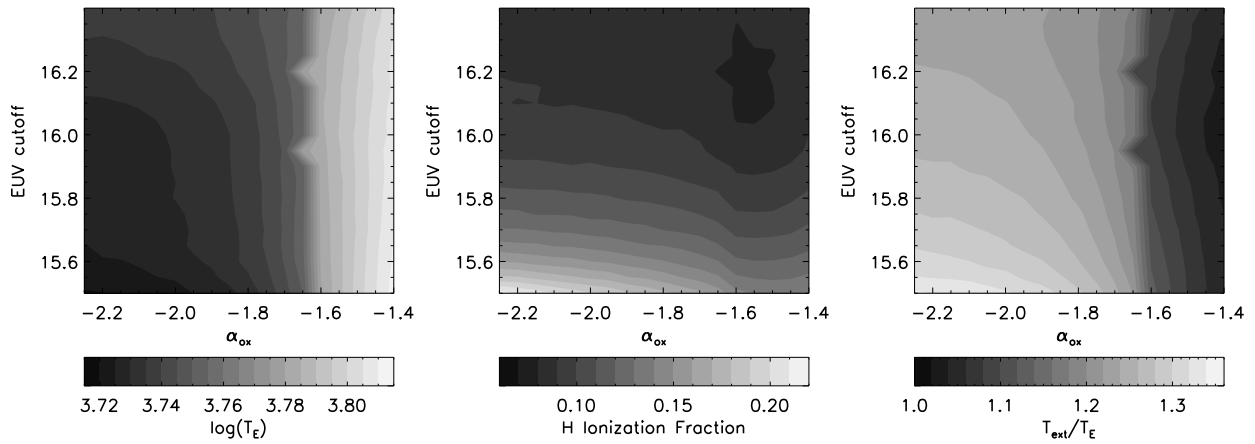


Fig. 35.— Properties of gas illuminated by SEDs shown in Fig. 33, evaluated at a depth of ten times the depth of the hydrogen ionization front. The electron temperature (left), the hydrogen ionization fraction (middle) and the ratio of the excitation temperature to the electron temperature for $n = 2$ are shown as functions of the parameters describing the SEDs, α_{ox} and the EUV cutoff.

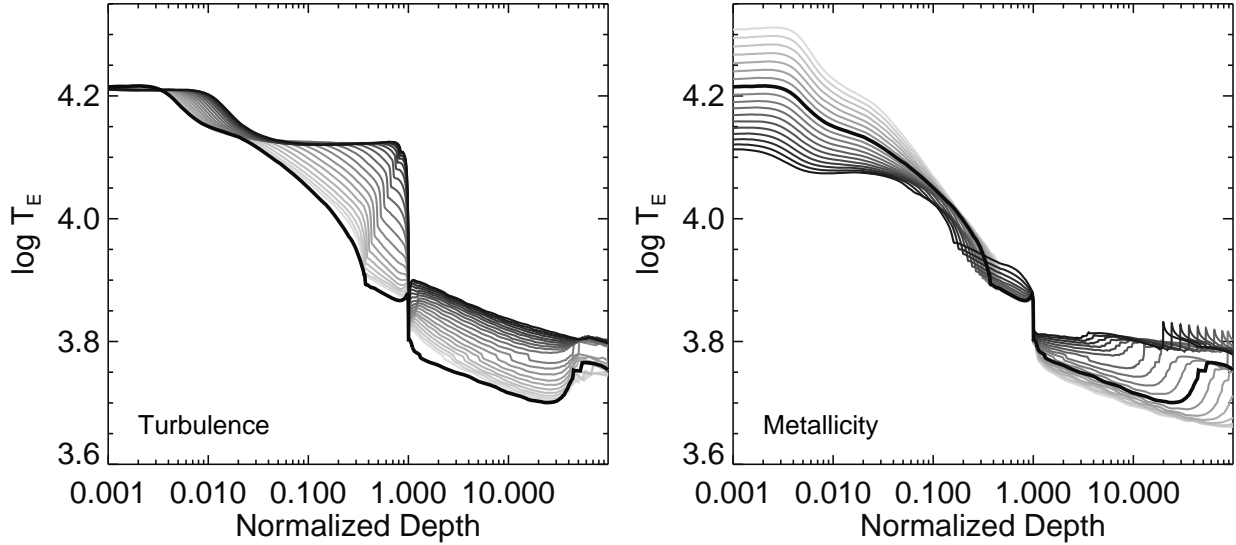


Fig. 36.— The electron temperature as a function of the ratio of the depth to the depth of the hydrogen ionization front for the fiducial gas parameters ($\log U = -1.5$, $\log n = 11$, and $\log N_H = 24.5$) as microturbulence (left) and metallicity (right) are varied. The solid line shows the result for the PHL 1811 continuum with $v_{turb} = 0$ and $Z/Z_\odot = 1$. Light to dark shows the results as the parameters are increased. Increase of either turbulence or metallicity results in an increase in temperature in the partially-ionized zone to values comparable to those obtained for typical AGN continua (Fig. 14).

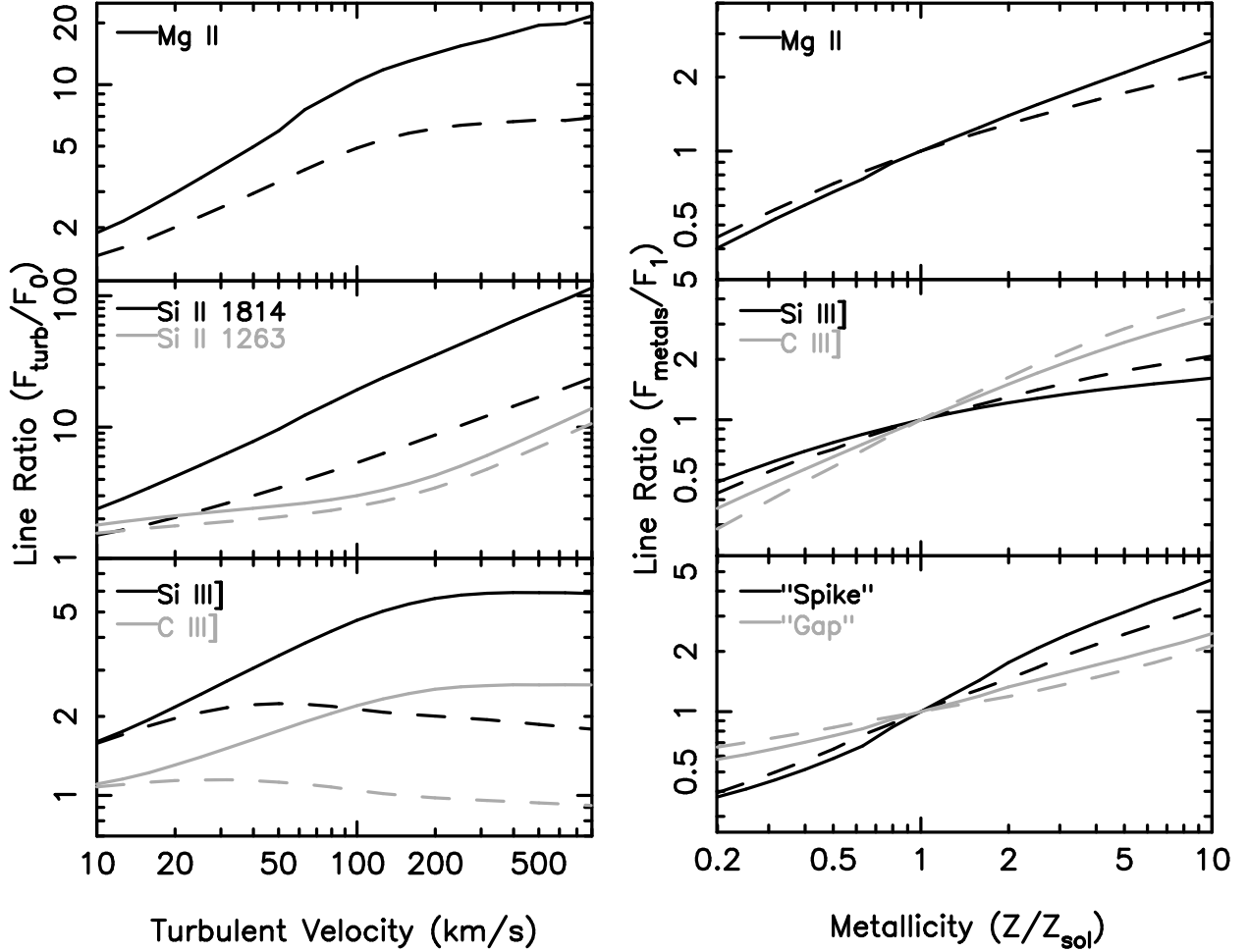


Fig. 37.— The ratio of lines as a function of turbulence (left) and metallicity (right) to the values obtained for models in which $v_{\text{turb}} = 0$ and $Z/Z_{\odot} = 1$, respectively, evaluated for the fiducial parameters ($\log U = -1.5$, $\log n = 11.0$, and $\log N_H = 24.5$). The solid and dashed lines show the case for the PHL 1811 and the K97 SEDs. More rapid increases in the line ratios for the PHL 1811 SED compared with the K97 SED are a consequence of temperature increases with turbulence and metallicity.